TECHNISCHE UNIVERSITÄT MÜNCHEN

Lehrstuhl für Numerische Mechanik

Computational and Experimental Modeling of Lung Parenchyma

Sophie M.K. Rausch

Vollständiger Abdruck der von der Fakultät für Maschinenwesen der Technischen Universität München zur Erlangung des akademischen Grades eines

Doktor-Ingenieurs (Dr.-Ing.)

genehmigten Dissertation.

Vorsitzender:		Univ.-Prof. Dr. mont. habil., Dr. h. c. Ewald Werner
Prüfer der Dissertation:		
	1.	Univ.-Prof. Dr.-Ing. Wolfgang A. Wall
	2.	Univ.-Prof. Dr.-Ing. Markus Böl, Technische Universität Braunschweig

Die Dissertation wurde am 21.05.2012 bei der Technischen Universität München eingereicht und durch die Fakultät für Maschinenwesen am 17.07.2012 angenommen.

Abstract

Acute Lung Injury (ALI) and its more severe form Acute Respiratory Distress Syndrome (ARDS) are serious diseases of the lung, with mortality rates of up to 33 %. Typically, patients suffering from ALI/ARDS need mechanical ventilation. However, the mechanical ventilation may lead to regional, inhomogeneous overstraining of the lung tissue, especially in the alveolar region. The damage caused by this overstraining is a so-called ventilator-associated lung injury (VALI), which contributes significantly to the high mortality rates of ALI/ARDS patients.

The goal of this study is to develop mathematical models that enable the quantification of strains and stresses of the lung tissue during ventilation. These models can be used to optimize mechanical ventilation strategies in the future.

Therefore, in a first step, the material behavior of lung parenchyma is experimentally characterized. By treating the tissue with specific enzymes, the contribution of the individual load-bearing components and their interaction is quantified for the first time. In a second step, suitable non-linear, compressible and elastic mathematical models are formulated, which reproduce the experimentally determined behavior in an adequate way. The model parameters are determined using an inverse analysis approach. Thereby, the experiments are simulated using the finite element (FE) method and the parameters of the models are optimized until the computational and the experimental results match. Different material models are compared, regarding their suitability to model the complex elastic behavior of lung tissue. Based on this comparison two optimal material models for lung parenchyma are defined. While the first model is purely phenomenological, the second model considers the individual contributions of the tissue components, i.e. ground substance, collagen and elastin fibers, as well as the fiber-fiber interaction. With this constituent-based material model, diseased states involving pathologic changes of the composition of the tissue, e.g. fibrosis, can be modeled in a straight forward manner. Using one of the proposed models the global strains and stresses within lung parenchyma can be determined.

In the next step, the correlation between global strains within the lung parenchyma and local stains within individual alveolar walls is investigated, by performing FE simulations of three-dimensional image-based alveolar geometries. With these simulations, the three-dimensional strain-state within alveolar walls is determined for the first time. It turns out that the local strains are a multiple of the global tissue expansion and areas of slim wall places have a higher risk of overstretch. Consequently, resolving the realistic alveolar morphology is crucial when investigating phenomena like VALI.

Zusammenfassung

Die akute Lungenschädigung (Acute Lung Injury, ALI) und das daraus resultierende akute Lungenversagen (Acute Respiratory Distress Syndrome, ARDS) sind schwere Erkrankungen der Lunge, mit Sterblichkeitsraten von bis zu 33 %. ALI/ARDS-Patienten müssen in der Regel künstlich beatmet werden. Dabei kann es jedoch zu regionalen, inhomogenen Überdehnungen des Lungengewebes, besonders im Alveolarbereich, kommen. Die, durch diese Überbeanspruchung hervorgerufenen, Verletzungen werden als beatmungsinduzierte Lungenschäden bezeichnet. Sie tragen wesentlich zu der hohen Sterblichkeitsrate von ALI/ARDS-Patienten bei.

In dieser Studie sollen mathematische Modelle entwickelt werden, um die Spannungen und Dehnungen im Lungengewebe während der Beatmung zu quantifizieren. Mit Hilfe dieser Modelle kann die künstliche Beatmung in Zukunft optimiert werden.

Zu diesem Zweck wird zunächst das Materialverhalten des Lungengewebes experimentell untersucht. Durch die Behandlung des Lungengewebes mit Enzymen können die Beiträge der einzelnen Gewebebestandteile zur Lastabtragung erstmalig quantifiziert werden. Anschließend werden geeignete nichtlineare, kompressible und elastische mathematische Modelle formuliert, die das beobachtete Verhalten abbilden können. Durch lösen eines inversen Problems werden die zugehörigen Modellparameter bestimmt. Dabei werden die Experimente mit der Methode der Finiten Elemente (FE) simuliert und die Modellparameter optimiert, bis die Ergebnisse der Modelle mit den experimentellen Ergebnissen übereinstimmen. Anschließend werden verschiedene Materialmodelle bezüglich ihrer Eignung, das Verhalten des komplexen Lungengewebes optimal abzubilden, verglichen. Dieser Vergleich lieferte zwei optimale Materialmodelle für das Lungengewebe. Während das erste Model rein phänomenologisch ist, berücksichtigt das zweite Modell die individuellen Beiträge der einzelnen Gewebebestandteile, wie die Grundsubstanz, die Kollagen- und Elastinfasern und deren Interaktion. Mit diesem Materialmodell der Gewebebestandteile können Krankheiten, bei denen sich die Gewebezusammensetzung pathologisch verändert, direkt modelliert werden. Mit Hilfe eines der beiden Modelle können die globalen Spannungen und Dehnungen im Lungengewebe bei der künstlichen Beatmung berechnet werden.

In einem weiteren Schritt wird der Zusammenhang zwischen globalen Dehnungen des Lungengewebes und die lokalen Dehnungen in den Alveolarwänden bestimmt. Mit einer auf gescannten dreidimensionalen Alveolargeometrien basierenden FE-Simulation können die dreidimensionalen Verzerrungen des Alveolargewebes erstmalig quantifiziert werden. Dabei zeigt sich, dass die lokalen Verzerrungen in den Aveloarwänden ein Vielfaches der

globalen Verzerrungen erreichen und dass besonders für schlanke Strukturen ein erhöhtes Überdehnungsrisiko besteht. Folglich ist die Berücksichtigung der realen alveolaren Morphologie entscheidend für die Unteruchung von beatmungsinduzierten Lungenschäden.

Danksagung

An dieser Stelle möchte ich mich bei allen, die mich während der letzten fünf Jahren begleitet und unterstützt haben, herzlich bedanken.

Bei meinem Doktorvater Prof. Dr. Wolfgang A. Wall bedanke ich mich für sein Vertrauen und seine Geduld.

Weiterhin bedanke ich mich bei Prof. Dr. Markus Böl vom Institut für Festkörpermechanik an der Technische Universität Braunschweig für die Übernahme des Mitberichts und bei dem Vorsitzenden meiner Prüfungskommission Prof. Dr. Dr. Ewald Werner vom Lehrstuhl für Werkstoffkunde und Werkstoffmechanik der Technischen Universität München.

Bei meinen derzeitigen und ehemaligen Kollegen möchte ich mich herzlich für die angenehme Arbeitsatmosphäre bedanken. Besonders die Zusammenarbeit und Freundschaft mit Dr. Lena Yoshihara im "Team Lung" war für mich in den letzten Jahren sehr wichtig. Außerdem möchte ich mich bei Dr. Burkhard Bornemann, Dr. Ulrich Küttler, Dr. Thomas Klöppel und Caroline Danowski für ihre umfassende Unterstützung bedanken.

Für die Förderung durch die Deutsche Forschungsgemeinschaft (DFG) im Rahmen des Forschungsschwerpunktes "Protektive Beatmung" bin ich sehr dankbar. Die Zusammenarbeit mit renommierten Wissenschaftlern aus verschiedenen Disziplinen habe ich als großes Privileg empfunden. Vor allem danke ich Prof. Dr. Stefan Uhlig, Dr. Christian Martin, Oliver Pack, Prof. Dr. Johannes Schittny, Dr. David Haberthür, Prof. Dr. Josef Guttmann, Prof. Dr. Knut Möller, Prof. Dr. Edmund Koch und Dr. Constanze Dassow. Die vielen hilfreichen Erklärungen und ergiebigen Diskussionen haben meine Arbeit sehr vorangebracht.

Besonderer Dank gebührt auch meiner Familie und meinen Freunden für ihre Geduld, Anteilnahme und Unterstützung in allen Phasen meiner Promotion.

Sophie Rausch

Contents

Nomenclature

Representation of Scalars and Tensors

Q, q	Material and current scalar value
$\mathbf{G}, \mathbf{g}$	Material and current second-order tensor
$\mathbb{C}$	Higher-order tensor

Operators and Symbols

$(\bullet)$	Variable
$(\bullet)_t$	Variable at time t
$(\bullet)_0$	Variable at the material configuration
$(\bullet)^T$	Transpose of a tensor
$(\bullet)^{-1}$	Inverse of a tensor or mapping
$(\bullet)^{-T}$	Transpose of the inverse of a tensor
$(\dot{\bullet})$	Time derivative
det	Determinant
tr	Trace operator
$\nabla_{\mathbf{X}}$	Material gradient operator
$\nabla_{\mathbf{x}}$	current gradient operator
$\nabla\cdot$	Material divergence operator
$\otimes$	Dyadic product
$\odot$	Specific tensor product
$\mathbf{1}$	Identity tensor
exp	Exponential function

Subscripts and Superscripts

$(\bullet)_M$	Variable based on material mass
$(\bullet)_V$	Variable based on material volume
$(\bullet)_{\mathrm{ext}}$	External
$(\bullet)_{\mathrm{int}}$	Internal

Domains and Boundaries

$\mathcal{B}$	Body
$\mathcal{B}_0, \mathcal{B}_t$	Body in the material and current domain
$\partial\mathcal{B}_0, \partial\mathcal{B}_t$	Boundary in material and current configuration
$\partial_{\mathbf{u}}\mathcal{B}_0$	Dirichlet partition of boundary in material configuration
$\partial_{\mathbf{S}}\mathcal{B}_0$	Neumann partition of boundary in material configuration

Kinematics

$\mathbf{X}, \mathbf{x}$	Position in material and current configuration
t_0, t	Stating and current time
$\mathbf{f}$	Force
$\boldsymbol{\varphi}$	Particle motion mapping
$\mathbf{U}, \mathbf{u}$	Displacement vector in material and current configuration
$\mathbf{V}, \mathbf{v}$	Velocity vector in material and current configuration
$\mathbf{A}, \mathbf{a}$	Acceleration vector in material and current configuration
V, v	Material and current volume
A, a	Material and current surface area
L, l	Material and current length
$\tilde{\mathbf{N}}, \tilde{\mathbf{n}}$	Normal vector in material and current configuration
$\mathbf{N}, \mathbf{n}$	Unit normal vector in material and current configuration

ψ	Ridged body movement
$\mathbf{R}$	Rotation tensor
$\mathbf{c}$	Translation tensor
$\mathbf{F}$	Deformation gradient
J	Determinant of $\mathbf{F}$
$\bar{\mathbf{F}}$	Isochoric part of $\mathbf{F}$

Strain Measures

$\mathbf{C}$	Right Cauchy-Green strain tensor
$\bar{\mathbf{C}}$	Modified right Cauchy-Green strain tensor
I_1, I_2, I_3	First, second and third invariant of $\mathbf{C}$
$\bar{I}_1, \bar{I}_2$	Modified first and second invariant of $\bar{\mathbf{C}}$
$\mathbf{E}$	Green-Lagrange strain tensor
$\mathbf{e}$	Euler-Almansi strain tensor
$\dot{\mathbf{E}}$	Strain rate tensor
$\tilde{\mathbf{U}}, \tilde{\mathbf{v}}$	Right and left strain tensor

Stress Measures

$\mathbf{T}, \mathbf{t}$	Material and current traction
$\mathbf{P}$	First Piola-Kirchhoff stress tensor
$\mathbf{S}$	Second Piola-Kirchhoff stress tensor
$\boldsymbol{\sigma}$	Cauchy stress tensor
$\boldsymbol{\tau}$	Kirchhoff stress tensor

Governing Equations

M, m	Mass in material and current configuration

ρ_0,ρ	Density in material and current configuration
$\mathbf{L}$	Linear Momentum
$\mathbf{Y}$	Arbitrary point in material configuration
$\tilde{\mathbf{R}}$	Torsion arm in material configuration
$\mathbf{J}_{\mathbf{Y}}$	Angular momentum
$\mathcal{D}_{\text{int}}$	Internal dissipation
$\mathcal{P}_{\text{ext}}$	External mechanical power
$\mathcal{Q}_{\text{ext}}$	Non-mechanical Power
$\mathcal{S}$	Entropy
$\mathcal{S}_M$	Specific entropy
ϵ	Energy
ϵ_{int}	Internal energy
$\epsilon_{\text{int},\,M}$	Internal energy referred to material mass
ϵ_{kin}	Kinetic energy
T	Absolute temperature
$\mathbf{f}_0^{\text{ext}}$	External force
$\mathbf{m}_0^{\text{ext}}$	External momentum
$\mathbf{f}_V^{\text{body}}$	Initial body force

Boundary Conditions

$\hat{\mathbf{u}}_0$, $\hat{\mathbf{u}}$	Displacement boundary condition in the material and current configuration
$\hat{\mathbf{v}}_0$, $\hat{\mathbf{v}}$	Velocity boundary condition in the material and current configuration
$\hat{\mathbf{T}}$	Traction boundary condition in the material configuration

Constitutive Models

Ψ_{v},Ψ	Strain energy density function

Ψ_M	Helmholtz free-energy
Ψ_{total}	Sum of strain energy density functions
Ψ_{iso}	Isochoric strain energy density functions
Ψ_{vol}	Volumetric strain energy density functions
Ψ_{summand}	Potential strain energy density function summand
Ψ_{par}	Strain energy density function for lung parenchyma
Ψ_{blako}	Coupled strain energy density function suggested by Blatz and Ko
Ψ_{neo}	Coupled neo Hookean strain energy density function
$\Psi_{\text{neo, Holzapfel}}$	Coupled neo Hookean strain energy density function suggested by Holzapfel
$\Psi_{\text{iso, neo}}$	Isochoric neo Hookean strain energy density function summand
$\Psi_{\text{iso, yeoh}}$	Isochoric strain energy density function summand suggested by Yeoh
$\Psi_{\text{iso, lin}}$	Isochoric, linear strain energy density function summand
$\Psi_{\text{iso, quad}}$	Isochoric, quadratic strain energy density function summand
$\Psi_{\text{iso, cub}}$	Isochoric, cubic strain energy density function summand
$\Psi_{\text{iso, pow}(\bullet)}$	Isochoric, power function strain energy density function summand
$\Psi_{\text{iso, exp}}$	Isochoric, exponential strain energy density function summand
$\Psi_{\text{iso, mori}}$	Isochoric, mooney rivlin function strain energy density function summand
$\Psi_{\text{vol, ogd}}$	Volumetric strain energy density function summand suggested by Ogden
$\Psi_{\text{vol, pen}}$	Penalty volumetric strain energy density function summand
$\Psi_{\text{vol, suba}}$	Volumetric strain energy density function summand suggested by Sussmann and Bathe
Ψ_{ex}	Example strain energy density function
Ψ_{GS}	Ground substance strain energy density function
Ψ_{CF}	Collagen fibers strain energy density function
Ψ_{EF}	Elastin fibers strain energy density function
Ψ_{FF}	Fiber-fibers interaction strain energy density function

$\mathbb{C}$	Elasticity tensor
$\gamma_1 - \gamma_3$	Derivation coefficients gamma for **S**
$\delta_1 - \delta_8$	Derivation coefficients delta for $\mathbb{C}$
$\overline{\gamma}_{\text{iso, 1}}, \overline{\gamma}_{\text{iso, 2}}$	Isochoric derivation coefficients gamma for **S**
$\overline{\gamma}_{\text{vol, 1}}$	Volumetric derivation coefficient gamma for **S**
$\overline{\delta}_{\text{iso, 1}} - \overline{\delta}_{\text{iso, 4}}$	Isochoric derivation coefficients delta for $\mathbb{C}$
$\overline{\delta}_{\text{vol, 1}}, \overline{\delta}_{\text{vol, 2}}$	Volumetric derivation coefficients delta for $\mathbb{C}$

Material Constants

β	Material parameter
c	Material parameter
$c_{\text{yeoh, 1}}, c_{\text{yeoh, 2}}, c_{\text{yeoh, 3}}$	Yeoh material parameter
$c_{\text{exp, 1}}, c_{\text{exp, 1}}$	Exponential material parameters
$c_{\text{mori, 1}}, c_{\text{mori, 2}}$	Mooney-Rivlin material parameters
c_{lin}	Linear summand material parameter
c_{quad}	Quadratic summand material parameter
c_{cub}	Cubic summand material parameter
$c_{\text{pow}(\bullet)}$	Power law material parameter
G	Shear Modulus
λ	Lame's constant
ν	Poisson's ratio
E	Young's modulus
ϵ	Material parameter
γ	Material parameter
κ	Bulk modulus

Experiments

ρ_{par}	Parenchyma density
L_0, L	Initial length before and after preconditioning
p	Pressure

Inverse Analysis

ρ_{par}	Parenchyma density
n	Number of time steps
k	Number of material parameters
j	Current run of the inverse analysis
j_{max}	Maximal number of runs of the inverse analysis
T, T_{old}	Current and old target function
T_n	Normalized target function
λ, λ_{old}	Current and old damping factor
$\mathbf{p}_0$, $\mathbf{p}$	Initial and current parameter vector
$\Delta\mathbf{p}$	Delta parameter vector
$\mathbf{r}$	Residual vector
$\mathbf{u}$	Displacement vector
$\mathbf{u}_i$	Subdisplacement vector
u_x	x-displacement
u_y	y-displacement
$\mathbf{J}_\mathbf{r}$	Jacobian-matrix of **r**
$\mathbf{g}$	Gradient vector
$\mathbf{H}$	Hessian matrix

Abbreviations

ALI	Acute Lung Injury
ARDS	Acute Respiratory Distress Syndrome
BACI	Bavarian Advanced Computational Initiative
BIC	Bayesian information criterion
CF	Collagen fiber(s)
CT	Computer tomographic
CV	Coefficient of variation
DFG	German Research Foundation
dof	Degree of freedom
EF	Elastin fiber(s)
FE	Finite element
FEM	Finite element method
FF	Fiber-fiber interaction
FRC	Functional residual capacity
FSI	Fluid-structure interaction
GAG	Glycosaminoglycan
GS	Ground substance
MEM	Minimal essential medium
MRI	Magnetic resonance imaging
ICU	Intensive care unit
PCLS	Precision-cut lung slice(s)
PEEP	Positive end-expiratory pressure
sd	Standard derivation
SEF	Strain energy density function
SLS	Swiss Light Source
SRXTM	Synchrotron-based X-ray tomographic microscopy
STL	Surface Tesselation Language

TLC	Total lung capacity
TOMCAT	Tomographic microscopy and coherent radiology experiments
VALI	Ventilator-associated lung injury
VILI	Ventilator-induced lung injury

List of Figures

List of Tables

1 Introduction and Motivation

> *"The acute respiratory distress syndrome continues as a contributor to the morbidity and mortality of patients in intensive care units throughout the world, imparting tremendous human and financial costs."(Bernard et al., 1994)*

Acute Lung Injury (ALI) and its more severe form Acute Respiratory Distress Syndrome (ARDS) are severe respiratory diseases with mortality rates of up to 33 %, as reported by the groundbreaking study of The Acute Respiratory Distress Syndrome Network (2000). The diseases can be caused by any major inflammation or injury to the lung, for example breathing vomit into the lung (aspiration), inhaling chemicals, pneumonia, septic shock, or trauma. The main problem of this disease is the accumulation of fluid within the air sacs, preventing oxygen transport into the blood stream. Additionally, due to the surface tension of the fluid, the lungs become stiffer and the ability to expand decreases. Hence, the lung functions very inefficiently. This causes the oxygen level in the blood stream to drop dangerously low, even when the patient is artificially ventilated. The deathly form of ALI/ARDS often occurs in combination with the failure of other vital organs, such as the liver or kidneys. Typically, patients suffering from ALI/ARDS need to be mechanically ventilated in the intensive care unit (ICU). The goal of the treatment is to provide breathing support and cure the underlying processes. This involves medication to reduce the infection and the resulting inflammation as well as the removal of the fluid from the lungs.

However, although mechanical ventilation is a mandatory life saving treatment, it is unfortunately the cause of further complications. The problem is that the damage during ALI/ARDS is inhomogeneous. Therefore, the air distributes unevenly throughout the lung, which leads to regional overstretching during mechanical ventilation. The damage and inflammation, caused by this overstretching, is a so-called ventilator-associated lung injury (VALI) which contributes significantly to the high mortality rates of ALI/ARDS patients. The introduction of protective ventilation protocols, including positive end-expiatory pressure (PEEP) and a decrease of tidal volume, has led to a reduction in associated mortality rates but they still remain unsatisfactorily high (The Acute Respiratory Distress Syndrome

Network, 2000). The usage of PEEP should prevent the lungs from partly collapsing (atelectrauma), by not letting the pressure drop to zero at the end of expiration. The reduction of tidal volume should prevent the tissue from being overstretched during ventilation (volutrauma). Due to the unevenly distributed air within the lung, the optimal level of PEEP, tidal volume etc. are extremely difficult to determine for individual ALI/ARDS patients.

VALI includes both mechanical damage of the tissue and activation of an inflammatory signaling cascade (biotrauma). How the ventilation exactly induces its deleterious effects still remains unclear. Studies both *in vitro* and *in vivo* have found that both the pattern and the degree of stretching are important (Dos Santos and Slutsky, 2000, 2006; Dassow et al., 2010).

The work presented in this thesis is part of the German Research Foundation (DFG) priority program “Protective Artificial Respiration”. *The main goal of this interdisciplinary initiative is to further improve mechanical ventilation in order to reduce the high mortality rate due to VALI.* For this purpose, a detailed “virtual lung model” is developed jointly at the Institute for Computational Mechanics (TUM). One important part involves the modelling of the lung tissue behavior.

In this thesis, sophisticated material models for the lung parenchyma are be deduced from experimental studies of lung parenchyma. Based on these models global strains and stresses within the lung parenchyma can be determined. As a next step, the relation between the global strains of the lung parenchyma and the local deformation in individual alveolar walls is investigated by performing finite element (FE) simulations on three-dimensional image-based alveolar geometries. Using these simulations, a three-dimensional strain state within the alveolar walls is determined for the first time. This approach will improve the understanding of the underlying processes causing the inflammation during VALI.

2 Anatomy, Physiology and Pathology of the Lung

In this chapter, all the necessary background concerning anatomy, physiology and pathology of the lung will be provided as well as the pathology of Acute Lung Injury (ALI) and Acute Respiratory Distress Syndrome (ARDS) and ventilator-associated lung injury (VALI). This is in order to put the wider goals (see chapter 5) of this research into context.

2.1 Anatomy of the Lung

The primary function of the lung is gas exchange, i.e. introducing oxygen into and removing carbon dioxide from the blood stream. In addition, the lung has other functions, e.g. filtering of unwanted materials. It is essential to understand the complex features of the lung structure, in order to understand how the lung reacts to injury and diseases.

Therefore, a brief introduction of the anatomy of the lung, from the upper airways, over the conducting airways, down to the respiratory zone, is provided below.

2.1.1 Upper Airways

The upper airways are all conducting structures above the *trachea* (windpipe). They include the *nasal cavity*, the *pharynx* (throat), and the *larynx*. The pharynx belongs to both the respiratory and the digestive system. It splits into the larynx and the *esophagus* leading to the digestive track. The *nasopharynx* humidifies the inhaled gas, clears out inhaled particles and reactive substances, as well as contributes to senses like smell and taste (Crapo, 2000).

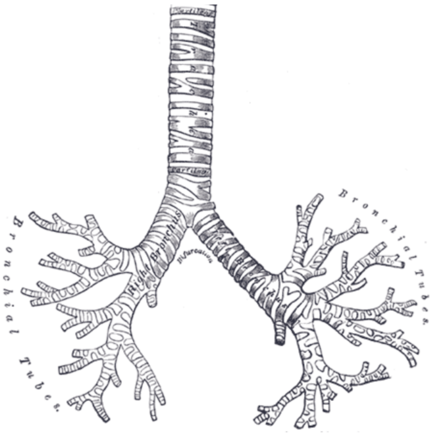

Figure 2.1: Front view of cartilages in the trachea and bronchi. Figure taken from Gray and Bannister (1995).

2.1.2 Airways - Conducting Zone

The primary airways consist of the trachea, the *bronchi,* and the *bronchioles* (see Figure 2.1). The trachea is a cartilaginous and membranous tube of about $100 - 150\,\text{mm}$ length of around $20\,\text{mm}$ in diameter. It divides into the two *mainstem bronchi*, one for each lobe of the lung. The bronchi rapidly divide, in an irregular pattern, into progressively smaller bronchi (see Figure 2.2). After about 16 generations of branching, the terminal bronchioles are reached. The terminal bronchioles are the smallest units in the lungs with a solely conducting function. Because the conducting airways do not participate in gas exchange, their volume is referred to as the *anatomic dead space*, which, in a normal adult, is around $150\,\text{ml}$. (Weibel, 1963; Horsfield et al., 1971; Gray and Bannister, 1995; Crapo, 2000; Ethier and Simmons, 2007; West, 2008).

Despite the fact that the cross-sectional area of the daughter branches decreases, the increasing number of branches leads to an almost exponential increase in total cross-sectional area. This increase leads to a fall in airway resistance, as well as a reduction in the flow velocity.

2.1.3 Transitional and Respiratory Zone

The actual gas exchange takes place in the transitional and respiratory zone. It consists of the respiratory bronchioles, the alveolar ducts and the alveolar sacs, see Figure 2.2.

2.1.3.1 Alveolar Acinus

Distal to the terminal bronchioles, the respiratory bronchioles, and the alveolar ducts the alveolar sacs are organized in individual *alveolar acini*. Despite the name acini, from the Latin word for “bunch of grapes”, alveoli do not look like grapes, rather they are polygonal in shape and interconnected by shared walls and pores of Kohn (Prange, 2003). The primary function of the acinar region is gas exchange, in particular oxygen transfer into and carbon dioxide removal from the blood stream. Although, the distance from the terminal bronchioles to the alveoli is only a few millimeters, the respiratory zone represents the biggest portion of the lung volume, with about $2.5 - 3.0l$ during rest.

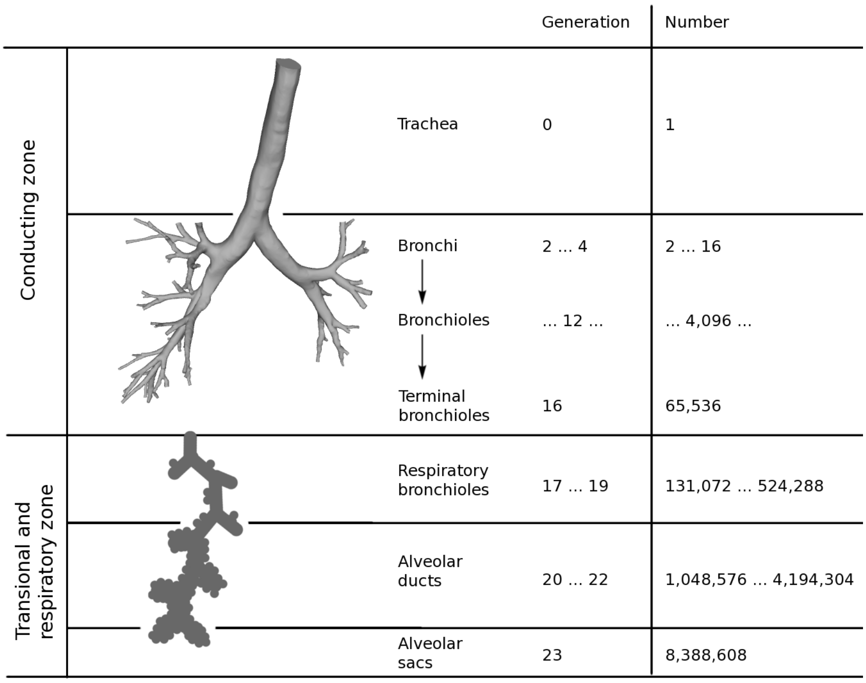

		Generation	Number
Conducting zone	Trachea	0	1
	Bronchi	2 ... 4	2 ... 16
	↓		
	Bronchioles	... 12 ...	... 4,096 ...
	↓		
	Terminal bronchioles	16	65,536
Transional and respiratory zone	Respiratory bronchioles	17 ... 19	131,072 ... 524,288
	Alveolar ducts	20 ... 22	1,048,576 ... 4,194,304
	Alveolar sacs	23	8,388,608

Figure 2.2: Schematic diagram of the airway tree, showing the different functional zones, i.e. the conducting zone, the transitional zone, and the respiratory zone. The number of airways is actually larger than that listed here, since the tabulated values are based on a simple bifurcating model of the airways; the reality is more complex. The Figure is adapted from Weibel (1963, 1984); Ethier and Simmons (2007); West (2008).

2.1.3.2 Alveoli

Alveoli are the smallest gas exchanging unit in the lung. According to recent estimations, the average number of alveoli is around 480 million with an average volume of 4.2 ×

$10^6\,\mu m^3$ and a diameter of $100\,\mu m$ (Ochs et al., 2004). The total surface has been quoted to be between $100-140\,m^2$ (Weibel, 1984; Crapo, 2000; West, 2008), which is of uppermost importance for the gas exchange.

Alveoli are arranged in a foam-like structure, the so-called *parenchyma*, and fill the entire volume of the lungs surrounding the airways. A part of a typical alveolar structure reconstructed from synchrotron-based X-ray tomography images, is shown in Figure 2.3 (B). It shows the complicated construction of the parenchymal tissue.

The individual alveoli are separated by a thin wall, the inter-alveolar septum which is referred to as the *alveolar wall* or the *single alveolar wall* in the following text. This wall is not only the separation of alveoli but also part of the blood-gas barrier, separating the air space from the capillaries filled with red blood cells and blood plasma. It consisting of:

1. a monolayer of epithelial cells lining the alveolar wall, with a supporting basement membrane,
2. the interstitium including collagen fibers (CF) and elastin fibers (EF), and
3. a layer of endothelial cells lining the capillaries, also supported by a basement membrane,

see Figure 2.3 (C).

In this study, the focus lies on biomechanics. For this reason, we are especially interested in the structures dominating the elastic behavior of the alveolar tissue, i.e. the main load-bearing constituents. According to Suki et al. (2005), these constituents are the CF and EF in the interstitium. Similar results were found by Yuan et al. (1997, 2000), who showed that CF and EF have a dominant influence, on the mechanical behavior of alveolar tissue, in comparison with the interstitial cells. The dominance of these fibers on the mechanical behavior of tissue is not specific to the lung, it actually occurs in most soft biological tissues, e.g. the cornea and the sclera of the eyes (Fung, 1993), the arterial walls (Holzapfel et al., 2000), the tendons (Kastelic et al., 1978), or the articular cartilage (Basser et al., 1998). Although these fiber networks exist in many soft biological tissues, their organization (diameter, inner structure and orientation) varies greatly (Ottani et al., 2001). The situation for alveolar tissue is comparatively more complicated, due to its sponge-like geometry.

Collagen Fibers Collagen is the basic structural element in both hard and soft biological tissue. It gives mechanical integrity and strength to the tissue. CF are the main load carrying elements in many biological tissues, like blood vessels, skin, tendons, cornea,

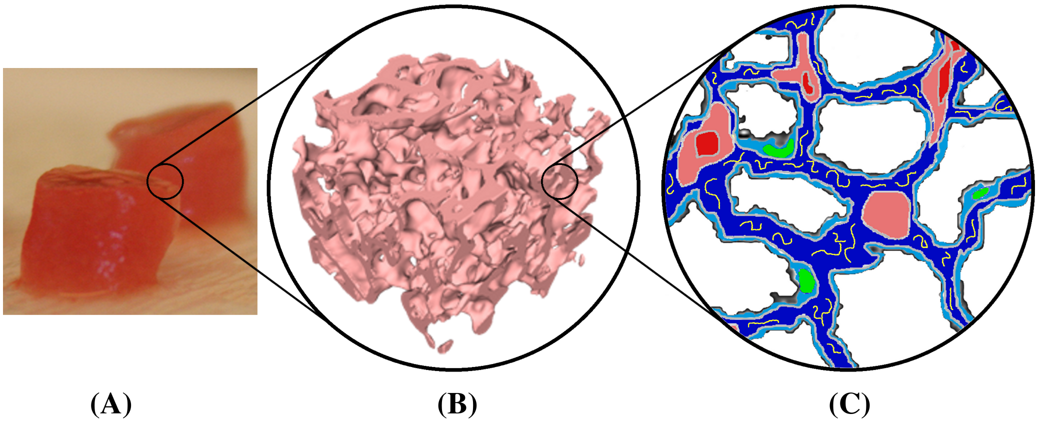

Figure 2.3: The makeup of parenchymal and alveolar tissue - On the macro-scale (A), the lung parenchyma appears as a continuous tissue but zooming further down to, the meso-scale (B) or the tissue has a sponge-like structure, consisting of only 20 % tissue and 80 % air (Tschanz et al., 2003). At a micro-scale (C), the actual tissue components are visible. The collagen and elastin fibers, indicated in yellow, are within the interstitium (dark blue). The endothelial cells are indicated in light blue with a green nucleus. The blood plasma is indicated with a light red and the red blood cells with a darker red. The basement membrane (light gray), and the surfactant layer, which is the liquid lining on the tissue-air interfaces (see section 2.1.3.4), is indicated by shades of gray. The endothelial cells are not shown.

sclera, bone. The CF make up 10 % to 20 % of the dry weight of an adult lung (Crystal et al., 1975).

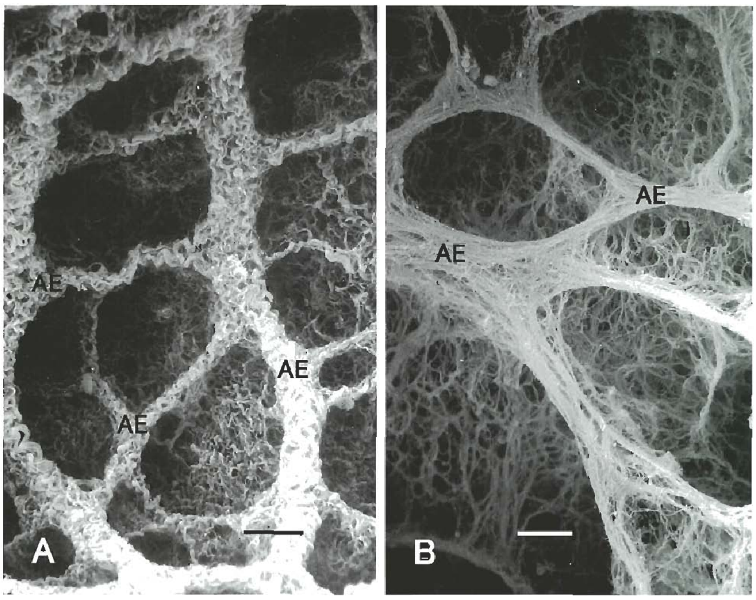

Figure 2.4: Electron microscopy pictures of collagen fiber (CF) networks in rat lungs. Figures taken from Toshima et al. (2004). (A) CF network at the alveolar entrances (AE) in the collapsed lung. (B) CF network at the AE in the inflated rat lung. Both scale bars correspond to 100 µm.

CF exhibit a strongly non-linear mechanical behavior. At low levels of strain (in the so-called “toe” region of the stress-strain curve), the CF take a wavelike configuration, see Figure 2.4, and are easily extended, see Ethier and Simmons (2007); Toshima et al. (2004); Mercer and Crapo (1990). At higher levels of strain (in the “heel” and “linear” region), however, CF become straight and resist further stretch by increasing the stiffness of the fiber significantly. Compared to EF, the Young’s modulus (E) (see Appendix A.2.1) of collagen is about 10,000 to 100,000 times higher (Ethier and Simmons, 2007). Thus, collagen is assumed to provide a mechanical framework to limit excess distension.

Orientation of the Collagen Fibers

Toshima et al. (2004) investigated the fiber structure in rat and human lungs. They found the CF form a continuum, see Figure 2.4, extending throughout the lung and pleura. They are condensed into the alveolar mouths and subdivided into smaller fibers in the alveolar septa, where they form basket-like networks. The fibers are wavy in the collapsed state, whereas they become straight in the inflated state, see Figure 2.4(A) and (B). Furthermore, Mercer and Crapo (1990) investigated the spatial distribution of the fibers in rat and human lungs. They found a high fiber concentration in the alveolar duct walls. Despite the fact that the fibers may have a predominant direction in the individual septum, there is no preferred fiber direction, if a large number of alveoli is considered. Hence, it seems reasonable to assume an isotropic fiber distribution within the lung parenchyma (Sobin et al., 1988).

Elastin Fibers Elastin has a linear stress-strain curve, even for strains larger than 1.5, thus, making it the most “linearly” elastic biosolid material known (Fung and Sobin, 1981). The E of EF is between 30 kPa (Ethier and Simmons, 2007) and 600 kPa (Fung and Sobin, 1981). EF are much softer than CF and can be extended up to 2.3 times their unloaded length (Carton et al., 1962; Weibel, 1986). Elastin provides elasticity to the lung tissue (Fung and Sobin, 1981), allowing the lungs to effectively recoil in the normal breathing range (Ethier and Simmons, 2007). A similar role of EF can be found in arteries, veins, and skin (Fung and Sobin, 1981).

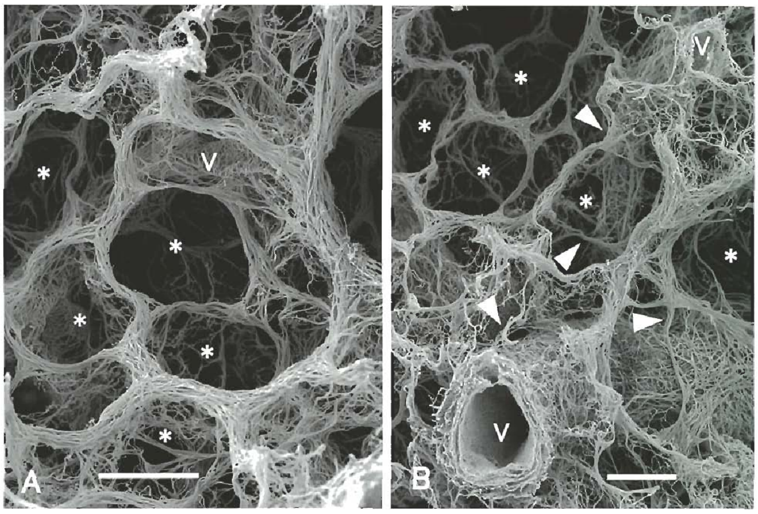

Figure 2.5: Electron micrograph scans of the elastin fiber (EF) network in the human lung. Figures taken from Toshima et al. (2004). The EF form bands at the entrances of the alveoli (*). Blood vessels (V) can also been seen in the scan. Both scale bars correspond to 100 µm.

Orientation of the Elastin Fibers

The orientation of the EF is similar to the CF orientation, except for a band of EF around the alveolar mouth, which forms an entrance ring into the single alveolus (Mercer and Crapo, 1990). Similar to CF, EF do not show a preferred fiber direction, see Figure 2.5, meaning they can be assumed to be distributed isotropically. The EF also form a continuum, with a higher density in the alveolar mouths than in the alveolar septa, however, they were always found to be rather straight than wavy.

Connection Between Collagen and Elastin Fibers Detailed material descriptions based on micro-structural considerations are scarce in the literature.

In ligaments, Brown et al. (1994) found the CF and the EF to be mechanically connected.

Mercer and Crapo (1990) reported very close spatial proximity between EF and CF. They also quantified the percentage of interwoven elastin in rats to be 51 %, leading to the assumption that they are most likely mechanically connected as well.

The close proximity between CF and EF found by Toshima et al. (2004), suggests that both fiber families are mechanically connected. Furthermore, their findings suggest that the two fiber families act as parallel mechanical elements. Similar to Mercer and Crapo (1990), they believe the extension of the connective matrix to be in two stages. At low strain levels, the wavy CF are easily extended and the main stress is carried by the EF. At high strain levels, the CF become straight and act as a limit to further deformations of the tissue.

The review of Faffe and Zin (2009) discusses the influence of the two fiber families on the mechanical behavior of the parenchymal tissue as well as the importance of modeling the fiber-fiber interaction (FF). However, to our best knowledge, none of these contributions have yet been precisely quantified for the parenchymal tissue.

Ground Substance and Other Constituents In the inter cellular space, the two fiber families are embedded in a hydrophilic gel, the ground substance (GS) (Fung and Sobin, 1981). Beside CF and EF, the GS contains proteoglycans and glycosaminoglycans (GAGs). Proteoglycans are macromolecules, consisting of protein cores, to which GAG side chains are covalently attached. The side chains can attract water molecules into the matrix, which can change the material properties of the tissue (Jamal et al., 2001).

2.1.3.3 Capillaries and Gas Exchange

The gas exchange occurs across the alveolar wall. Within the alveolar walls, the capillaries form a dense network, which is almost a continuous sheet of blood. In normal humans, 200 ml of blood are distributed in the total surface area of the alveolar region, which is about $100 - 140\,\mathrm{m}^2$, i.e. approximately the size of a tennis court (Weibel, 1984; Crapo, 2000; West, 2008).

2.1.3.4 Surface Tension and Surfactant

The alveoli are lined with a thin liquid film, which creates a surface tension acting against an increase of alveolar surface area. When an interface is expanded, the minimum amount of work required to create the additional surface area is the product of the inter-facial tension and the increase in area of the interface. This surface tension leads, amongst other phenomena, to a hysteresis between pressure-volume (p-V) curves for inflation and deflation.

In the alveolar wall there are two types of alveolar epithelial cells (type I and II). Type II cells are responsible for the production of surfactant, a surface active agent. Surfactant reduces the surface tension of the liquid lining at the tissue-gas interface (see Figure 2.3) and thereby, significantly changes the amount of work required to expand those surfaces (Rosen, 2004; West, 2008). Its absence drastically reduces the compliance of the lung (West, 2008).

2.2 Physiology and Pathology of the Lung

In this section a short overview over healthy respiration is given, before introduction the diseases ALI and ARDS and therefrom resulting VALI.

2.2.1 Respiration

During inspiration, the volume of the thoracic cavity is increased by lifting the rib cage and contracting the diaphragm. This causes the pressure in the pleural space to drop to more negative values causing air to flow into the lungs. The air flows down to the terminal bronchioles. At this point, the overall cross-sectional area is so big, due to the large number of branches, that the convective velocity of the gas becomes very small and diffusion takes over in the respiratory zone (West, 2008). During expiration, the diaphragm relaxes, which increases the pressure in the pleural space, resulting in airflow out of the lungs.

A number of clinically measured volumes are defined in Figure 2.6. The total lung capacity (TLC), which is the maximum air volume in the lung, is between 6 and 8 l in a healthy adult. However, during normal breathing only 0.5 l (tidal volume) are exchanged. Taking a deep breath, the whole vital capacity can be exchanged. The residual volume, including the anatomical dead space, is the volume remaining in the lung after maximal expiration

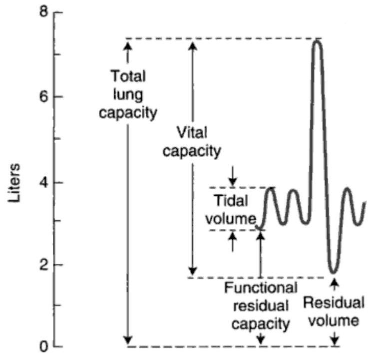

Figure 2.6: Lung volumes and capacities for normal humans. Figure taken from West (2008).

(∼ 1.21). The functional residual capacity (FRC) is the volume of air in the lung after passive expiration (Ethier and Simmons, 2007; West, 2008).

2.2.2 Acute Lung Injury and Acute Respiratory Distress Syndrome

ARDS and its lighter form ALI are both severe forms of diffuse lung disease. A variety of direct and indirect triggers, e.g. aspiration, inhalation of chemicals, pneumonia, septic shock, or trauma, lead to this condition. Both forms are characterized by inflammation of the lung parenchyma leading to reduced gas exchange. For this reason, the patients usually require mechanical ventilation and admission to an intensive care unit. Associated phenomena are the systemic release of inflammatory mediators causing inflammation of other organs, hypoxemia, i.e. reduction of oxygen transfer into the arterial blood stream, and frequently resulting in multiple organ failure. However, due to the fact that ARDS/ALI are syndromes, rather than diseases, a precise definition is difficult and has changed over the years.

The first definition was given in 1967 by Ashbaugh et al. (1967). They defined ARDS to have the following symptoms:

- dyspnea (shortness of breath),
- tachypnea (rapid breathing),
- hypoxemia (deficient oxygenation of the blood), and
- loss of compliance of the lung tissue.

In 1991, the American-European consents conference on ARDS was held, in order to establish a clear and uniform definition. Their specifically recommended criteria are, amongst others,

- the acute onset,
- bilateral infiltration, seen on the front chest radiograph,
- a threshold value for the oxygenation (different values for ALI and ARDS), and
- a threshold value for the hypertension (different values for ALI and ARDS).

The details can be found in the consents report, see Bernard et al. (1994).

Due to the wide range of definitions, the reported mortality rates vary between 10 and 90 %.

2.2.2.1 Pathogenesis

There is a great diversity of initiating causes of ALI and ARDS, like sepsis, trauma, aspiration, multiple blood transfusion, acute pancreatitis, inhalation injury, and drug toxicity. Although the initiating injury might be different, the resulting inflammation causes the injury to propagate, especially when it is paired with additional trauma, like high-tidal volume of the mechanical ventilation or hypoxemia, see section 2.2.3.

The pathogenesis of ARDS can be split into two phases:

- the earlier exudate phase, also called the acute inflammation; and
- the later fibrosing-alveolitis phase,

see Figure 2.7.

In the first phase, the alveolar wall barrier becomes more permeable, leading to an inflow of fluid and neutrophils into the alveolar air space. As mentioned above, the alveolar wall consists, amongst others, of capillary endothelial and alveolar epithelial cells, the damage of which, could have a variety of reasons, results in ARDS. Injury of the endothelium (e.g. in case of sepsis) increases the capillary permeability, leading to an influx of protein-rich fluid into the alveolar space (see Figure 2.7). Injury of the alveolar epithelium also leads to the formation of pulmonary edema. As mentioned above, there are two types of alveolar epithelial cells. The alveolar type I cells are at high risk of damage. Their damage leads to an increased inflow of fluid into the alveoli and a decreased clearance of this fluid from the alveolar space. The alveolar type II cells are more resistant to damage; however, they have, amongst others, the task of producing surfactant, transporting ions, and the proliferation and differentiation into type I cells to replace them after injury. Injury of type II cells can lead to a reduced production of surfactant molecules, which increases the surface tension (see section 2.1.3.4), resulting in a decrease of compliance and alveolar collapse.

In the second phase, the alveolar wall gets transparent, with varying degrees of interstitial fibrosis, leading to the resolution of the individual walls (Tsushima et al., 2009; Harman, 2011).

2.2.2.2 Treatment

The standard treatment of ALI and ARDS is towards identification and management of pulmonary and non-pulmonary dysfunction. In some cases, the underlying cause can be treated directly, e.g. in the case of pneumonia. However, the majority of cases, e.g. aspiration, cannot be treated except to provide essential supportive care.

Most ALI and ARDS patients develop a life-threatening hypoxemia. Furthermore, the high breathing effort caused by the reduced lung compliance may lead to ventilatory failure. For these reasons, mechanical ventilation is the mainstay of the supportive care. The stabilization of the respiration allows time for the evolution of the natural healing process and, if possible, the treatment of the underlying cause (Brower et al., 2001).

2.2.3 Ventilator Associated Lung Injuries

Although mechanical ventilation is a lifesaving treatment, it can cause further lung damage itself. These injuries are called ventilator-induced lung injury (VILI) or ventilator associated lung injury (VALI).

VILI is defined as an acute lung injury directly caused by mechanical ventilation, whereas in VALI, the injury is not necessarily caused by mechanical ventilation but is associated with it. This means VALI is a lung injury that comes along with diseases like ARDS, where mechanical ventilation is a mandatory treatment (American Thoracic Society, European Society of Intensive Care Medicine, Societé de Réanimation Langue Française, 1999).

2.2.3.1 Pathogenesis

VALI damage the lung in an inhomogeneous manner. Supposedly healthy alveoli, which are more compliant than affected alveoli, are at risk of becoming over distended during mechanical ventilation. Furthermore, affected alveoli may experience further injury due to shear forces arising from a cycle of collapse and re-expansion during the breathing cycle. In addition to mechanical damage, mechanical stimulation causes the cells to secrete proinflammatory cytokines, leading to an increase of inflammation and pulmonary edema.

The clinical course of VALI is different; while some patients recover within a couple of weeks, others need a long therapy, including mechanical ventilation. These patients face the risk of superimposed infections or multi-organ failure, leading to the high mortality rates (American Thoracic Society, European Society of Intensive Care Medicine, Societé de Réanimation Langue Française, 1999). The majority of patients suffering from VALI do not die of primary respiratory causes rather of sepsis or multi-organ dysfunction (Ware and Matthay, 2000).

2.2.3.2 Prophylaxis and Treatment

The use of protective ventilation protocols, including positive end-expiatory pressure (PEEP) to prevent alveolar collapse, the use of low tidal volumes, and limited levels of inspiratory filling pressures appear to be beneficial in diminishing the observed VALI. The change of “normal” mechanical ventilation to these protocols reduced the mortality rates from $55 - 65\,\%$, as reported in the 1980s and early 1990s, to $31\,\%$ (Abel et al., 1998; Tsushima et al., 2009). This indicates that some cases were related to lung injury due to VALI. A more effective treatment of sepsis and improvement in the supportive care of critically ill patients also influenced this reduction.

Dreyfuss et al. (1988) studied the effects of different ventilation strategies on pulmonary edema, i.e. the respective effects of high airway pressure and high inflation with and without PEEP on the water content, micro-vascular permeability, and ultra-structure of the lungs on mechanically ventilated rats. They found, that the edema was only related to changes in the lung volume and not the airway pressure.

Additionally, they found PEEP to:

- have a positive effect on the alveolar epithelial layer,
- prevent the animals from edema or reduce the amount of edema, and
- improve the arterial oxygenation during pulmonary edema.

The protein concentration within the edema fluid remained the same and the lung water was not decreased by PEEP, sometimes it even increased.

2.2.3.3 Conclusion

Despite these improvements, the mortality rates remain unacceptably high. A better understanding of the connection between mechanical ventilation and implications of overstraining the alveolar tissue is essential.

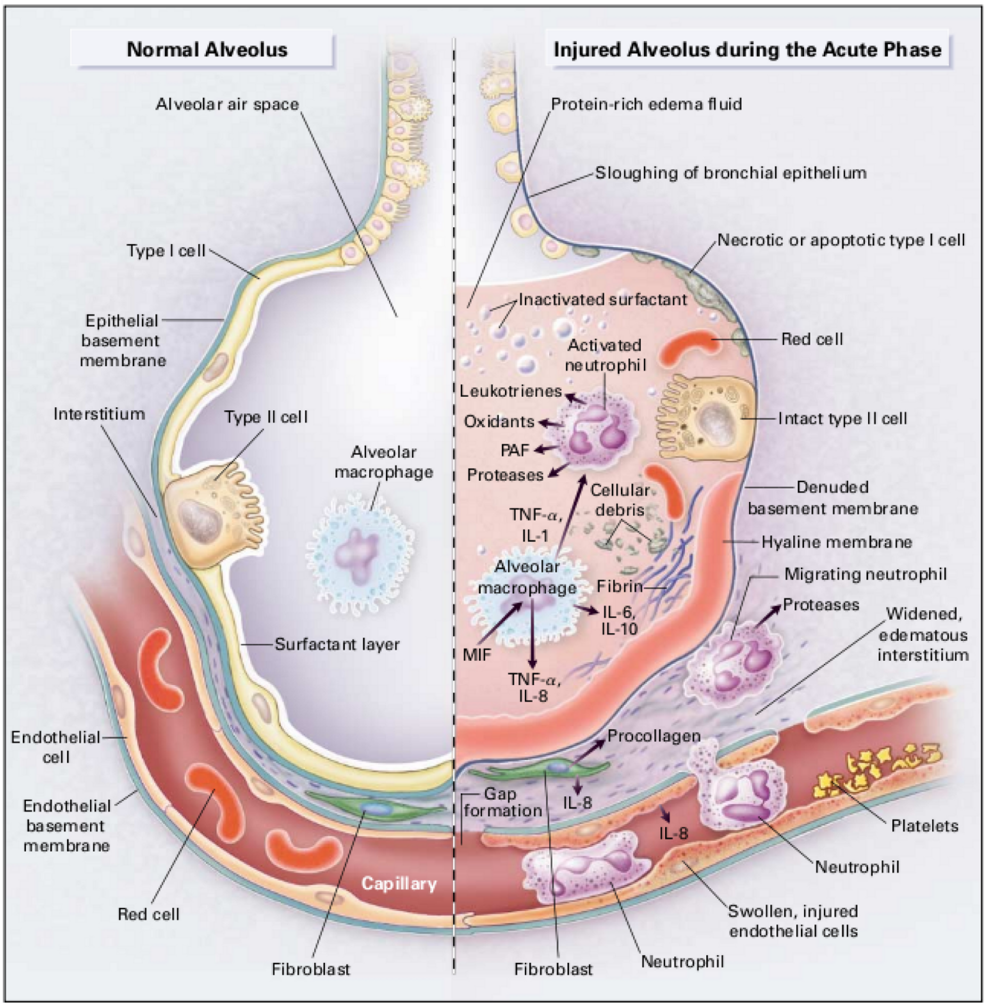

Figure 2.7: Normal alveolus (left) and injured alveolus in the exudate or acute phase of ALI and ARDS (right). Neutrophils migrate through the injured capillary endothelium via the interstitium into the airspace, which is filled with edema fluid. The influx of the fluid in the alveolar space leads to the inactivation of surfactant. Figure taken from Ware and Matthay (2000).

3 Theoretical Framework

This chapter provides the necessary theoretical background knowledge to understand this work. In the first section a brief introduction into solid continuum mechanics is presented. In the second section the theoretical framework for hyperelastic material models is introduced.

3.1 Solid Continuum Mechanics

In continuum mechanics, a body $\mathcal{B}$ is considered as a continuous object. The fact that it is actually built of discrete constituents, like atoms and molecules, is neglected. This assumption is valid if there is a large scale difference between the macro-scale, i.e. the continuous body, and the micro-scale, i.e. the molecules or atoms.

The theory of continuum mechanics is applicable for both solid and fluid mechanics and not limited to Cartesian coordinates. However, here, the focus is restricted to solid mechanics in Cartesian coordinates.

The aim of this section is to give a brief overview of the continuum mechanical background of this work and to introduce the used notation. For a detailed background, the reader is referred to Wall et al. (2010a) and Holzapfel (2004).

3.1.1 Kinematics

In the undeformed or material configuration, the body $\mathcal{B}_0 \subset \mathbb{R}^3$ is parametrized with $\mathbf{X}$. In the deformed, current, or spatial configuration, the body $\mathcal{B}_t \subset \mathbb{R}^3$ at $t \in \mathbb{R}_+$ is parametrized with $\mathbf{x}$. The boundary of $\mathcal{B}$ is denoted with $\partial\mathcal{B}$. The motion of the body $\mathcal{B}$ is described by the particle motion mapping $\boldsymbol{\varphi}(\mathbf{X}, t) : \mathcal{B}_0 \rightarrow \mathcal{B}_t$, which relates the points $\mathbf{X} \in \mathcal{B}_0$ with the points $\mathbf{x} \in \mathcal{B}_t$ at a fixed time $t \in \mathbb{R}_+$, i.e.

$$\mathbf{x} = \boldsymbol{\varphi}(\mathbf{X}, t). \tag{3.1.1}$$

The transformation is invertible with

$$\mathbf{X} = \boldsymbol{\varphi}^{-1}(\mathbf{x}, t). \tag{3.1.2}$$

The partial derivative of $\boldsymbol{\varphi}$ with respect to $\mathbf{X}$ is one of the most important kinematic quantities. The resulting tensor

$$\nabla_{\mathbf{X}}\boldsymbol{\varphi} := \frac{\partial \mathbf{x}}{\partial \mathbf{X}} = \begin{bmatrix} \frac{\partial x^1}{\partial X^1} & \frac{\partial x^1}{\partial X^2} & \frac{\partial x^1}{\partial X^3} \\ \frac{\partial x^2}{\partial X^1} & \frac{\partial x^2}{\partial X^2} & \frac{\partial x^2}{\partial X^3} \\ \frac{\partial x^3}{\partial X^1} & \frac{\partial x^3}{\partial X^2} & \frac{\partial x^3}{\partial X^3} \end{bmatrix} := \mathbf{F}(\mathbf{X}, t) \tag{3.1.3}$$

is called deformation gradient $\mathbf{F}$. In order to be invertible the deformation gradient $\mathbf{F}$, it needs to be non-singular, i.e.

$$J = \det\mathbf{F} \neq 0 \tag{3.1.4}$$

with J being the determinant of the deformation gradient or the Jacobian determinant. In that case the inverse motion $\boldsymbol{\varphi}^{-1}$ with respect to the current position $\mathbf{x}$ of a material point exists, the inverse deformation gradient $\mathbf{F}^{-1}$ reads

$$\mathbf{F}^{-1} = \mathbf{F}^{-1}(\mathbf{x}, t) := \nabla_{\mathbf{x}}\boldsymbol{\varphi}^{-1} = \frac{\partial \mathbf{X}}{\partial \mathbf{x}} = \begin{bmatrix} \frac{\partial X^1}{\partial x^1} & \frac{\partial X^1}{\partial x^2} & \frac{\partial X^1}{\partial x^3} \\ \frac{\partial X^2}{\partial x^1} & \frac{\partial X^2}{\partial x^2} & \frac{\partial X^2}{\partial x^3} \\ \frac{\partial X^3}{\partial x^1} & \frac{\partial X^3}{\partial x^2} & \frac{\partial X^3}{\partial x^3} \end{bmatrix}. \tag{3.1.5}$$

Based on the deformation gradient, there are three fundamental geometric mappings. The deformation gradient $\mathbf{F}$ itself defines a linear transformation of an infinitesimal line element $\mathrm{d}\mathbf{X} \in \mathcal{B}_0$ in the material configuration to an infinitesimal line element $\mathrm{d}\mathbf{x} \in \mathcal{B}_t$ in the current configuration, i.e.

$$\mathrm{d}\mathbf{x} = \mathbf{F}\mathrm{d}\mathbf{X}. \tag{3.1.6}$$

Due to the fact that the deformation gradient $\mathbf{F}$ transforms points between two configurations, it is also called *two-point tensor*.

The change of volume of an infinitesimal volume element in the material configuration $\mathrm{d}V \subset \mathcal{B}_0$ and the current configuration $\mathrm{d}v \subset \mathcal{B}_t$ at time t is defined as

$$\mathrm{dv} = J\mathrm{dV} = \det(\mathbf{F})\mathrm{dV}. \tag{3.1.7}$$

For this reason, the Jacobian determinant J is also called the volume ratio. Since $\mathbf{F}$ is invertible and the volume elements cannot have negative volumes, the determinant J needs to be positive. An isochoric or volume preserving deformation is characterized by $J = 1$. In order to transform vector elements of infinitesimal area $\mathbf{n}\,\mathrm{d}a \subset \mathcal{B}_t$ and $\mathbf{N}\,\mathrm{d}A \subset \mathcal{B}_0$ in the current and the material configuration, respectively, with $\mathbf{n}$ and $\mathbf{N}$ being the material and spatial unit normal vector of the area element, respectively, the Nanson's formula is used, i.e.

$$\mathbf{n}\,\mathrm{d}a = J\mathbf{F}^{-T}\mathbf{N}\,\mathrm{d}A. \tag{3.1.8}$$

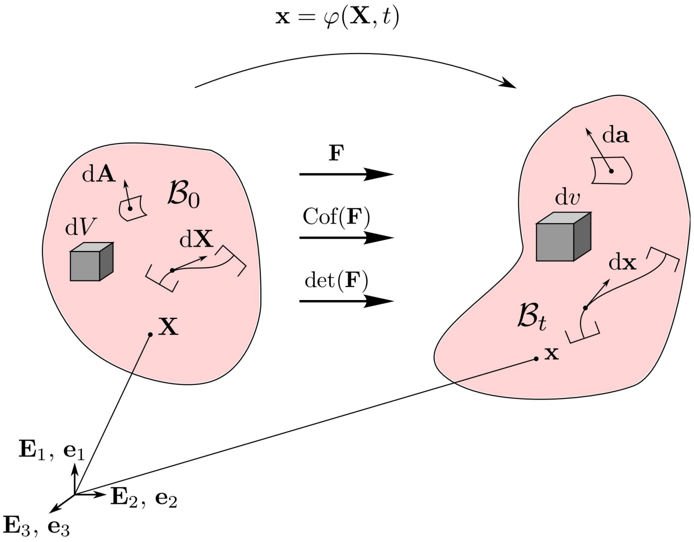

Figure 3.1: Material and current configuration with corresponding geometric mapping.

The displacement fields in the current and in the material configuration, $\mathbf{u}(\mathbf{x},t)$ and $\mathbf{U}(\mathbf{X},t)$, respectively, are defined as

$$\mathbf{u}(\mathbf{x},t) = \mathbf{x} - \mathbf{X}(\mathbf{x},t) \quad \text{and} \quad \mathbf{U}(\mathbf{X},t) = \mathbf{x}(\mathbf{X},t) - \mathbf{X}. \tag{3.1.9}$$

In order to determine the velocity fields in the current and in the material configuration, $\mathbf{v}(\mathbf{x},t)$ and $\mathbf{V}(\mathbf{X},t)$, respectively, the rate of change of the spatial position $\mathbf{x}(\mathbf{X},t)$ of a point $\mathbf{X} \in \mathcal{B}_0$, are calculated by

$$\mathbf{v}(\mathbf{x},t) := \mathbf{V}(\mathbf{X},t) = \frac{\mathrm{d}\mathbf{x}(\mathbf{X},t)}{\mathrm{d}t} = \frac{\partial \mathbf{x}(\mathbf{X},t)}{\partial t} = \dot{\mathbf{x}}(\mathbf{X},t). \tag{3.1.10}$$

The material velocity field $\mathbf{V}(\mathbf{X},t)$ at a material point $\mathbf{X}$ is by definition identical to the spatial velocity field $\mathbf{v}(\mathbf{x},t)$ at the spatial point $\mathbf{x}$. The total derivative of the velocity field, with respect to the time t, defines the acceleration field. The acceleration field in the current and the material configuration $\mathbf{a}(\mathbf{x},t)$ and $\mathbf{A}(\mathbf{X},t)$, respectively, are calculated by

$$\mathbf{A}(\mathbf{X},t) = \mathbf{a}(\mathbf{x},t) = \frac{\mathrm{d}\mathbf{V}(\mathbf{X},t)}{\mathrm{d}t} = \frac{\mathrm{d}^2\mathbf{x}(\mathbf{X},t)}{\mathrm{d}^2 t} \tag{3.1.11}$$

or, equivalently,

$$\mathbf{a}(\mathbf{x},t) = \dot{\mathbf{v}}(\mathbf{x},t) = \frac{\mathrm{d}\mathbf{v}(\mathbf{x},t)}{\mathrm{d}t} = \underbrace{\frac{\partial\mathbf{v}(\mathbf{x},t)}{\partial t}}_{\text{partial derivative}} + \underbrace{(\nabla_{\mathbf{x}}\mathbf{v})\cdot\mathbf{v}}_{\text{convective derivative}} \quad . \tag{3.1.12}$$

The partial and the convective derivative are also called the local and convective acceleration, respectively.

3.1.2 Strain and Stress Measures

In order to determine the volume and shape change of a body, displacements are not sufficient. For this reason, strain measures based on the deformation gradient $\mathbf{F}$ are introduced in the following. The polar decomposition of the deformation gradient reads

$$\mathbf{F} = \mathbf{R}\tilde{\mathbf{U}} = \tilde{\mathbf{v}}\mathbf{R}, \tag{3.1.13}$$

with $\mathbf{R}$ being a rotation tensor, i.e. an orthogonal tensor ($\mathbf{R}^{-1} = \mathbf{R}^T$) and $\tilde{\mathbf{U}}$ and $\tilde{\mathbf{v}}$ are the symmetric right and left stretch tensors, respectively. For this reason, the deformation gradient $\mathbf{F}$ is not invariant with respect to rigid body rotations, in contrast to the right Cauchy-Green strain tensor

$$\mathbf{C} := \mathbf{F}^T\mathbf{F} = \tilde{\mathbf{U}}^T \underbrace{\mathbf{R}^T\mathbf{R}}_{\mathbf{1}} \tilde{\mathbf{U}} = \tilde{\mathbf{U}}^T\tilde{\mathbf{U}}, \tag{3.1.14}$$

with $\mathbf{1}$ being the second-order identity tensor. The strain tensor $\mathbf{C}$ exclusivly depends on the right stretch tensor $\tilde{\mathbf{U}}$ and, is therefore, well suited for describing the internal state of a body. Similar to the right Cauchy-Green strain tensor, the left Cauchy-Green strain tensor $\mathbf{b}$ is given as

$$\mathbf{b} = \mathbf{F}\mathbf{F}^T = \tilde{\mathbf{v}}^T\tilde{\mathbf{v}}. \tag{3.1.15}$$

In many cases, it is usefully to have a strain measure, that is zero for the undeformed configuration ($\mathbf{F} = \mathbf{1}$). For this reason the Green-Lagrange strain tensor $\mathbf{E}$ and the Euler-Almansi strain tensor $\mathbf{e}$ are given as

$$\mathbf{E} := \frac{1}{2}(\mathbf{C} - \mathbf{1}) = \frac{1}{2}\left(\mathbf{F}^T\mathbf{F} - \mathbf{1}\right) \tag{3.1.16}$$

and

$$\mathbf{e} := \frac{1}{2}\left(\mathbf{1} - \mathbf{b}^{-1}\right). \tag{3.1.17}$$

The Green-Lagrange strain tensor $\mathbf{E}$ and the right Cauchy-Green strain tensor $\mathbf{C}$ are defined in the material configuration and are material objective, whereas the Euler-Almansi strain tensors $\mathbf{e}$ and the left Cauchy-Green $\mathbf{b}$ are defined in the current configuration and are spatial objective.

Table 3.1: Selection of different strain measures.

Strain Measure	Definition
Right Cauchy-Green	$\mathbf{C} := \mathbf{F}^T\mathbf{F} = \tilde{\mathbf{U}}^T\tilde{\mathbf{U}}$
Left Cauchy-Green	$\mathbf{b} = \mathbf{F}\mathbf{F}^T = \tilde{\mathbf{v}}^T\tilde{\mathbf{v}}$
Green-Lagrange	$\mathbf{E} := \frac{1}{2}(\mathbf{C} - \mathbf{1})$
Euler-Almansi	$\mathbf{e} := \frac{1}{2}\left(\mathbf{1} - \mathbf{b}^{-1}\right)$

An overview over the most common strain measures can be found in Table 3.1. It is important to note that due to the fact, that strain is not a physical quantity, other strain measures could possibly be used.

The objective material strain rate, calculated from the Green-Lagrange strain tensor $\mathbf{E}$, is

$$\dot{\mathbf{E}} = \frac{\mathrm{d}}{\mathrm{d}t}\left(\frac{1}{2}(\mathbf{C} - \mathbf{1})\right) = \frac{\mathrm{d}}{\mathrm{d}t}\left(\frac{1}{2}\left(\mathbf{F}^T\mathbf{F} - \mathbf{1}\right)\right) = \frac{1}{2}\left(\dot{\mathbf{F}}^T\mathbf{F} + \mathbf{F}^T\dot{\mathbf{F}}\right) = \frac{1}{2}\dot{\mathbf{C}}. \tag{3.1.18}$$

The other possible strain rates can be defined accordingly and are not shown.

To describe the internal stress state of a body, the surface traction vector $\mathbf{t}$ is introduced as

$$\mathbf{t}(\mathbf{x}, t) = \lim_{\Delta a \to 0} \frac{\Delta \mathbf{f}}{\Delta a} = \frac{\mathrm{d}\mathbf{f}}{\mathrm{d}a}, \tag{3.1.19}$$

with $\Delta\mathbf{f}$ being the resultant force acting on an area element $\Delta a \subset \partial\mathcal{B}_t$, including the point $\mathbf{x} \in \partial\mathcal{B}_t$. According to Cauchy's fundamental lemma, there exists a uniquely defined second-order stress field $\boldsymbol{\sigma}$, such that

$$\mathbf{t}(\mathbf{x}, t, \mathbf{n}) = \boldsymbol{\sigma}(\mathbf{x}, t) \cdot \mathbf{n}. \tag{3.1.20}$$

The tensor $\boldsymbol{\sigma}$ is called Cauchy stress tensor. Due to the fact that the Cauchy stress tensor $\boldsymbol{\sigma}$ refers to an unknown configuration, alternative stress measures were introduced. The 1st Piola-Kirchhoff stress tensor $\mathbf{P}$ is given as uniquely defined tensor field with

$$\mathbf{T} = \mathbf{P}\mathbf{N} \tag{3.1.21}$$

with $\mathbf{T} = \frac{\mathrm{d}a}{\mathrm{d}A}\mathbf{t}$ being the pseudo-traction vector. The Cauchy stress tensor $\boldsymbol{\sigma}$ can be restated to the 1st Piola-Kirchhoff stress tensor $\mathbf{P}$ by

$$\mathbf{P} = \det\mathbf{F}\boldsymbol{\sigma}\mathbf{F}^{-T}. \tag{3.1.22}$$

The 1st Piola-Kirchhoff stress tensor $\mathbf{P}$ is a two-point tensor, i.e. it is defined in both configurations. In contrast, the 2nd Piola-Kirchhoff stress tensor

$$\mathbf{S} = \mathbf{F}^{-1}\mathbf{P} = \det\mathbf{F}\mathbf{F}^{-1}\boldsymbol{\sigma}\mathbf{F}^{-T}, \tag{3.1.23}$$

which is defined solely in the material configuration. The interpretation of the 1st and the 2nd Piola-Kirchhoff stress tensor are not trivial. However, they are frequently used because they refer to the *a priori* known material configuration. For this reason, in the following, especially in chapter 6, the term stress will be used as an equivalent to the 2nd Piola-Kirchhoff stress $\mathbf{S}$. An overview over the most common stress measures can be found in Table 3.2.

Table 3.2: Selection of different stress measures.

Stress Measure	Symbol	Definition	Conversion
Cauchy	$\boldsymbol{\sigma}$	$\mathbf{t} = \boldsymbol{\sigma}\mathbf{n}$	
1st Piola-Kirchhoff	$\mathbf{P}$	$\mathbf{T} = \mathbf{P}\mathbf{N}$	$\mathbf{P} = \det\mathbf{F}\boldsymbol{\sigma}\mathbf{F}^{-T}$
2nd Piola-Kirchhoff	$\mathbf{S}$		$\mathbf{S} = \mathbf{F}^{-1}\mathbf{P} = \det\mathbf{F}\mathbf{F}^{-1}\boldsymbol{\sigma}\mathbf{F}^{-T}$

3.1.3 Balance Principles

Conservation laws and balance principles are the physical basis of continuum mechanics. They are material independent, i.e. valid for every continuum. In detail, there are four balance equations and one inequality. The balance equations are the conservation of mass, the balance of linear momentum, the balance of angular momentum, and the balance of energy. The entropy inequality will be further discussed in more detail in the following section 3.2.

3.1.3.1 Conservation of Mass

The law of conservation of mass states that, in a closed system, the mass M of the body $\mathcal{B}$ remains constant during a deformation process. The first global form is given as

$$M := \int_{\mathcal{B}_0} \underbrace{\rho_0(\mathbf{X})\,\mathrm{d}V}_{\mathrm{d}M} = \int_{\mathcal{B}_t} \underbrace{\rho(\mathbf{x},t)\,\mathrm{d}v}_{\mathrm{d}m} = m = const., \tag{3.1.24}$$

where ρ_0 and ρ are the material and current density, respectively. Using equation (3.1.7), the first local form is derived to be

$$\rho_0 = J\rho. \tag{3.1.25}$$

Since the mass does not change over time ($\dot{m} = 0$), the first global form can be equally written as

$$\dot{m} = 0 = \frac{\mathrm{d}}{\mathrm{d}t}\int_{\mathcal{B}_t} \rho\,\mathrm{d}v = \int_{\mathcal{B}_t} (\dot{\rho} + \rho\nabla\cdot\mathbf{v})\,\mathrm{d}v, \tag{3.1.26}$$

where the Reynolds transport theorem has been applied, see Appendix A.1.1.

The corresponding local forms reads

$$\dot{\rho} + \rho\nabla\cdot\mathbf{v} = 0. \tag{3.1.27}$$

3.1.3.2 Balance of Momentum

The balance of momentum state that the change over time of the linear momentum $\mathbf{L}$ and the angular momentum $\mathbf{J}_{\mathbf{Y}}$ equal the external forces $\mathbf{f}_0^{\mathrm{ext}}$ and the external momentum $\mathbf{m}_0^{\mathrm{ext}}$, respectively.

Balance of Linear Momentum The linear momentum $\mathbf{L}$ is defined as

$$\mathbf{L} := \int_{\mathcal{B}_0} \rho_0 \mathbf{V} \, \mathrm{d}V. \tag{3.1.28}$$

The change of linear momentum $\dot{\mathbf{L}}$ in time leads to

$$\dot{\mathbf{L}} = \mathbf{f}_0^{\text{ext}} := \int_{\mathcal{B}_0} \mathbf{f}_V^{\text{body}} \, \mathrm{d}V + \int_{\partial\mathcal{B}_0} \mathbf{T} \, \mathrm{d}A \tag{3.1.29}$$

where $\mathbf{f}_V^{\text{body}}$ is the material volume type body load. With some lengthy transformations, including Gauss' divergence theorem, see Appendix A.1.2, it is derived as

$$\int_{\mathcal{B}_0} \rho_0 \dot{\mathbf{V}} \, \mathrm{d}V = \int_{\mathcal{B}_0} \left(\mathbf{f}_V^{\text{body}} + \nabla \cdot (\mathbf{F} \cdot \mathbf{S}) \right) \mathrm{d}V. \tag{3.1.30}$$

The local material form of this equation reads

$$\nabla \cdot (\mathbf{F} \cdot \mathbf{S}) + \mathbf{f}_V^{\text{body}} - \rho_0 \dot{\mathbf{V}} = \mathbf{0}. \tag{3.1.31}$$

This equation is called the linear momentum equation or Cauchy's first equation of motion and is the starting point of the numerical method.

Balance of Angular Momentum The angular momentum relative to a fixed point (characterized by the position vector $\mathbf{Y}$) is defined as

$$\mathbf{J}_{\mathbf{Y}} := \int_{\mathcal{B}_0} \tilde{\mathbf{R}} \times \rho_0 \mathbf{V} \, \mathrm{d}V \tag{3.1.32}$$

with the identity of the velocity fields (equation (3.1.10)) and the position vector $\tilde{\mathbf{R}} = \mathbf{X} - \mathbf{Y}$. The change of angular momentum $\dot{\mathbf{J}}_{\mathbf{Y}}$ with respect to time leads to

$$\dot{\mathbf{J}}_{\mathbf{Y}} = \mathbf{m}_0^{\text{ext}} := \int_{\partial\mathcal{B}_0} \tilde{\mathbf{R}} \times \mathbf{T} \, \mathrm{d}A + \int_{\mathcal{B}_0} \tilde{\mathbf{R}} \times \mathbf{f}_V^{\text{body}} \, \mathrm{d}V. \tag{3.1.33}$$

With a lengthy transformation, Cauchy's second equation of motion results in

$$\mathbf{S} = \mathbf{S}^T \tag{3.1.34}$$

or

$$\boldsymbol{\sigma} = \boldsymbol{\sigma}^T. \tag{3.1.35}$$

Thus, the balance of angular momentum is satisfied if the Cauchy stress tensor $\boldsymbol{\sigma}$ and the 2^{nd} Piola-Kirchhoff stress tensor $\mathbf{S}$ are symmetric.

3.1.3.3 Balance of Energy (First Principle of Thermodynamics)

The change over time of the sum of the internal energy ϵ_{int} and kinetic energy ϵ_{kin} equals the sum of the external mechanical power $\mathcal{P}_{\text{ext}}$ and the non-mechanical power $\mathcal{Q}_{\text{ext}}$

$$\frac{\mathrm{d}}{\mathrm{d}t}\left(\epsilon_{\text{int}} + \epsilon_{\text{kin}}\right) = \mathcal{P}_{\text{ext}} - \mathcal{Q}_{\text{ext}}. \tag{3.1.36}$$

Since only mechanical effect are considered within this work, $\mathcal{Q}_{\text{ext}}$ is set to zero. For simplicity, in the following the summands are given in the material configuration. In detail, equation (3.1.36) can be reformed as

$$\frac{\mathrm{d}}{\mathrm{d}t}\left(\underbrace{\int_{\mathcal{B}_0} \epsilon_{\text{int},\,M}\rho_0 \,\mathrm{d}V}_{\epsilon_{\text{int}}} + \underbrace{\int_{\mathcal{B}_t} \frac{1}{2}\rho_0\left(\mathbf{V}\cdot\mathbf{V}^T\right)\mathrm{d}V}_{\epsilon_{\text{kin}}}\right) = \underbrace{\int_{\partial\mathcal{B}_0} \mathbf{T}\cdot\mathbf{V}^T \,\mathrm{d}A + \int_{\mathcal{B}_0} \mathbf{f}_V^{\text{body}}\cdot\mathbf{V}^T \,\mathrm{d}V}_{\mathcal{P}_{\text{ext}}} \tag{3.1.37}$$

with $\epsilon_{\text{int},\,M}$ being the specific internal energy, i.e. internal energy per unit mass. With some transformations, the local form reads

$$\mathbf{S} : \dot{\mathbf{E}} + \rho_0\left(\dot{\mathbf{V}}\cdot\mathbf{V}^T\right) = \nabla\cdot\left(\left(\mathbf{S}:\dot{\mathbf{E}}\right)\cdot\mathbf{V}^T\right) + \mathbf{f}_V^{\text{body}}\cdot\mathbf{V}^T. \tag{3.1.38}$$

3.1.3.4 Initial and Boundary Conditions

In order to solve the differential equation (3.1.31) initial and boundary conditions are required. The boundary conditions account for the external stresses and displacements on $\mathcal{B}$ and the initial conditions define the stresses and displacements for the material state.

The initial conditions are given as

$$\mathbf{u}(\mathbf{x}, t_0) = \hat{\mathbf{u}}_0(\mathbf{x}) \tag{3.1.39}$$

and

$$\mathbf{v}(\mathbf{x}, t_0) = \hat{\mathbf{v}}_0(\mathbf{x}) \tag{3.1.40}$$

on the Dirichlet boundary $\mathcal{B}_0$. Prescribed displacements $\hat{\mathbf{u}}_0$ and an initial velocity $\hat{\mathbf{v}}_0$ are needed, since equation (3.1.31) is a second-order differential equation of the time.

The boundary conditions are given as

$$\mathbf{S} \cdot \mathbf{N} = \hat{\mathbf{T}}, \tag{3.1.41}$$

on the Neumann boundary $\partial_{\mathbf{S}}\mathcal{B}_0$,

and

$$\mathbf{u} = \hat{\mathbf{u}} \tag{3.1.42}$$

on the Dirichlet boundary $\partial_{\mathbf{u}}\mathcal{B}_0$. It is important to note that every point of $\partial\mathcal{B}_0$ needs to be assigned to either a stress or displacement boundary condition, i.e. $\partial_{\mathbf{S}}\mathcal{B}_0 \cup \partial_{\mathbf{u}}\mathcal{B}_0 = \partial\mathcal{B}_0$ and $\partial_{\mathbf{S}}\mathcal{B}_0 \cap \partial_{\mathbf{u}}\mathcal{B}_0 = \emptyset$.

3.2 Constitutive Equations for Hyperelastic Materials

The second law of thermodynamics states that heat always flows from the warmer to the colder region of a body; friction converts mechanical energy into heat, which cannot be converted back into mechanical energy. Based on this principle, the Clausius-Planck Inequality is

$$\mathcal{D}_{\text{int}} = \mathbf{S} : \dot{\mathbf{E}} - \rho_0 \dot{\Psi}_M + T \rho_0 \dot{\mathcal{S}}_M \geq 0 \tag{3.2.1}$$

with the internal dissipation $\mathcal{D}_{\text{int}}$, the specific Helmholtz free energy Ψ_M which is a measure for the work per unit mass obtainable from a closed thermodynamic system at constant temperature and volume, the absolute temperature T and the specific entropy $\mathcal{S}_M$. The contraction $\mathbf{S} : \dot{\mathbf{E}}$ is the rate of internal mechanical work or stress-power per unit reference volume. The absolute temperature multiplied by the rate of entropy $\rho_0 \dot{\mathcal{S}}_M T$ is zero for this adiabatic process. This leads to the reversible process of

$$\mathcal{D}_{\text{int}} = \mathbf{S} : \dot{\mathbf{E}} - \rho_0 \dot{\Psi}_M = 0. \tag{3.2.2}$$

In the following, this study is restricted to *Green-elastic* or *hyperelastic* materials. In this case, the Helmholtz free energy Ψ_M solely depends on the current state of deformation relative to an arbitrary material configuration. Besides this, the work needed to get to a particular state of deformation is path independent. Consequently, the stress is derivable from a scalar potential function, the strain energy density function (SEF) Ψ_v, defined as

$$\Psi_\text{v} = \rho_0 \Psi_M. \tag{3.2.3}$$

For homogeneous materials, the SEFs solely depend on the Green-Lagrange stress tensor $\mathbf{E}$, i.e. $\Psi_\text{v} = \Psi_\text{v}(\mathbf{E})$. With the material time derivation of Ψ_v being

$$\dot{\Psi}_\text{v}(\mathbf{E}(\mathbf{X},t)) = \frac{\mathrm{d}\Psi_\text{v}}{\mathrm{d}t} = \frac{\partial \Psi_\text{v}}{\partial t} + \frac{\partial \Psi_\text{v}}{\partial \mathbf{E}} : \frac{\mathrm{d}\mathbf{E}}{\mathrm{d}t} = \frac{\partial \Psi_\text{v}}{\partial \mathbf{E}} : \dot{\mathbf{E}}, \tag{3.2.4}$$

equation (3.2.2) can be reformulated into

$$\mathbf{S} = \frac{\partial \Psi_\text{v}}{\partial \mathbf{E}}. \tag{3.2.5}$$

Other forms of this so-called constitutive equation can be found in Table 3.3.

Table 3.3: Calculating the different stress measures from a strain energy density function (SEF).

Stress Measure	Constitutive Equation		
Cauchy	$\boldsymbol{\sigma}$	$= J^{-1}\mathbf{F}\left(\frac{\partial \Psi_\text{v}}{\partial \mathbf{F}}\right)^T$	$= 2J^{-1}\mathbf{F}\frac{\partial \Psi_\text{v}}{\partial \mathbf{C}}\mathbf{F}^T$
1st Piola-Kirchhoff	$\mathbf{P}$	$= \frac{\partial \Psi_\text{v}}{\partial \mathbf{F}}$	$= 2\mathbf{F}\frac{\partial \Psi_\text{v}}{\partial \mathbf{C}}$
2nd Piola-Kirchhoff	$\mathbf{S}$	$= \frac{\partial \Psi_\text{v}}{\partial \mathbf{E}}$	$= 2\frac{\partial \Psi_\text{v}}{\partial \mathbf{C}}$

Since some materials, like lung parenchyma, show a compressible material behavior, i.e. their volume changes considerably during the deformation, it can be useful to split the deformation locally into a volumetric and an isochoric part. To do so, the deformation gradient $\mathbf{F}$ multiplicatively splits into a volume-changing and a volume-preserving part. This leads to

$$\mathbf{F} = \left(J^{\frac{1}{3}}\mathbf{1}\right)\bar{\mathbf{F}} = J^{\frac{1}{3}}\bar{\mathbf{F}}, \;\; \mathbf{C} = \left(J^{\frac{2}{3}}\mathbf{1}\right)\bar{\mathbf{C}} = J^{\frac{2}{3}}\bar{\mathbf{C}}, \tag{3.2.6}$$

with $J^{\frac{1}{3}}\mathbf{1}$ and $J^{\frac{2}{3}}\mathbf{1}$ being associated with the volume-changing deformation. The isochoric deformation gradient $\bar{\mathbf{F}}$ and the isochoric right Cauchy-Green strain tensor $\bar{\mathbf{C}}$, are associated with the volume-preserving deformation.

In order to solve the initial boundary value problem with the FEM, the linearized constitutive equation is needed. For this reason, the forth-order elasticity tensor is introduced as

$$\mathbb{C} := \frac{\partial \mathbf{S}}{\partial \mathbf{E}} = \frac{\partial^2 \Psi_{\mathrm{v}}}{\partial \mathbf{E} \partial \mathbf{E}} = 4 \frac{\partial^2 \Psi_{\mathrm{v}}}{\partial \mathbf{C} \partial \mathbf{C}}. \tag{3.2.7}$$

For more details the reader is referred to textbooks (Holzapfel, 2004; Schröder and Neff, 2003; Ogden, 1997).

There are two fiber families in the alveolar tissue, the CF and EF. However, as discussed above, see section 2.1.3.2, the fiber orientation within the alveolar tissue can be assumed to be isotropic. For this reason, the focus of this work is put on isotropic SEFs. In this case, the SEF is by definition invariant with respect to rotation, i.e.

$$\Psi_{\mathrm{v}}(\mathbf{C}) = \Psi_{\mathrm{v}}(\mathbf{RCR}), \tag{3.2.8}$$

for any rotation tensor $\mathbf{R}$.

This invariance towards rotation allows Ψ_{v} to be expressed in terms of the principle invariants of its argument $\mathbf{C}$. In the following section, coupled and decoupled SEFs will be presented, where the decoupled forms are split into an isochoric and a volumetric contribution.

3.2.1 Coupled Strain Energy Density Functions

The coupled SEFs considered in this work, are formulated as

$$\Psi_{\mathrm{v}}(\mathbf{C}) = \Psi_{\mathrm{v}}(I_1, I_2, I_3) \tag{3.2.9}$$

where I_1, I_2, and I_3 are the invariants of the right Cauchy–Green strain tensor $\mathbf{C}$, defined as

$$I_1 := \mathrm{tr}\mathbf{C},\ I_2 := \tfrac{1}{2}\left[(\mathrm{tr}\mathbf{C})^2 - \mathrm{tr}(\mathbf{C}^2)\right],\ I_3 := \det\mathbf{C}. \tag{3.2.10}$$

This leads to the calculation of the 2^{nd} Piola-Kirchhoff stress tensor

$$\mathbf{S} = 2\frac{\partial \Psi_{\mathrm{v}}(\mathbf{C})}{\partial \mathbf{C}} = \underbrace{2\left(\frac{\partial \Psi_{\mathrm{v}}}{\partial I_1} + I_1 \frac{\partial \Psi_{\mathrm{v}}}{\partial I_2}\right)}_{\gamma_1} \mathbf{1} + \underbrace{(-2)\frac{\partial \Psi_{\mathrm{v}}}{\partial I_2}}_{\gamma_2} \mathbf{C} + \underbrace{2I_3 \frac{\partial \Psi_{\mathrm{v}}}{\partial I_3}}_{\gamma_3} \mathbf{C}^{-1} \tag{3.2.11}$$

and the elasticity tensor

$$\begin{aligned}\mathbb{C} = 2\frac{\partial \mathbf{S}(\mathbf{C})}{\partial \mathbf{C}} &= 4\frac{\partial^2 \Psi_{\mathrm{v}}(I_1, I_2, I_3)}{\partial \mathbf{C} \partial \mathbf{C}} \\ &= \delta_1 \mathbf{1} \otimes \mathbf{1} + \delta_2 (\mathbf{1} \otimes \mathbf{C} + \mathbf{C} \otimes \mathbf{1}) + \delta_3 \left(\mathbf{1} \otimes \mathbf{C}^{-1} + \mathbf{C}^{-1} \otimes \mathbf{1}\right) \\ &\quad + \delta_4 \mathbf{C} \otimes \mathbf{C} + \delta_5 \left(\mathbf{C} \otimes \mathbf{C}^{-1} + \mathbf{C}^{-1} \otimes \mathbf{C}\right) \\ &\quad + \delta_6 \mathbf{C}^{-1} \otimes \mathbf{C}^{-1} + \delta_7 \mathbf{C}^{-1} \odot \mathbf{C}^{-1} + \delta_8 \frac{\mathbb{I} + \bar{\mathbb{I}}}{2}.\end{aligned} \tag{3.2.12}$$

In this context the symbols $\otimes$ and $\odot$ denote the tensor products given by

$$(\mathbf{G} \otimes \mathbf{G})_{JKLM} = \mathbf{G}_{JK} \mathbf{G}_{LM} \tag{3.2.13}$$

and

$$(\mathbf{G} \odot \mathbf{G})_{JKLM} = \frac{1}{2}(\mathbf{G}_{JL} \mathbf{G}_{KM} + \mathbf{G}_{JM} \mathbf{G}_{KL}). \tag{3.2.14}$$

The forth-order tensors $\mathbb{I}$ and $\bar{\mathbb{I}}$ are defined as $\mathbb{I} = \delta_{IM} \delta_{KL}$ and $\bar{\mathbb{I}} = \delta_{IM} \delta_{KL}$, respectively. The coefficients $\delta_1 - \delta_8$ are defined as

$$\delta_1 = 4\left(\frac{\partial^2\Psi_\mathrm{v}}{\partial I_1 \partial I_1} + 2I_1\frac{\partial^2\Psi_\mathrm{v}}{\partial I_1 \partial I_2} + \frac{\partial\Psi_\mathrm{v}}{\partial I_2} + I_1^2\frac{\partial^2\Psi_\mathrm{v}}{\partial I_2 \partial I_2}\right), \tag{3.2.15}$$

$$\delta_2 = -4\left(\frac{\partial^2\Psi_\mathrm{v}}{\partial I_1 \partial I_2} + I_1\frac{\partial^2\Psi_\mathrm{v}}{\partial I_2 \partial I_2}\right), \tag{3.2.16}$$

$$\delta_3 = 4\left(I_3\frac{\partial^2\Psi_\mathrm{v}}{\partial I_1 \partial I_3} + I_1 I_3\frac{\partial^2\Psi_\mathrm{v}}{\partial I_2 \partial I_3}\right), \tag{3.2.17}$$

$$\delta_4 = 4\frac{\partial^2\Psi_\mathrm{v}}{\partial I_2 \partial I_2}, \tag{3.2.18}$$

$$\delta_5 = -4I_3\frac{\partial^2\Psi_\mathrm{v}}{\partial I_2 \partial I_3}, \tag{3.2.19}$$

$$\delta_6 = 4\left(I_3\frac{\partial\Psi_\mathrm{v}}{\partial I_3} + I_3^2\frac{\partial^2\Psi_\mathrm{v}}{\partial I_3 \partial I_3}\right), \tag{3.2.20}$$

$$\delta_7 = -4I_3\frac{\partial\Psi_\mathrm{v}}{\partial I_3}, \text{ and} \tag{3.2.21}$$

$$\delta_8 = -4\frac{\partial\Psi_\mathrm{v}}{\partial I_2}. \tag{3.2.22}$$

3.2.2 Decoupled Strain Energy Density Functions

The decoupled SEFs, which are split up into a volumetric part Ψ_vol and an isochoric part Ψ_iso, are formulated as

$$\Psi_\mathrm{v}(\bar{I}_1, \bar{I}_2, J) = \Psi_\mathrm{iso}(\bar{I}_1, \bar{I}_2) + \Psi_\mathrm{vol}(J), \tag{3.2.23}$$

with

$$\bar{I}_1 = I_1 J^{-\frac{2}{3}} \quad \text{and} \quad \bar{I}_2 = I_2 J^{-\frac{4}{3}}, \tag{3.2.24}$$

being the first and the second modified invariant of $\bar{\mathbf{C}}$. The modified third invariant $\bar{I}_3$ is zero by definition since an isochoric deformation is volume preserving. The volumetric part of the SEF Ψ_vol depends solely on J, i.e. the change of volume. The decoupled stress tensor is defined as

$$\mathbf{S} = \mathbf{S}_\mathrm{iso} + \mathbf{S}_\mathrm{vol}. \tag{3.2.25}$$

The isochoric stress contribution $\mathbf{S}_\mathrm{iso}$ is given by

$$\mathbf{S}_{\text{iso}} = 2\frac{\partial \Psi_{\text{iso}}\left(\bar{\mathbf{C}}\right)}{\partial \mathbf{C}} = J^{-2/3}\bar{\mathbf{S}}\text{-}\frac{1}{3}\left[\bar{\mathbf{S}} : \bar{\mathbf{C}}\right]\bar{\mathbf{C}}^{-1} \tag{3.2.26}$$

with the fictitious second Piola-Kirchhoff stress tensor $\bar{\mathbf{S}}$ being defined by

$$\bar{\mathbf{S}} = 2\frac{\partial \Psi_{\text{iso}}\left(\bar{\mathbf{C}}\right)}{\partial \bar{\mathbf{C}}} = \underbrace{2\left(\frac{\partial \Psi_{\text{iso}}}{\partial \bar{I}_1} + \bar{I}_1\frac{\partial \Psi_{\text{iso}}}{\partial \bar{I}_2}\right)}_{\overline{\gamma}_{\text{iso, 1}}}\mathbf{1} \underbrace{-2\frac{\partial \Psi_{\text{iso}}}{\partial \bar{I}_2}}_{\overline{\gamma}_{\text{iso, 2}}}\mathbf{C}. \tag{3.2.27}$$

The volumetric stress stress contribution $\mathbf{S}_{\text{vol}}$ is given by

$$\mathbf{S}_{\text{vol}} = J\underbrace{\frac{\partial \Psi_{\text{vol}}}{\partial I_3}}_{\overline{\gamma}_{\text{vol, 1}}}\mathbf{C}^{-1}. \tag{3.2.28}$$

Based on equation (3.2.25), the elasticity tensor for a decoupled hyperelastic SEF is

$$\mathbb{C} = \mathbb{C}_{\text{iso}} + \mathbb{C}_{\text{vol}}. \tag{3.2.29}$$

The isochoric part $\mathbb{C}_{\text{iso}}$ depends on the isochoric stress contribution $\mathbf{S}_{\text{iso}}$ and thus is defined as

$$\mathbb{C}_{\text{iso}} = 2\frac{\partial \mathbf{S}_{\text{iso}}}{\partial \mathbf{C}} = \mathbb{P} : \bar{\mathbb{C}} : \mathbb{P}^T + \frac{2}{3}\left(\left(I_3^{-\frac{1}{3}}\overline{\mathbf{S}}\right) : \mathbf{C}\right)\tilde{\mathbb{P}} - \frac{2}{3}\left(\mathbf{C}^{-1} \otimes \mathbf{S}_{\text{iso}} + \mathbf{S}_{\text{iso}} \otimes \mathbf{C}^{-1}\right) \tag{3.2.30}$$

with $\mathbb{P} = \mathbb{I} - \frac{1}{3}\mathbf{C}^{-1} \otimes \mathbf{C}$ and $\tilde{\mathbb{P}} = \mathbf{C}^{-1} \odot \mathbf{C}^{-1} - \frac{1}{3}\mathbf{C}^{-1} \otimes \mathbf{C}^{-1}$ being a forth-order projection and a forth-order modified projection tensor, respectively, and $\bar{\mathbb{C}}$ denoting the fourth-order fictitious elasticity tensor

$$\begin{aligned} \bar{\mathbb{C}} &= 2J^{-\frac{4}{3}}\frac{\partial \bar{\mathbf{S}}}{\partial \bar{\mathbf{C}}} = 4J^{-\frac{4}{3}}\frac{\partial^2 \Psi_{\text{iso}}\left(\bar{I}_1, \bar{I}_2\right)}{\partial \bar{\mathbf{C}} \partial \bar{\mathbf{C}}} \\ &= J^{-\frac{4}{3}}\left(\overline{\delta}_{\text{iso, 1}}\mathbf{1} \otimes \mathbf{1} + \overline{\delta}_{\text{iso, 2}}\left(\mathbf{1} \otimes \bar{\mathbf{C}} + \bar{\mathbf{C}} \otimes \mathbf{1}\right) + \overline{\delta}_{\text{iso, 3}}\bar{\mathbf{C}} \otimes \bar{\mathbf{C}} + \overline{\delta}_{\text{iso, 4}}\frac{\mathbb{I} + \bar{\mathbb{I}}}{2}\right). \end{aligned} \tag{3.2.31}$$

The coefficients $\overline{\delta}_{\text{iso, 1}} - \overline{\delta}_{\text{iso, 4}}$ are defined as

$$\bar{\delta}_{\text{iso},\,1} = 4\left(\frac{\partial^2\Psi_{\text{iso}}}{\partial\bar{I}_1\partial\bar{I}_1} + 2\bar{I}_1\frac{\partial^2\Psi_{\text{iso}}}{\partial\bar{I}_1\partial\bar{I}_2} + \frac{\partial\Psi_{\text{iso}}}{\partial\bar{I}_2} + \bar{I}_1^2\frac{\partial^2\Psi_{\text{iso}}}{\partial\bar{I}_2\partial\bar{I}_2}\right), \tag{3.2.32}$$

$$\bar{\delta}_{\text{iso},\,2} = -4\left(\frac{\partial^2\Psi_{\text{iso}}}{\partial\bar{I}_1\partial\bar{I}_2} + \bar{I}_1\frac{\partial^2\Psi_{\text{iso}}}{\partial\bar{I}_2\partial\bar{I}_2}\right), \tag{3.2.33}$$

$$\bar{\delta}_{\text{iso},\,3} = 4\frac{\partial^2\Psi_{\text{iso}}}{\partial\bar{I}_2\partial\bar{I}_2}, \text{ and} \tag{3.2.34}$$

$$\bar{\delta}_{\text{iso},\,4} = -4\frac{\partial\Psi_{\text{iso}}}{\partial\bar{I}_2}. \tag{3.2.35}$$

The volumetric part of the elasticity tensor can be expressed as follows

$$\mathbb{C}_{\text{vol}} = 2\frac{\partial\mathbf{S}_{\text{vol}}}{\partial\mathbf{C}} = J\underbrace{\left(\frac{\partial\Psi_{\text{vol}}}{\partial J} + J\frac{\partial^2\Psi_{\text{vol}}}{\partial J\partial J}\right)}_{\bar{\delta}_{\text{vol},\,1}}\mathbf{C}^{-1}\otimes\mathbf{C}^{-1} - 2J\underbrace{\frac{\partial\Psi_{\text{vol}}}{\partial J}}_{\bar{\delta}_{\text{vol},\,2}}\mathbf{C}^{-1}\odot\mathbf{C}^{-1}. \tag{3.2.36}$$

The coefficients $\bar{\delta}_{\text{vol},\,1}$ and $\bar{\delta}_{\text{vol},\,2}$ are defined as

$$\bar{\delta}_{\text{vol},\,1} = \frac{\partial\Psi_{\text{vol}}}{\partial J} + J\frac{\partial^2\Psi_{\text{vol}}}{\partial J\partial J} \text{ and} \tag{3.2.37}$$

$$\bar{\delta}_{\text{vol},\,2} = \frac{\partial\Psi_{\text{vol}}}{\partial J}. \tag{3.2.38}$$

More detailed derivations can be found in Holzapfel (2004).

3.2.3 Requirements for Strain Energy Density Functions

The SEFs have to fulfill different requirements in order to produce thermodynamically stable and physically reasonable results. The following contains a brief overview over the most important aspects.

Strain Energy Density Functions Must be Positive For any state of deformation, the stored energy,

$$\Psi_{\text{v}}(\mathbf{C} \neq \mathbf{1}) > 0, \tag{3.2.39}$$

must be positive (Doll and Schweizerhof, 2000).

Stress Free Reference Configuration The requirement of a stress free reference configuration is physically reasonable, since in hyperelastic materials only deformations induce stresses. This condition can be written as

$$\mathbf{S}(\mathbf{C} = \mathbf{1}) = \mathbf{0}. \tag{3.2.40}$$

Limit Cases In the limit of a completely degenerated continuum to a single point, the strain energy needs to tend towards positive infinity and the volumetric stress to negative infinity. Accordingly, in the limit of an infinite stretch the continuum the strain energy as well as the volumetric stress have to tend towards positive infinity.

Principle of Material Frame Indifference - Objectivity The description of a physical quantity associated with the motion of a body is generally dependent on the observer. In contrast, the constitutive equation has to be independent of the particular observer, i.e. indifferent to a change of the reference system.

Hence, rigid body movements should not change the internal quantities. An arbitrary movement $\boldsymbol{\varphi}(\bullet)$ should lead to the same internal state as the same movement superimposed with a rigid body movement $\boldsymbol{\psi}(\bullet)$, leading to $\boldsymbol{\varphi}^{+}(\bullet) = \boldsymbol{\psi}(\boldsymbol{\varphi}(\bullet))$. Due to the superposition, the spatial point $\mathbf{X}$ gets mapped to $\mathbf{x}^{+} = \boldsymbol{\varphi}^{+}(\mathbf{X})$. In case of

$$\mathbf{x}^{+} = \mathbf{c}(t) + \mathbf{R}(t)\mathbf{x}, \tag{3.2.41}$$

where $\mathbf{c}(t)$ can be interpreted as a translation and $\mathbf{R}(t)$ as a rotation, the deformation gradient $\mathbf{F}^{+}$ can be obtained as

$$\mathbf{F}^{+} = \frac{\partial \mathbf{x}^{+}}{\partial \mathbf{x}} \frac{\partial \mathbf{x}}{\partial \mathbf{X}} = \mathbf{R}\mathbf{F}. \tag{3.2.42}$$

The principle of material frame indifference requires both observers to register the same amount of energy and the same state of stress of the deformed body, i.e.

$$\Psi_{\mathrm{v}}(\mathbf{R}\mathbf{F}) = \Psi_{\mathrm{v}}(\mathbf{F}), \; \mathbf{S}(\mathbf{R}\mathbf{F}) = \mathbf{R}\mathbf{S}(\mathbf{F}). \tag{3.2.43}$$

With the right Cauchy-Green tensor being *a priori* frame objective, i.e. $\mathbf{C}^{+} = \mathbf{F}^{+T}\mathbf{F}^{+} = \mathbf{R}^{T}\mathbf{F}^{T}\mathbf{R}\mathbf{F} = \mathbf{C}$, the SEF introduced above fulfills the below requirement as well

$$\Psi_{\mathrm{v}}(\mathbf{C}) = \Psi_{\mathrm{v}}\left(\mathbf{C}^{+}\right). \tag{3.2.44}$$

Existence of a Minimizer It has to be assured that the boundary value problem has at least one solution. It has been been shown that, polyconvexity is the most suitable restriction for the construction of physically reasonable SEFs, guaranteeing the existence of at least one minimum.

The polyconvexity requires

$$\Psi_{\mathrm{v}}(\mathbf{F}) = f(\mathbf{F}, J\mathbf{F}^{T}, J), \tag{3.2.45}$$

i.e. a function of the 19-dimensional space, to be convex. In a more descriptive way, this means that the transformations of line, area and volume elements, see equations (3.1.6), (3.1.8) and (3.1.7), need to be unique. An additional advantage is that polyconvex functions can be constructed by summing up polyconvex summands. More details on polyconvexity can be found in Ball (1977); Schröder (2004); Balzani (2006).

For more details on hyperelastic materials, the reader is referred to Ogden (1997); Holzapfel (2004).

4 State of the Art

This chapter provides an overview of previous work done in this field and what is still missing in order to achieve the aims of this study (see chapter 5). The first section gives a literature overview over experimental characterization of the lung. The second section gives a literature overview of lung modelling.

4.1 Experimental Characterization of the Lung Tissue

This section gives an literature overview of the experimental characterization of lung tissue, from the organ level down to the cell level. The focus of this section is on the experimental determination of elastic stress-strain curves, since this study is concerned with developing a hyperelastic material model for lung parenchyma. Experimental characterization methods, that are less targeted in this study are the p-V curves of the whole lung and cell culture experiments, they are described only superficially. A short definition of associated common constants of physiology and material science can be found in Appendix A.2 and A.3.

4.1.1 Pressure-Volume (p-V) Curves

In the literature, many approaches to characterize respiratory mechanics at the organ level with p-V curves are reported. In this study, only selected examples are presented to give a general impression of this type of experiments.

Hildebrandt (1969, 1970) investigated p-V curves of cat lungs. To do this, he placed the examined lungs in a fluid filled plethysmograph, in which the lung volume was cyclically changed, while the amount of gas within the lung was fixed. In total seven isolated cat lungs were used for this study. He found

1. stress relaxation and an almost symmetrical stress recovery to occur respectively, after volume increase and decrease;

2. dynamic elastance (Appendix A.3.2), to increase linearly with the logarithm of cyclic frequency (0.1 increase in elastance a 10-fold increase in frequency); and
3. hysteresis loop area, i.e. the area between the loading and unloading p-V curve, to vary with the square of the tidal volume but to be independent of the cyclic frequency.

Stamenovic and Yager (1988) studied the mechanical properties of the parenchymal tissue with and without surface tension, in air and saline filled rabbit lungs, respectively. In the first step, the lungs were inflated to transpulmonary pressure of 30 $\mathrm{mmH_2O}$. The associated volume was defined as the volume at TLC. The pressure was then successively reduced down to zero. At every step, small p-V loops were performed to determine the local bulk moduli. They found little difference in the shape of the curves describing the elastic behavior of air and saline filled lungs, suggesting that the mechanism of resisting deformation in both cases is similar. However, the air-filled lungs showed stiffer behavior, which they explained with the surface tension at the air-liquid interface.

Bates et al. (1989) determined the resistance (Appendix A.3.3) and elastance of the respiratory system using data obtained from healthy anesthetized dogs during mechanical ventilation at different frequencies and tidal volumes. They found resistance and elastance to decrease with increasing frequency. The variations of resistance and elastance with frequency are similar to the variations determined from regular ventilation data. There were, however, some systematic differences between the actual values of resistance and elastance obtained by the two methods, which may reflect certain non-linear characteristics. They also found a slight decrease for both resistance and elastance with increasing tidal volume at all frequencies.

Suki et al. (1989) measured the lung impedance in six healthy humans for frequencies between $0.01-0.1$ Hz. They superimposed small amplitude signals in order to force oscillations on spontaneous breathing. They did not find a difference between applying a force or a pressure. They found the compliance to decrease from 0.97 kPa/l via 0.27 kPa/l to 0.23 kPa/l at 0.01 Hz, 0.03 Hz, and 0.1 Hz, respectively. It is remarkable that at very small frequencies, the change in compliance is much larger than at higher frequencies, which are closer to actual breathing frequencies.

Summing up, the p-V curves are an adequate way to understand global lung mechanics, which is especially important for adjusting the ventilator towards the needs of a ventilated patient. However, the focus of this work is on a more local behavior of the lung parenchyma and even further down to the individual alveolar walls. For this reason p-V curves of the whole lung, including airways etc., are too coarse for this purpose.

4.1.2 Tensile Tests on Lung Parenchyma Specimens

To investigate the local material behavior of lung parenchyma, tests on isolated samples are required. In the literature, a wide range of experiments have been presented such as uni-, bi-, or triaxial tensile tests in a saline bath or in air. Consequently, this section gives an overview of the most important tensile tests on parenchymal tissue specimens.

4.1.2.1 Uniaxial Tensile Tests

Fukaya et al. (1968) performed uniaxial tensile tests on cat lung specimens with the dimensions $30 \times 30 \times 200\,\mu\mathrm{m}$, see Figure 4.1. Contrary to the title ”Mechanical properties of alveolar walls”, they investigated the material behavior of the parenchymal tissue and not of the individual alveolar wall. The tests were performed in a saline bath, in order to obtain the osmolarity of the cells, at room temperature. Their findings are briefly summarized in the following.

- The length-tension relationship did not change within the first 36 h after dissection of the lungs.
- A strong hysteresis occurred in the length-tension relationship.
    - The hysteresis depends on final force and length-tension history, see Figure 4.2(A) (Remark: The hysteresis measured is not due to the air-liquid interface, because the tests were performed in a saline bath).
    - However, the hysteresis is not dependent on cyclic frequencies between 6 cycles/min and 0.2 cycles/min. The independence of the cyclic frequency has been previously reported by Hildebrandt (1966).
- The length increase of the specimens is limited to an extension of $100 - 130\,\%$ over the initial length; stretch beyond this length resulted in tissue damage.
- Stress relaxation and recovery, with the fast component of stress relaxation, is complete within 60 s after the initial deformation.
- The hysteresis, in a quasi-static experiment, is reduced but does not disappear, see Figure 4.2(B). This shows that the hysteresis is not solely dependent on the fast component of stress relaxation.
- A 5 min resting period is necessary to reset the tissue back to its initial state prior to testing.

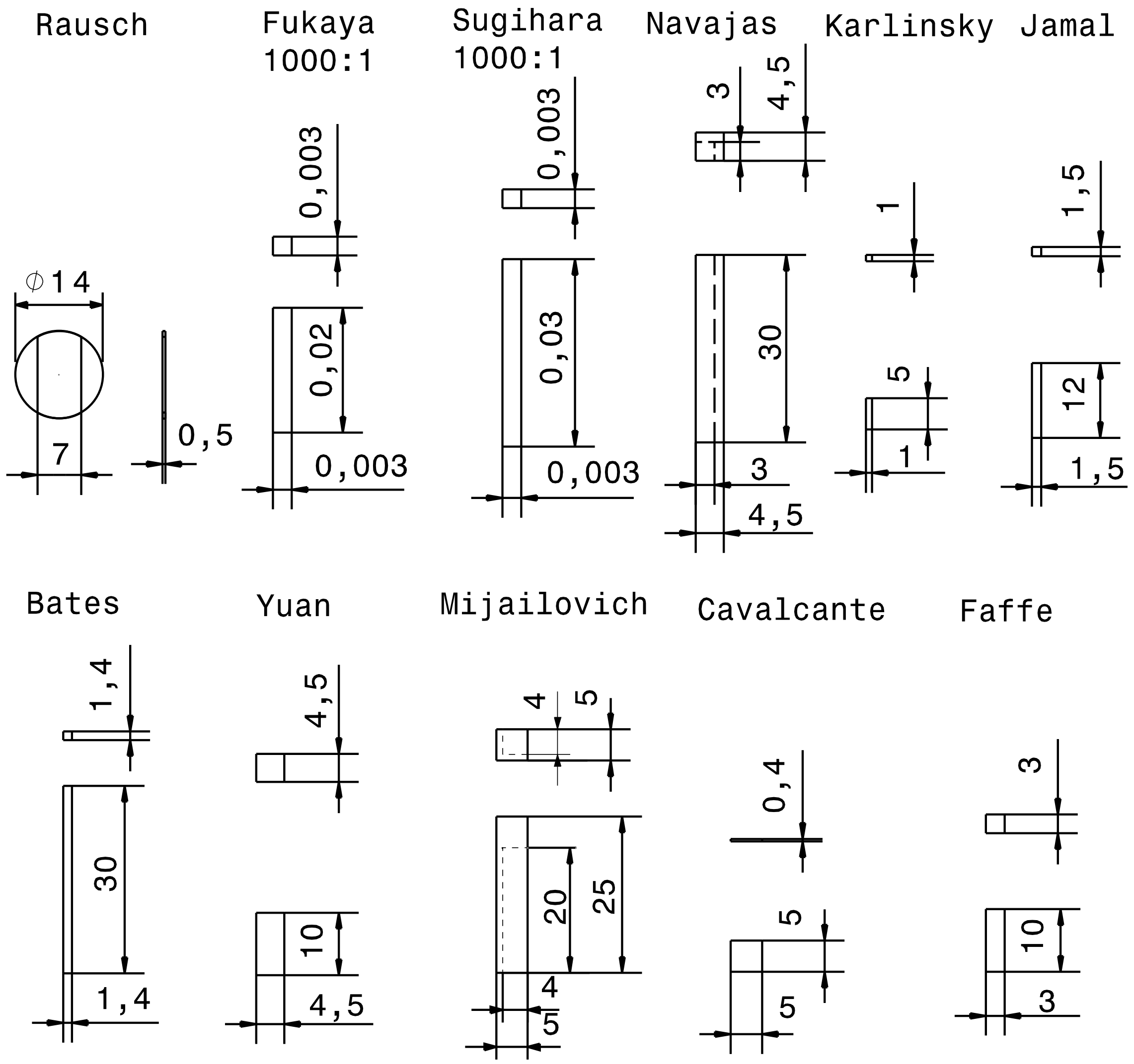

Figure 4.1: Comparison of specimens utilized in uniaxial tensile tests. First row from left to right: Rausch et al. (2011b), Fukaya et al. (1968), Sugihara et al. (1971), Navajas et al. (1995), Karlinsky et al. (1985), and Jamal et al. (2001). Second row from left to right: Bates et al. (1994), Yuan et al. (1997), Mijailovich et al. (1994), Cavalcante et al. (2005), and Faffe et al. (2001). The dashed lines indicate that the specimen dimensions were not clearly defined in the corresponding paper. The units are given in mm.

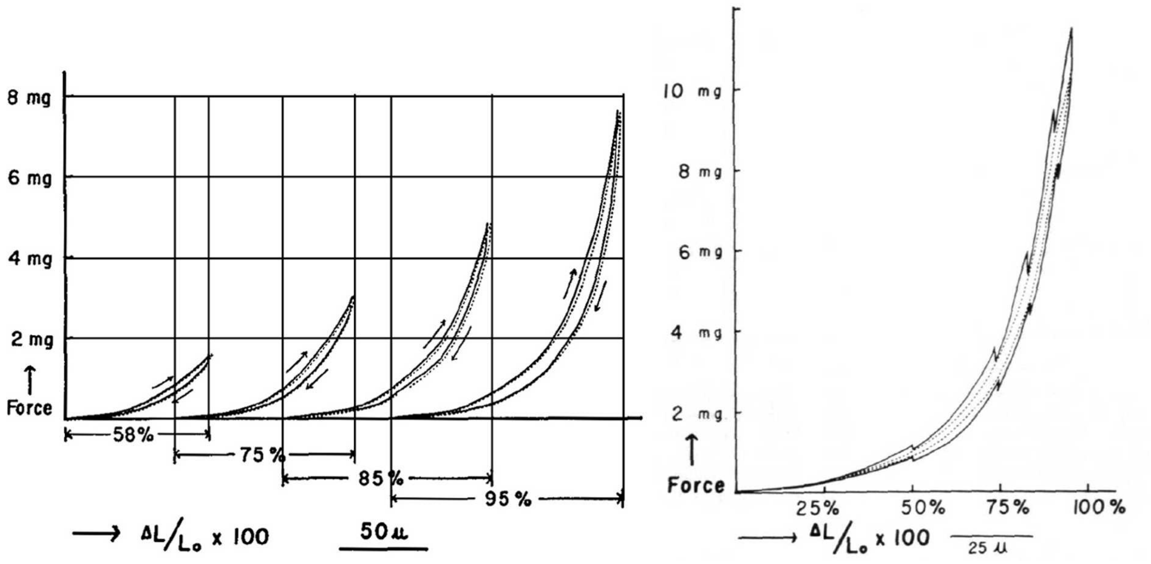

(A) (B)

Figure 4.2: (A) Length-tension characteristics of cat lungs for different maximal forces. (B) Determination of the time dependent portion of the hysteresis loop, by letting stress relaxation and stress recovery occur. Figures were taken from Fukaya et al. (1968)

Sugihara et al. (1971)performed uniaxial tension tests on human lung parenchyma. The focus of their study was to characterize the change of material properties with age, sex and expiratory flow. In total, they tested 170 specimens from 25 individuals (14 male, 11 female), between 18 and 88 years old. They used the same testing apparatus as Fukaya et al. (1968). Their findings are briefly summarized in the following.

- Due to the history dependence of the length-tension relationship, preconditioning was necessary. To do so, they stretched the tissue with $3\,\mathrm{g}$ force ($\widehat{=}32.7\cdot 10^6\,\mathrm{Pa}$) to provide a small extension. After 10 preconditioning cycles the length-tension curves did not change anymore.
- Forces of $15\,\mathrm{g}\left(\widehat{=}163.5\cdot 10^6\,\mathrm{Pa}\right)$ caused irreversible damage to the tissue.
- There is no difference between specimens gained from autopsy or surgery.
- The maximum length increase, for a given force, of the specimens was between $133\,\%$ and $260\,\%$, with a mean of $175\,\%$.
- The maximum extensibility decreased with age.

Sugihara et al. (1971) propose that the maximum extensibility, for an applied force, is an important tissue property. They assumed the limit for the tissue elongation could arise from two possible mechanisms

1. the tissue is not as extensible anymore, i.e. the tissue component responsible for the stop of the extension has shortened or
2. the initial length of the tissue has increased, whereas the maximal extension does not change.

Due to the fact that the diameter and the volume of the alveoli increase with age, the second option seems more reasonable. A shortcoming of this study is that they assumed the tissue to be incompressible, which is not the case for lung parenchyma.

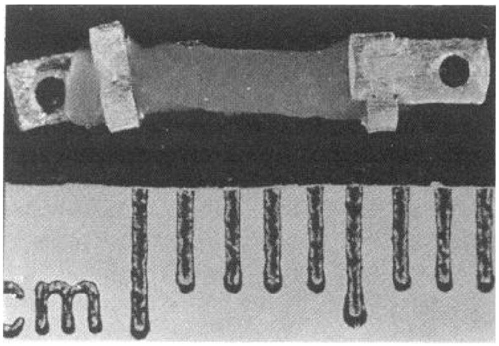

Figure 4.3: Photograph of lung strip, with the dimension $1 \times 1 \times 5\,\mathrm{mm}$, used for uniaxial tensile tests by Karlinsky et al. (1985).

Karlinsky et al. (1985) studied the thermoelastic properties of uniaxially deformed hamster lung strips. The idea being that, since macromolecules in the tissue, i.e. CF and EF, have different thermoelastic moduli, variation in temperature would affect their respective contributions to the tissue elastic properties. To investigate this question, they performed the experiments on hamster lung strips, see Figure 4.3, with the dimension $1 \times 1 \times 5\,\mathrm{mm}$, see Figure 4.1. They assumed that lung tissue is a homogeneous, isotropic and nearly incompressible material. They found that

- freezing or refrigerating increases the stiffness of the lung strips,
- over the temperature range $23 - 42\,^{\circ}\mathrm{C}$, the material behavior does not change, and
- above $50\,^{\circ}\mathrm{C}$, not only the CF melt and denatured but also the mechanical properties of the EF change with respect to lower temperatures.

The results supported their hypothesis that high non-physiological temperatures alter the distribution of water in lung connective tissue, thus, influencing the micro-mechanical behavior of the fibers alter the macro-mechanical behavior of the lung strips. Their findings demonstrated that performing experiments at room temperature instead of body temperature does not affect the mechanical behavior, while freezing changes the material properties of the tissue.

Bates et al. (1994) investigated time dependent effects in lung tissue. They cut their specimens, with the dimension of $30\times\sim1.4\times\sim1.4\,\mathrm{mm}$, from saline filled dog lungs. Their main finding was that some aspects of organ behavior arise from the connectivity between the organ components, i.e. it is not enough to only understand the behavior of the individual components. There is not much information about the elongation of their specimens after preconditioning, the lateral contraction nor how many samples were tested.

Mijailovich et al. (1994) investigated whether the material behavior of rabbit lung parenchyma, especially the viscoelastic properties, could be simplified by a previously described model of two fibers in contact (Mijailovich et al., 1993). In their model, the load was transferred from one fiber to the next by friction acting at slipping interfaces. To verify the model assumptions, they performed uniaxial tensile tests on rabbit lung strips, compared their analytical results with experimentally determined data and found

- E to increase linearly with the logarithm of frequency,
- E to decrease with strain amplitude,
- the hysteresis to decrease moderately with increasing frequency, and
- a disparate mechanical response after the tissue was exposed to a hyper tonic solution.

All the above effects are consistent with the predicted effects of their model, for example if the tissue is swelling in a hyper tonic solution, the contact between the two fibers changes. All experiments were performed in a temperature controlled tissue bath, i.e. there are no surface tension effects.

The specimens were cut, in the degassed state, to a length-width-height ratio of 5:1:1. With the length of the specimen being between $20-25\,\mathrm{mm}$, the cross-sectional area A_{cut} was between $0.16-0.25\,\mathrm{cm}^2$, see Figure 4.1 dashed line. After the cutting process, the cross-sectional area A was recalculated, based on the tissue density $\rho = 1.06\,\mathrm{g/cm}^3$, the mass M of the tissue, and the initial length L, i.e. $A = \frac{M}{\rho_0 L} = 0.19 \pm 0.02\,\mathrm{cm}^2$. Unfortunately, there is no information about how the cutting and weighing of the specimen were performed and about, how L and ρ_0 were determined. Based on the value of ρ_0, it can be assumed to be the density of the alveolar walls rather than the parenchymal tissue, i.e. the calculated stresses referrers solely to the tissue fraction of the strip and not to the homogenized lung parenchyma. However, comparing the force-strain curve with other results reported in literature, the tissue appears to be much softer, see Figure 4.4. This might be caused by strains above 100 %, which can damage the tissue (Fukaya et al., 1968).

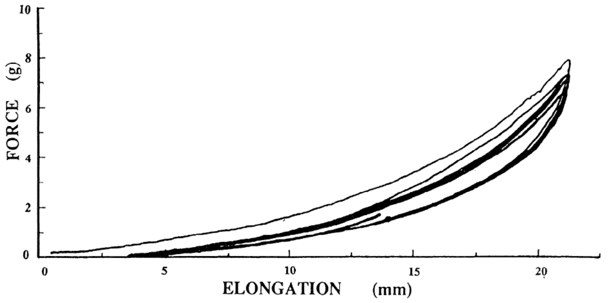

Figure 4.4: Force-elongation loops of rabbit lung parenchymal strip. Figure taken from Mijailovich et al. (1994).

Navajas et al. (1995) investigated the dynamic viscoelasticity of dog lung tissue, i.e. the time and frequency response of isolated parenchymal strips. They studied five strips of five different dogs. The lungs were degassed, filled with a Krebs-Ringer solution, and specimen of the dimension $\sim 30 \times 3 \times 3\,\mathrm{mm}$ were cut, yielding a cross-sectional area of $A_{\mathrm{cut}}=9\,\mathrm{mm}^2$, see Figure 4.1. However, due to the softness of the tissue, these dimensions were not very accurate. For this reason, they calculated the cross-sectional area similar to Mijailovich et al. (1994). They get a mean ± sd of the cross-sectional area of A_{cut} of $21.66 \pm 1.37\,\mathrm{mm}^2$, with sd being a standard derivation, see Figure 4.1 dashed line. Similar to Mijailovich et al. (1994), they also did not give any information on how the weight or initial length of the tissue was determined. Furthermore, in comparison to Mijailovich et al. (1994), where the ratio between the cut and the calculated cross-sectional area was between 0.84 and 1.31, the ratio of Navajas et al. (1995) was only 0.42.

Navajas et al. (1995) found the quasi-static elastic behavior of lung parenchyma to be strongly non-linear and well described by an exponential curve, see Figure 4.5. Their results concerning viscoelasticity are not discussed in detail here, because viscoelasticity is not part of this work. Similar to Mijailovich et al. (1994), they also strained the tissue over 100 %, which might, according to Fukaya et al. (1968), damage the tissue. Furthermore, neither reported the elongation of the tissue strip after the preconditioning. The viscoelastic effects are not further discussed since they are not part of the presented work.

Maksym et al. (1993) and Maksym and Bates (1997) performed uniaxial tensile tests in order to calibrate their tissue model of section 4.2.1. They took specimens from five different degassed dog lungs, with the dimensions $1.5 \times 1.5 \times 28\,\mathrm{mm}$. The experiments were performed in a tissue bath, i.e. without surface tension, after preconditioning. The determined stress-strain curves can be found in Figure 4.6. There is no information about the cutting technique or the elongation of the tissue after a preconditioning phase.

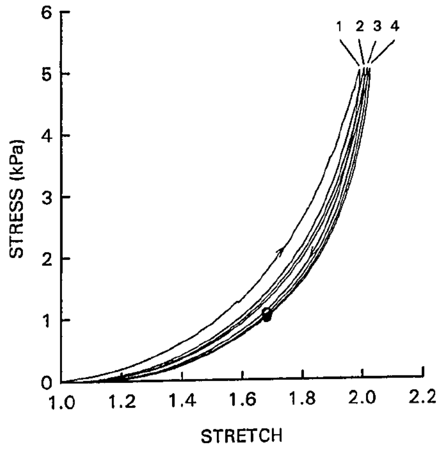

Figure 4.5: Stress-stretch curve for dog lung parenchyma during preconditioning. The strip was cyclically stretched with a constant rate of 0.02 1/s from its resting length up to a maximum stress of $5 \cdot 10^3$ Pa. Subsequently, the cycling was stopped at a stress ratio of 1.683 where the tissue had a nominal stress of 1 kPa and the deformation remained constant for 6 min to stabilize the tissue. Figure taken from Navajas et al. (1995).

Yuan et al. (1997) investigated the contributions of cellular elements and the fiber network to the macroscopic mechanical properties of parenchymal tissue. They measured the dynamic material properties in viable and nonviable tissue. They also assessed the influence of metabolically active cells on tissue mechanics under the induction of MCh, a parasympathomimetic drug stimulating smooth muscle activity. In total, they investigated eight strips from eight guinea pigs with dimensions of $4.5 \times 4.5 \times 10$ mm, see Figure 4.1.

The tests were performed in an organ bath and the specimens were glued to small metal clips. They found the tissue mechanics at the macroscopic level to be mainly influenced by the connective tissue fiber network, whereas interstitial cells played only a minor roll.

Three years later, another paper was published by Yuan et al. (2000), where the influence of CF and EF was investigated in more detail. To do so, they treated similar tissue strips with the enzymes collagenase and elastase. These two enzymes destroy the associated fiber family as will be discussed in section 4.1.2.4. Yuan et al. (2000) found that

- the fraction of intact fibers decreases after enzyme treatment and
- the decrease in intact fibers leads to a decrease in stiffness, see Figure 4.7.

This led them to the assumption that the two fiber families dominate the mechanical behavior of lung parenchyma. Results concerning viscoelastic material properties are not further discussed in this study.

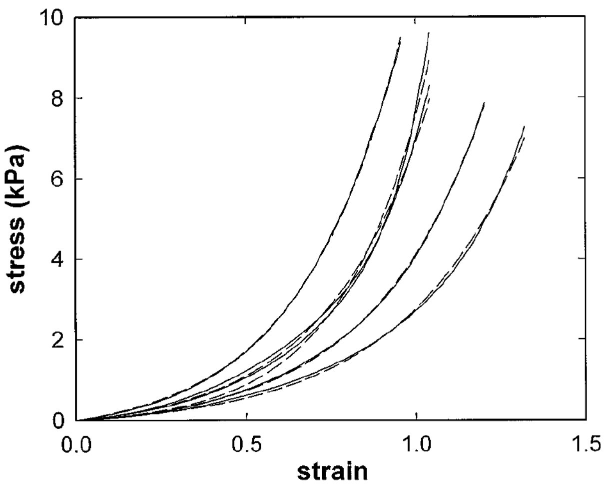

Figure 4.6: Five individual stress-strain curves of lung parenchyma strips, obtained from five different dogs. The curves were recorded a frequency of $0.005L$ 1/s. The solid lines indicate the experimentally determined curve, while the dashed line is a curve fit. Figure taken from Maksym and Bates (1997).

Kononov et al. (2001) investigated collagen failure and the changes in mechanical properties in the development of elastase-induced emphysema. They measured the stress-strain properties of a rat lung tissue section while simultaneously visualizing the collagen-elastin network. They filled the lungs with 55 °C warm agarose and cut specimens of $4 \times 4 \times 10$ mm. Preliminary studies showed that the agarose did not influence the mechanical properties. They found that, in the elastase treated tissue

- significant remodeling leads to thickened CF and EF, which undergo larger distortion than in normal tissue;
- the threshold for mechanical failure of collagen is reduced.

Their results indicate that mechanical forces during breathing are capable of causing failure in the remodelled tissue, leading to a progression of the emphysema.

Jamal et al. (2001) examined whether GAGs affect the tissue viscoelasticity. Rat parenchyma strips were exposed to a specific degenerative enzyme and it was evaluated if the material behavior changes. They performed uniaxial tensile tests in an organ bath on parenchyma strips with the dimensions of $1.5 \times 1.5 \times 12$ mm, see Figure 4.1. They calculated the initial cross-sectional area of their specimen similar to the method of Mijailovich et al. (1994). The strips were preconditioned but there was no adjustment of the resting length prior to testing. The maximal strain amplitude was 5 %. They found the degeneration to have an impact on the viscoelastic material behavior but compared to the influence of elastance (dynamic and static) it was found to be neglectible. The quasi-

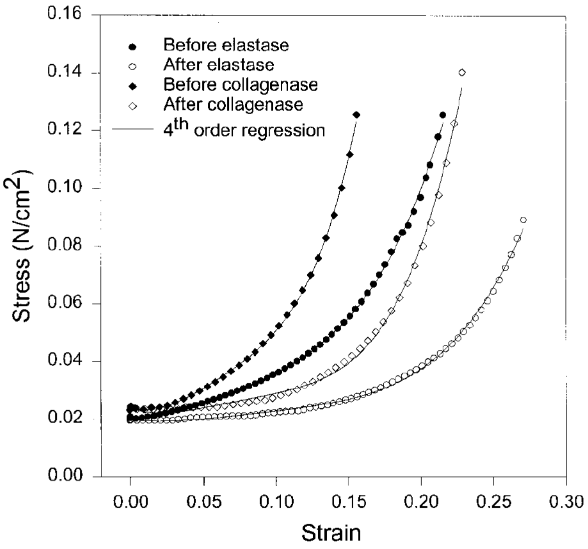

Figure 4.7: Quasi-static stress-strain curves of guinea pig tissue strips before and after enzymatic digestion. One of the strips was treated with collagenase and the other one with elastase. Figure taken from Yuan et al. (2000).

static-stress strain curves are shown in Figure 4.8. Unfortunately, they did not report the change in cross-sectional area in comparison with the dimensions of the cut area or how they determined the wet weight.

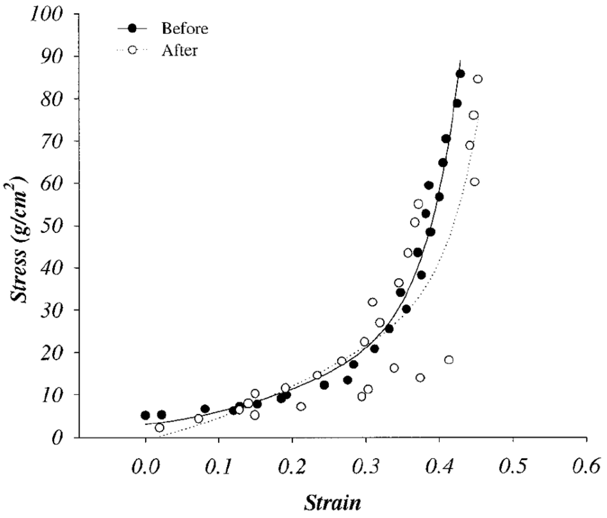

Figure 4.8: Quasi-static stress-strain curve. Figure taken from Jamal et al. (2001)

Cavalcante et al. (2005) studied the influence of proteoglycans and found that the mechanical behavior of the parenchymal tissue is not only dependent on the CF, EF, and their interaction but also on their interaction with the proteoglycans. Contrary to CF and EF, the proteoglycans can resist compression and shear. They assume that the elasticity of the lung tissue primarily arises from:

1. the topology of the collagen-elastin network, and
2. the mechanical interaction of proteoglycans and fibers.

To investigate these hypothesis, they measured a quasi-static, uniaxial stress-strain curve in a hypotonic, normal and hypertonic solution. They degassed rat lungs and filled them with 55 °C warm agarose and cut tissue strips of $5 \times 5 \times \sim 0.4\,\mathrm{mm}$, see Figure 4.1. The agarose was removed and one out of three samples per lung was used for determining a stress-strain curve, whereas the other two were used for imaging. The samples were glued to the force transducer and the experiments were performed within a saline solution. They stretched the samples up to an extension of 30 %. They found rat tissue to be sensitive to the osmolarity, however, this sensitivity decreased with digestion of the proteoglycans. They determine rather linear stress-strain curves for strains of up to 30 %. Since the measured stresses are much lower than others reported in literature, their results are excluded from further comparisons.

Faffe et al. (2001, 2006) investigated the influence of the extracellular matrix composition on the viscoelastic material properties of mouse parenchyma. In their first study they examined 23 male mice. After the lungs were rinsed in a modified Krebs-Henseleit solution, they cut specimens with the dimensions of $3 \times 3 \times 10\,\mathrm{mm}$, see Figure 4.1. The initial area A was determined from the volume and the initial length L_0. However, how these quantities were measured was not specified. They remeasured the resting length L of the specimen after the preconditioning protocol was completed. After the experiments, a morphological study was performed on the tested specimens. They found the elastance to have a positive dependence on frequency. In the second paper, they used slightly smaller mice specimens with the dimensions $2 \times 2 \times 10\,\mathrm{mm}$, see Figure 4.1. They also found a positive frequency dependence as well as a correlation between the elastance and the content of both the CF and EF. However, they stated that not only the absolute amount of fibers but also their organization is responsible for the tissue stiffness.

4.1.2.2 Biaxial Tensile Tests

Vawter et al. (1978) investigated the difference between uniaxial and biaxial loading. They cut pieces of frozen, saline filled dog lungs to $50 \times 50 \times 5\,\mathrm{mm}$ specimens. These specimens were stretched in-plane. The in-plane deformations and the thickness change were measured with an optical electromechanical system. All tests were performed in a tissue bath. Their main findings are listed bellow.

- For small strains, the tissue is stiffer for biaxial than for uniaxial tension.
- For larger strains, beyond a cross-over point, this behavior reverted and the tissue becomes stiffer for uniaxial loading.

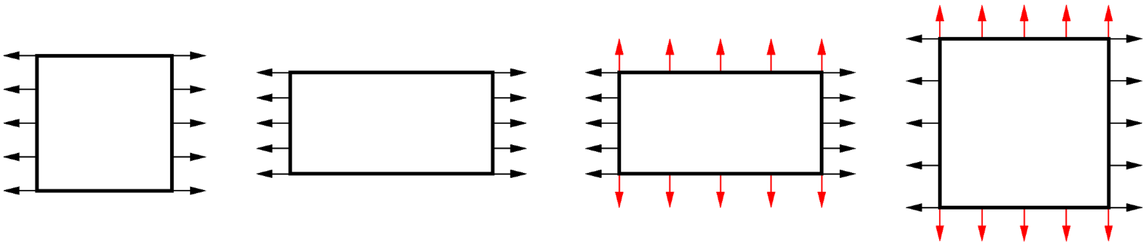

Figure 4.9: Schematic drawing of the biaxial tensile tests performed by Vawter et al. (1978). The specimens are loaded with a constant stress in the one direction (black arrows), while the stress in the perpendicular direction is varied cyclically (red arrows).

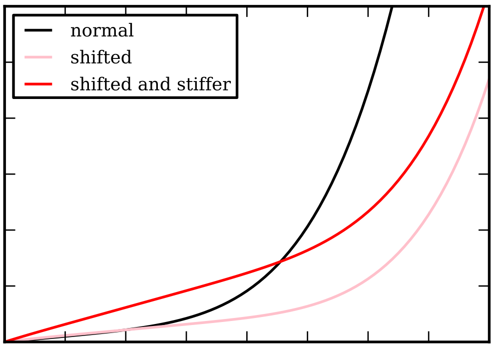

Figure 4.10: Comparison of stress-strain curves. The black curve is generally generated, showing a similar behavior than the experimental results by Vawter et al. (1978). The pink curve shows the same behavior but is shifted to the right. This happens if two different initial lengths L are utilized. The red curve has the same shift as the pink curve but with stiffer behavior, which arises from the different loading state. The black and the red curves show similar cross-over behavior than that which Vawter et al. (1978) found in their experiments.

These specimens were stretched in-plane. The in-plane deformations and the thickness change were measured with an optical electromechanical system. All tests were performed in a tissue bath.

Having a closer look at their testing protocol, this finding becomes less surprising. For their biaxial testing, they pre-stressed the specimen in one direction and cyclically loaded in the perpendicular direction, see Figure 4.9. They compared the extension ratio $\lambda = \frac{l}{L}$ in the direction of the varied load. However, when the pre-stretched state, i.e. the second drawing in Figure 4.9, is taken for determining the initial length L, the stress-strain curve shifts to the right, see Figure 4.10. Furthermore, not only the loading but also the strain state is three-dimensional, i.e. a strain measure including only one direction is not sufficient. For this reason, the material behavior appears stiffer for biaxial loading than for uniaxial loading. An additional problem could be the freezing of the tissue, since according to (Karlinsky et al., 1985), this changes the material properties of the tissue.

This work was followed up by Zeng et al. (1987), who tested postmortem human lungs. They also performed biaxial tests, where uniaxial modes were included as a special case. The lungs were filled with saline, frozen, and cut into specimens with the dimensions of $30 \times 30 \times 4$ mm. The load was applied with 8 silk threads, which could spread out and allowed large deformations. The forces were measured with force transducers and the deformation was tracked optically in a target area at the center of the specimen, see Vawter et al. (1978). A specified load was applied first in one direction and then in perpendicular direction The specimen was stretched sinusoidally between fixed limits at a given frequency of 0.04 Hz. They found

- a strongly non-linear stress-strain relationship with hysteresis,
- the strain-rate effect to be small between three tested frequencies, see Figure 4.11 (left),
- the human lung to be stiffer than dog lungs, by comparing their data to those obtained by Vawter et al. (1978), and
- regional differences in the stress-strain curves, by comparing specimens obtained from the five different lobes, see Figure 4.11 (right).

Similar to Vawter et al. (1978), there was the problem of the tissue being frozen before testing.

Yager et al. (1992) stretched liquid-filled human and dog lungs biaxially. They investigated the effects of macroscopic biaxial stretch on local deformation. The specimens were filled with saline, frozen, and cut into specimens with the dimensions of $50 \times 50 \times 5$ mm. The dimensions are quite similar to the ones of Vawter et al. (1978). In total, they investigated 182 duct rings, 151 from humans and 31 from dog specimens. They measured the relative deformation of ducts versus alveoli in a plane section of the lung under biaxial loading conditions. The deformation of the ducts was measured and compared to the macroscopic deformation. To the author's knowledge this is the only paper measuring ductal deforma-

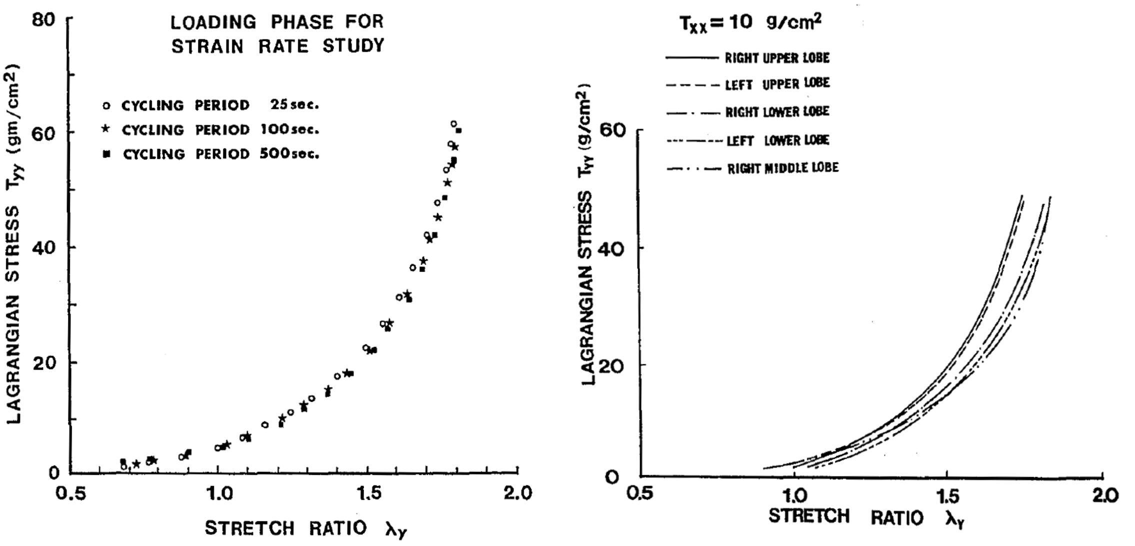

Figure 4.11: Left, stress-strain curves of human lung specimens under biaxial loading. The load in one direction is fixed, whereas the load in the perpendicular direction (y) is applied sinusoidally. Although, the loading changed frequency, the tissue shows almost no frequency dependence. Right, comparison of the stress-strain curves for the different lobes. Both Figures were taken from Zeng et al. (1987).

tion. They discussed the point that biaxial testing without the influence of surface tension, does not represent the actual loading state in the lung. Nevertheless, they measured a revised notion of the interaction between the ducts and the surrounding alveoli, as well as their mechanical role in the saline filled lung. They found

- all septal walls to be stretched, despite the absence of surface-tension and
- the local deformation to be significantly larger than the global deformation.

They concluded that the fiber reinforcement in the alveolar mouths could compensate for the missing structural stability due to the absent alveolar wall, which would lead to a uniform deformation state all over the lung. Unfortunately, no stress-strain curves were shown in this work but they can be expected to be similar to the ones presented earlier by Vawter et al. (1978) and Zeng et al. (1987).

Debes and Fung (1992) investigated the influence of temperature on the mechanical properties of dog lung parenchyma. Preparing the specimens, the lungs were degassed, frozen, and cut into specimens to the dimension of $50 \times 50 \times 5$ mm. After the specimen preparation the exact specimen dimensions were measured to be $42 \pm 0.4 \times 42 \pm 0.4 \times 3.6 \pm 0.8$ mm. Repeated freezing and thawing caused a reduction of $20-50\,\%$ of the compliance of p-V curves. Debes and Fung (1992) used the same testing device as Yager et al. (1992). They were especially interested in the mechanics of CF and EF, for this reason they eliminated the surface tension prior to testing. They performed biaxial tensile tests, where they varied the strains between $0-30\,\%$ and the temperature between $10-40\,^\circ\mathrm{C}$. They found

- the stress-strain relationship to be linear,
- the mechanical properties of the lung changed slowly and linearly with temperature, and
- the elastic modulus increased by 1.6 % during cooling from body to room temperature.

These results showed that testing at room temperature does not significantly influence the outcome of the experiments.

Gao et al. (2006) performed their experiments on postmortem human specimens. In total, they had 17 specimens of seven cadavers. The specimens were filled with saline, frozen, and cut to specimens with the dimensions of 50 × 50 × 4 mm. The dimensions are quite similar to the ones of Vawter et al. (1978) and Yager et al. (1992). The strain was measured with a rectangular mark of four 300-μm-diameter steel wires at the center of the specimen, see Figure 4.12. All experiments were performed in a saline bath.

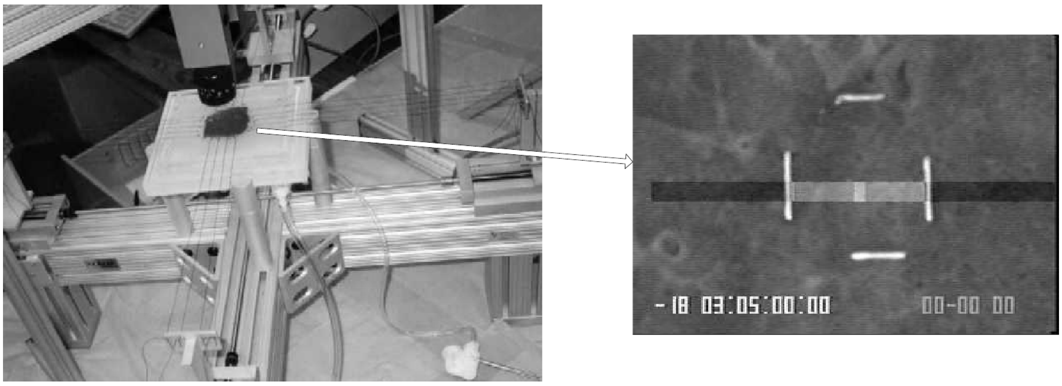

Figure 4.12: The left picture shows the set up of the biaxial testing of Gao et al. (2006). The right picture shows a top view of the central region of the tested specimen utilized to calculate local strains. Figure taken from Gao et al. (2006).

They performed two types of experiments, one with equi-biaxial loading and one similar to the experiments of Vawter et al. (1978), with one direction being constantly loaded and the perpendicular direction being cyclically loaded. One concern about the experimental results is the long post-mortem time of the cadavers, which is 3.0 ± 1.1 month. The tissue might have been degenerated and changed the mechanical properties during this time.

4.1.2.3 Triaxial Tensile Tests

Hoppin et al. (1975) performed triaxial tensile tests on dog lung specimens. The tissue was frozen and cut in cubes of $10 \times 10 \times 10\,\mathrm{mm}$. In total, they tested three specimens. The force was induced by placing 16 small fishhooks evenly into each of the six surfaces, see Figure 4.13.

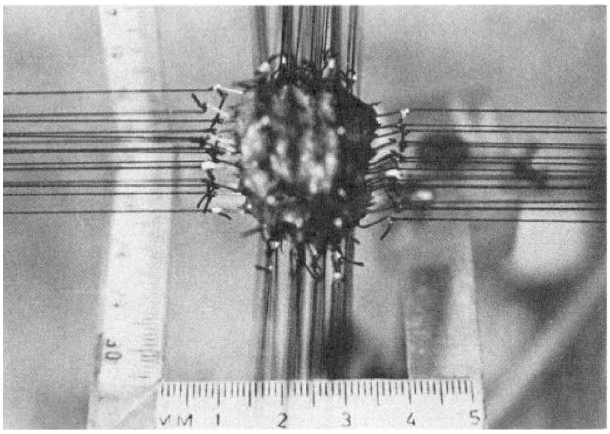

Figure 4.13: Photograph of a specimen under triaxial loading. Figure taken from Hoppin et al. (1975).

They found:

- a greater hysteresis in air-filled than in saline filled specimens,
- moderate differences in extensibility during equi-triaxial loading, i.e. loading the specimen with the same force in all three directions but they could not determine a specific preferred direction, and
- a greater tissue compliance and less hysteresis during asymmetric loading, in comparison with symmetric loading.

The experiments showed a slightly anisotropic behavior. However, the direction of the anisotropy was not consistent. In the discussion, they stated two possible explanations for this anisotropy. First, it is small and real but not systematic, and second, the anisotropy could be due to variations in the preparation of the tissue specimens, placing of the hooks, mechanical linkage, or other effects. Reasons for isotropy could be the homogeneous distribution of alveoli under the microscope and the observation that the excised lung deflates symmetrically. This lead them to the assumption that at a macro level, parenchyma may well be isotropic to the extent that the respiratory units are randomly orientated. Problems are the inaccuracy in cutting, placing of the fishhooks, the small number of specimens, and the freezing of the tissue.

Later, the same protocol was used by Tai and Lee (1981) for additional investigation concerning anisotropy, age dependence, and homogeneity of dog lung parenchyma. For the anisotropy they found that:

- it is more noticeable in air than in saline filled specimens and
- it decreases with age.

However, the only significant anisotropy was found in young dogs tested in air and they stated that this anisotropy is not significant enough to justify additional measurements. For age dependence, they found the maximal extension ratio to increase with age. These results are in agreement with the study of Sugihara and Martin (1975) on human lungs. For homogeneity they tested different specimens of different positions within the lungs but, they did not find significant changes between the different locations. Additionally, they investigated the influence of gravity by changing the orientation of the specimen in the machine but they did not find a significant influence.

4.1.2.4 Enzyme Treatment of Lung Parenchymal Tissue

Using an electron microscopy, Karlinsky et al. (1976) observed disruption of CF and EF after both were, respectively treated with either collagenase or elastase. They also found collagenase not to be active against EF and the other way round. Based on their results, the degeneration of the two fiber families is appropriate to study their mechanical contribution.

As mentioned above, Yuan et al. (2000) performed uniaxial tensile tests on guinea pig lung parenchyma. They investigated the origin of tissue elastic and hyperelastic properties. To achieve this, they investigated the linear and non-linear mechanical contributions of the main load-bearing constituents of the lung parenchyma, i.e. CF, EF, and their fiber network. To determine the contribution of the individual constituents they treated the parenchymal tissue with collagenase and elastase, which respectively destroyed the CF and EF. For the enzymatic treatment they used collagenase (1 mg Sigma Chemical) or pancreatic elastase (5 µg Sigma Chemical). During the digestion, the specimens were placed in a chamber filled with phosphate buffered saline (37 °C, pH 7.4) to which the respective enzyme solution was added. The incubation times were 30 min and 60 min for the collagenase and elastase, respectively. One of their main findings was that both CF and EF have a strong influence on the slope of the entire stress-strain curve, see Figure 4.7. This is in contradiction with the observations of Karlinsky et al. (1976), who found the compliance of elastase treated lungs is only reduced at low to medium lung volumes, whereas the compliance of collagenase treated lungs decreased at high lung volumes. Additionally, the stiffness of the intact tissue strip is lower than of the individual fiber families, which is most likely a network effect.

Furthermore, the above discussed studies by Kononov et al. (2001); Jamal et al. (2001); Cavalcante et al. (2005); Faffe et al. (2001, 2006) also investigate enzyme treated specimens, see section 4.1.2.1.

4.1.3 Determining Deformations of the Alveolar Wall

Brewer et al. (2003) investigated the influence of *in vivo* elastance treatment on microscopic and macroscopic deformation. They performed uniaxial tensile tests on immunofluorescently labeled tissue strips. Utilizing a fluorescent microscope, they were able to follow the microscopic length change and angular orientation, see Figure 4.14. Additionally, the macroscopic strain was measured and a network simulation, based on the network model introduced by Mishima et al. (1999) (section 4.2.1), was performed.

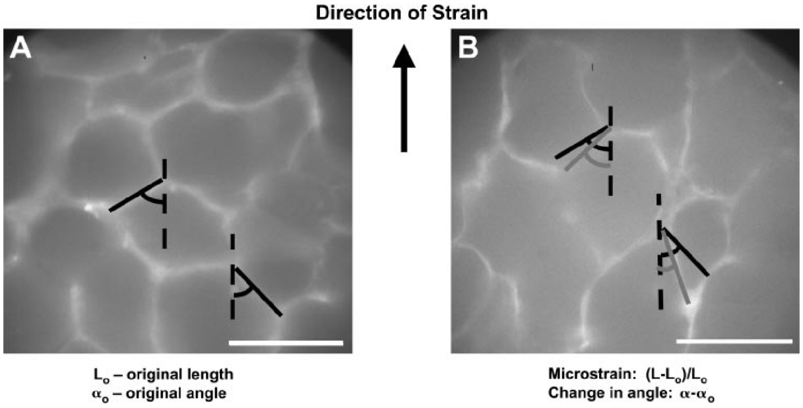

Figure 4.14: An example of the measurements of microstrain and change in angle of individual alveolar wall segments. At 0 % strain (A), the alveolar wall segments are traced and their lengths L and angles with respect to the direction of strain α_0 are measured. At 30 % strain (B), the new lengths l and angles α are measured. Microstrain is defined for each segment as the change in length divided by the length at 0 % strain, and change in angle is the current angle minus the angle at 0 % strain. Bar equals 100 µm. Figure taken from Brewer et al. (2003).

They found considerable heterogeneity within the micro strains and the change in angle of the alveolar walls, see Figure 4.14, which they interpreted based on their network model. However, due to the imaging technique, the authors were only able to investigate two-dimensional images of a three-dimensional deformation state.

A similar method was used by Cavalcante et al. (2005). They investigated the influence of the tissue constituents in the alveolar wall. Among others, they compared the local extension of the alveolar wall with the global deformation of the strip.

DiRocco et al. (2006) investigated the dynamics of rat alveoli *in vivo*. They utilized videomicroscopy to image the alveoli located directly beneath the pleura. The change in area between inspiration and expiration of manually outlined alveoli was calculated for healthy and diseased lungs. The imaging technique is again two-dimensional and additional only subpleural alveoli can be investigated, which are pathologically not as important during ARDS.

Perlman and Bhattacharya (2007) utilized real time confocal microscopy to determine the micro mechanics of alveolar perimeter distension in perfused rat lungs. They were able to image a 2-µm-thick optical section 20 µm under the pleura. They identified the alveoli to be polygons with five to eight corners, which is in contrast to the abovementioned authors who claimed that the alveoli are hexagons. The average length of these segments was compared for normal and hyper inflation. They found the segment distension to be heterogeneous within the single alveolus. Two shortcomings of this technique are that the alveolar extension is measured only in two dimensions and due to the imaging technique, only alveoli located close to the pleura can be included.

4.1.4 Cell Experiments (Mechanotransduction)

As mentioned above, mechanical stimulation of cells, for example during mechanical ventilation, can cause biochemical and biomolecular alterations. This mechanism is called mechanotransduction. The lung is a dynamic organ being exposed to varying mechanical forces throughout life. However, the magnitude of mechanical deformation observed during injurious mechanical ventilation are unlikely to occur during natural breathing. For this reason, the inflammation is probably not due to evolutionarily developed processes, rather is an unwanted reaction. For more details see Dos Santos and Slutsky (2006).

To get a better understanding of the kind of stretching causing inflammation, *in vitro* experiments on cells were performed. In this section, selected studies are briefly reviewed to present the variety of outcomes.

Vlahakis et al. (1999) found cyclic cell stretch to cause an inflammatory response in human alveolar epithelium in the absence of structural cell damage stimulation. In their experiments, they cultured alveolar epithelial cells on a deformable silicoelastic membrane. When stretched by 30 % for up to 48 h, the cells released $49 \pm 34\,\%$ ($P < 0.001$) more

IL-8, a major mediator of the inflammatory response, than static controls. This led to the conclusion that deformation itself can trigger inflammatory signaling.

Ning and Wang (2007) investigated the influence of the pathological state of human alveolar epithelium on cell response to different mechanical stretches. In contrast to Vlahakis et al. (1999), they found IL-8 release already after 5 % strain.

Copland and Post (2007) performed cyclic continuous radial elongations, of 5, 10, and 17 % on fetal lung epithelial cells. These stretches were applied with a frequency of 30 cycles/min. Control cells were grown on Bioflex collagen I plates, treated in the same manner as stretched cells but were not subjected to stretch. They compared the appearance of diverse signaling mechanisms of the stretched and the control group.

Summing up, there is a disagreement in the literature: the strain magnitudes, which cause an inflammatory reaction, vary between 5 and 30 % during cyclic loading.

4.2 Lung modeling

A major problem is that there is no possibility to measure local deformations *in vivo*. For this reason, a connection between the global deformation of a tissue strip or the whole organ and the strains occurring in individual cells lining the alveolar walls is needed. However, due to the complex alveolar geometry, the determination of this relationship is not straightforward.

There are several different approaches for modeling the individual alveolar wall and lung parenchymal tissue. Due to the large number of modeling approaches, only some selected examples will be introduced in this section. In the following, two different approaches will be distinguished: first, network models and second, continuum mechanical models.

4.2.1 Network Models of Lung Parenchyma

Network models assume that the resistance to deformation is provided solely by the supporting fiber network (CF and EF). Corresponding models approximate alveolar tissue by an arrangement of discrete elements representing the connective tissue fibers without considering the effect of the surrounding GS. In this section, three exemplarily network models are introduced.

Wilson and Bachofen (1982) developed a two-dimensional model for the mechanical structure of alveolar ducts. Their model consists of two networks: the first one is solely dependent on changes of the lung volume; the second one is composed of line-elements, forming the rims of the alveolar openings, which are extended by the outward force of surface tension. The alveolar walls themselves are neglected as mechanical components, although they are the place, where for surface-tension on the air-liquid interface occures. Their model mimics the relations between surface area, recoil pressure, lung volume, and surface tension. It shows consistent results with published data of lung volumes below 80 % TLC. Furthermore, the model shows qualitative agreement with the p-V curves presented by Budiansky and Kimmel (1987).

Maksym and Bates (1997) presented an one-dimensional material model for lung tissue including the load-bearing constituents, CF and EF. The fiber pair is modeled as a spring for the EF and a non-linear string element, extending to a limited length for the CF. Multiple fiber pairs can be used in series to create analytical and numerical models. The calibration of the model was performed on stress-strain curves of dog lungs and can also be applied to p-V curves of human lungs.

Mishima et al. (1999) developed a two-dimensional elastic spring network model representing a slice of lung tissue. The model consisted of a 500×500 grid of nodes connected in a square grid with prestressed springs, capable of stress relaxation or adaption. The border nodes of the grid were fixed and the internal nodes were free to move. Areas of low tissue density in a Computed tomography (CT) image, were mimicked by randomly removed nodes from the grid.

Cavalcante et al. (2005) developed a two-dimensional network model of non-linear springs connected with pin joints, see Figure 4.15. This model is not only able to reproduce experimentally determined stress-strain curves but also to predict microscopic distortion of alveolar constituents, CF and EF. Based on microscopic images, the springs are arranged as hexagons. Each spring represents the combined material behavior of the CF and EF with a second-order force-length relationship. The nodes at the top and bottom of the network are fixed. Due to the hexagonal shape, the network itself is unstable. For this reason, the springs were constrained against rotation. This model shows good agreement with experimentally determined stress-strain curves from the same paper.

4.2.2 Continuum Mechanical Models

The continuum mechanical approach models a body as a continuum mass, rather than resolving its micro-structure. For the alveolar tissue, there are several possibilities: first, the individual alveolar wall is modeled as a continuum, which is numerically very expensive

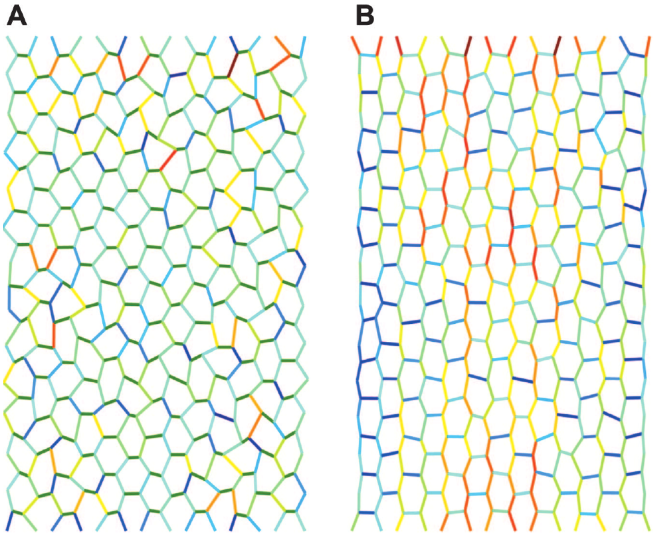

Figure 4.15: Elastic network model at 30 % strain in the vertical direction. (A) A stiff network. (B) A soft network. Color is proportional to the energy carried by the springs. The maximum energy values corresponding to dark red on A and B are different. Figure taken from Cavalcante et al. (2005).

but includes geometric information; second, the parenchymal tissue is modeled as a compressible homogeneous material; and third, the whole lung is modelled as a continuum. In this section, SEFs, see section 3.2, which were proposed in the literature for lung tissue will be introduced, before giving some examples of finite element (FE) models.

4.2.2.1 Strain Energy Density Functions

In this section, is split up into a part for homogenized or phenomenological and one part for constituent-based SEFs. Homogenized SEF relates to SEFs, which phenomenological describes the behavior of the lung parenchyma. Constituent-based SEF relates to SEFs, which are split up into summands representing the contribution of the parenchymal constituents, like the CF and EF. The differentiation between homogenized and constituent-based material models is a differentiation of mechanical effects which are or are not included within the models, it must not be mistaken for the isochoric volumetric split introduced in section 3.2, which is a solely mathematical transformation.

Homogenized Strain Energy Density Functions Frankus and Lee (1974) and Lee and Frankus (1975) proposed the following coupled SEF for lung parenchymal tissue,

$$\begin{aligned}\Psi_{\mathrm{v}} =& c_1 I_1 + c_2\left(I_1^2 - 2I_2\right) + c_3\left(I_1^3 - 3I_1 I_2 + 3I_3\right)\\ &+ c_4\left(I_1^4 - 4I_1^2 I_2 + 2I_2^2 + 4I_1 I_3\right) + c_5 I_2\\ &+ c_6\left(I_2^2 - 2I_1 I_3\right) + c_7 I_3 + c_8\left(I_1 I_2 - 3I_3\right)\\ &+ c_9\left(I_1^2 I_2 - 2I_2^2 - I_1 I_3\right),\end{aligned} \tag{4.2.1}$$

with $c_1 - c_9$ being material parameters and $I_1 - I_3$ are the invariants of the right Cauchy–Green strain tensor $\mathbf{C}$, see equation (3.2.10). In general, the presented SEF does result in a stress free reference state (see equation (3.2.40)), however, they argue that this is less significant from the physiological point of view.

Gao et al. (2006) determined an exponential SEF but no information was given on how they controlled the volume change of the compressible tissue.

Constituent-Based Strain Energy Density Functions Mijailovich et al. (1993) developed a model, which mimics elastic and dissipative phenomena of the parenchymal tissue based on geometry and material properties. Their hypothesis was that the dissipative phenomena are mainly influenced by the FF within the parenchymal tissue. The complex three-dimensional fiber network was modeled with two ideal fibers with slipping interface surfaces leading to energy dissipation. This model is meant to reproduce stiffening with rate of deformation (Barnas et al., 1989b; Bates et al., 1989; Hildebrandt, 1969; Kikuchi et al., 1991; Navajas et al., 1992; Suki et al., 1989), softening with increasing cycle strain amplitude (Barnas et al., 1989a; Navajas et al., 1992), stress-strain loops for sinusoidal behavior, energy dissipation, stress relaxation function, and preconditioning effects. However, not all of these experimentally determined effects are reproduced adequately enough.

Lanir (1983) suggested that the SEF can be composed of a sum of two terms, one for the alveolar walls and another one for the surfactant film. However, he did not differ between the individual load-bearing elements within the alveolar wall. Sobin et al. (1988) proposed a SEF for the parenchymal tissue. This SEF was determined by adding up contributions for SEFs of the CF and the EF, cells, GS and interfacial tension. Grytz and Meschke (2009) suggested a SEF formulation especially for the contribution of CF in collagenous tissue.

However, the remaining problem is to determine the associated material parameters. To quantify the contribution of the individual load-bearing constituents, their contribution needs to be measured individually. One possibility is to destroy the corresponding constituent utilizing proteases (see section 4.1.2.4).

4.2.2.2 Finite Element Models

The finite element method (FEM) provides the possibility to simulate the deformation of the whole lung, the parenchymal tissue and the individual alveolar wall.

There are several studies investing the deformation of the whole lung. However, this work is focused on the local deformations, for this reason, only one example is mentioned, namely the work of West and Matthews (1972). They investigated the deformation of lungs caused by gravity. Additionally, they showed that due to the large deformation of the lung during ventilation, a non-linear analysis is needed.

The number of studies concerned with the local deformation of the lung parenchyma is very limited and mainly uses artificially generated geometries. A short overview is given in the following.

Denny and Schroter (1997, 2000) investigated the oscillatory behavior of an isolated alveolar duct. Their model includes discrete fibers as well as the surface tension acting over the air-liquid interface. The tissue is simulated using a visco-elastic model involving non-linear quasi-static stress-strain behavior combined with a reduced relaxation function. The surface tension force is simulated with a time and area dependent model of surfactant behavior. They used artificially generated geometries composed of truncated octahedra.

There are also several other groups investigating the mechanical behavior of artificially generated three-dimensional geometries (Karakaplan et al., 1980; Kowe et al., 1986).

Because of missing realistic images of alveolar geometries, all these methods used symmetric, generated octahedra and miss the complexity of the real geometry. In summary, none of the abovementioned studies were able to determine the local three-dimensional deformation state of the alveolar wall.

To the author’s knowledge, the only simulation performed on image-based two-dimensional alveolar geometries was performed by Gefen et al. (1999). The major advantage of this method is that it allows for the investigation of the strain distribution within the alveolar wall, whereas the abovementioned experimental methods only investigated overall wall extension. Despite these advantages they used a very simplified linear elastic constitutive model and a two-dimensional simulation. However, since the lung undergoes a three-dimensional deformation state, three-dimensional simulations are essential.

5 Goals

5.1 Long Term Goal

This work is part of the priority program ”Protective Artificial Respiration” funded by the German Research Foundation (DFG). The priority project consists of several groups with medical, biological, imaging and engineering backgrounds. *Its main goal is to further improve mechanical ventilation in order to reduce the high mortality rates due to VALI.* For this purpose, the Institute for Computational Mechanics (TUM) is developing a detailed “virtual lung model”, see Figure (5.1).

Our virtual lung model starts with the tracheo-bronchial region. Here, the airflow interacting with the deformation of the airway walls and the surrounding parenchymal tissue, the fluid-structure interaction (FSI), is simulated. The FSI is important to reproduce *in vivo* fluid mechanics in the tracheo-bronchial region, as well as stresses and strains in the airway wall, which are potentially associated with the onset of inflammation and remodeling of the epithelium (Wall and Rabczuk, 2008). Due to limitations on the number of visible airways in CT scans, only a part of the airway tree can be resolved in three-dimensions. Therefore, realistic boundary conditions at the outlets of the three-dimensional domain are developed. To take the peripheral region into account simplified reduced-dimensional airway trees are coupled to every outlet of the three-dimensional region (Comerford et al., 2010; Ismail et al., 2012). The flow in individual acini can be linked to the structural deformation of the parenchyma, utilizing a newly developed volume-coupling method (Yoshihara and Wall, 2012). From these deformations, strains and stresses in the individual alveolar walls can be determined by using a multi-scale approach (Wiechert and Wall, 2010). The deformation within the alveolar walls is our main interest, since this is the area where the inflammation during VALI initiates. For more details of our virtual lung model, e.g. see Wall et al. (2010b).

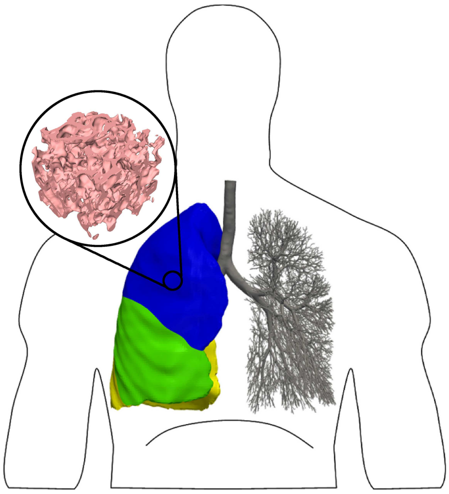

Figure 5.1: Schematic of the ”virtual lung” model developed at the Institute for Computational Mechanics (TUM). This model considers the effects of airflow in the tracheo-bronchial region on the parenchymal deformation, via volume-coupling and, thereby, on stresses and strains in individual alveolar walls using a multi-scale approach.

5.2 Specific Goal

The specific goal of this study is to develop material models for the alveolar parenchyma that will enable to determine the global stresses and strains in the tissue. Based on these strain states, the relevant strains within the alveolar wall will be determined utilizing a FE simulation of image-based alveolar geometries. The deformation within the alveolar wall is of utmost importance, since overstretching of the alveolar walls is the primary cause of inflammation during VALI. Since the alveolar wall is too small and inaccessible to allow direct measurements of its material behavior (Wilson and Bachofen, 1982), computational models can provide essential insight into involved phenomena.

To develop a sophisticated material model, the lung tissue is first experimentally characterized. To determine the influence of the load-bearing tissue constituents, like CF, EF, FF, and GS, the tissue is treated with enzymes, destroying the fiber families, during the tests. In the next step, several non-linear, compressible and elastic material models are optimized using an inverse analysis approach. The experiment is numerically simulated with the material parameters being iteratively improved until the experimental and numerical results match. Based on this approach the two bet suited material models are selected, a phenomenological material model and a model accounting for the individual contribution of the load-bearing tissue components and their interaction. The presented methodology is not limited to lung parenchyma but can be applied to other materials in an equivalent manner.

The actual damage during VALI occurs due to overstraining of the alveolar wall. For this reason, the strain state within the individual alveolar wall needs to be quantified. Because of the foam-like structure of the lung parenchyma, the local deformation of the alveolar wall cannot be directly deduced of the global deformation of the lung parenchyma. Furthermore, the currently available classical imaging techniques, i.e. CT, magnetic resonance imaging (MRI) etc., do not have a sufficient resolution to image the deformation state in vivo. However, using the novel imaging techniques presented by Schittny (2008) the individual alveolar walls of fixated rat lungs are visible with adequate resolution. Based on these images and a prescribed global strains a three-dimensional deformation state can be determined by FE simulations.

In this work, all simulations are based on the FEM. For more details on this method the interested reader is referred to textbooks from Belytschko et al. (2005); Hughes (2000), and lecture notes from Wall et al. (2010a, 2012).

All material models of this work were implemented in the in-house FE software platform Bavarian Advanced Computational Initiative (BACI, Wall and Gee (2010)). This multipurpose parallel research-code is written in C++ and integrates open-source libraries of the Trilinos Project (Heroux et al., 2005). BACI has been and is developed jointly at the Institute for Computational Mechanics (Technische Universität München).

It has to be noted, though, that the introduced material models are based on general solid continuum mechanics, i.e. they are not limited to the FEM.

5.3 Specific Aims

The above introduced goals can be narrowed down to the following five specific aims:

AIM 1

To develop an experimental testing protocol in order to determine the elastic material behavior of lung parenchyma.

AIM 2

To extend the experimental methodology to investigate the influence of the individual tissue constituents (CF and EF).

AIM 3

To develop an inverse analysis methodology in order to deduce a hyperelastic material model for soft biological tissue from experiments.

AIM 4

To determine a phenomenological and a constituent-based material model for lung parenchyma.

AIM 5

To perform a FE simulation on image-based alveolar geometries, in order to determine the deformation within the alveolar walls for a given global deformation state.

6 Experiments

Although experiments on lung parenchymal tissue have been carried out since the late 1960s, they mainly focused on the qualitative mechanical behavior. Thus, from these results it is difficult to determine a quantitative stress-strain relationship for computational simulations. The major drawbacks of previous experimental approaches are:

- Global p-V measurements are too coarse to determine a sophisticated material model for lung parenchyma. The problem is that a distinction between the individual contribution of the airways and the parenchymal tissue is not possible.
- Only a few studies use viable tissue. However, it has not been satisfactorily shown that cell death does not change the material behavior of parenchymal tissue.
- The production of the tested specimens was performed by hand rather than fully automated, which can cause large variations in the dimensions of the specimens.
- In many studies the tissue was frozen in order to cut the specimen, which has been shown before to change the material properties of the tissue.
- Many studies perform their experiments only on one single specimen, i.e. there is no information about the repeatability of the experiment or the statistical spread of the measured values.
- The lateral contraction or other measurements determining the volume change of the compressible lung parenchyma have only been determined in multi-axial tensile tests.
- In some studies critical information, i.e. cross-sectional area or length, were not provided at all or their determination was not further specified.
- In most cases, it was poorly documented, which initial length (before or after preconditioning) or initial cross-sectional area (including the air-space or not) was taken, or how these quantities were determined. This is very important, since these quantities have an essential influence on the scaling and position of the determined stress-strain curves.

For all these reasons, it appears necessary to perform additional experiments. In this chapter, the experimental methodology utilized in this study is introduced followed by the experimental results, their discussion, and a short conclusion.

6.1 Methodology

In this section, an overview of the experimental methodology is given. For the experiments, living precision-cut lung slices (PCLS) are used. Their preparation will be described in detail below. As several studies (Hoppin et al., 1975; Tai and Lee, 1981; Sobin et al., 1988; Toshima et al., 2004) have shown that lung parenchymal tissue is isotropic, uniaxial tensile tests can be considered sufficient. The lateral contraction of the specimens is measured in addition to determine the volume change of the specimen.

6.1.1 Specimen Preparation

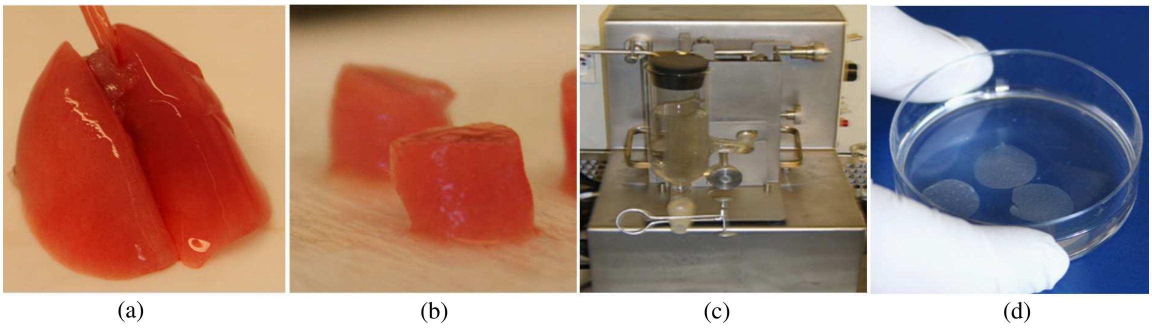
(a) (b) (c) (d)

Figure 6.1: Preparation of living precision-cut lung slices (PCLS). (a) Lungs are dissected from the rats and filled with agarose solution (1.5 %). (b) Utilizing a coring tool, cylindrical cores with a diameter of 14 mm are cut. (c) The cores are placed in a Krumdieck tissue slicer (Alabama Research and Development, Munford, AL) and 0.5 mm thick slices are cut as shown in (d).

The PCLS are prepared from isolated rat lungs as described by Martin et al. (1996). All animal experiments are approved by the local authorities. Female Wistar rats obtained from Harlan Winkelmann (Borchen, Germany) are maintained on laboratory food and tap water ad libitum in a regular 12 h dark night cycle at a temperature of 22 °C. Briefly, the lungs are dissected from the animals, filled with agarose solution (1.5 %) via the trachea, and put on ice to allow the agarose to cool and solidify. The lung lobes are separated and cut into tissue cores utilizing a coring tool. These cores with a diameter of 14.0 mm are cut into 0.5 mm thick slices with a Krumdieck tissue slicer (Alabama Research and Development, Munford, AL), see Figure 6.1.

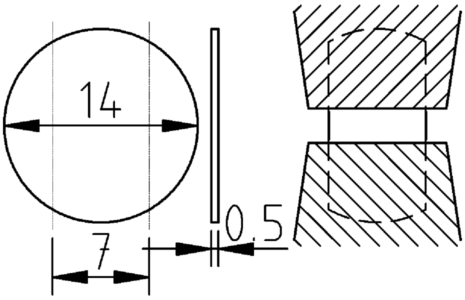

Figure 6.2: The left hand picture shows the dimensions of precision-cut lung slices (PCLS) in mm. The right hand picture shows how the specimen is clamped into the uniaxial tensile tester. The extension direction is vertical.

The thickness of the slices is measured with a light microscope. For this purpose, the change of the focus in the presence and absence of a slice between two microscopic slides is determined. The two sides of the round slices are trimmed with two parallel razor blades giving a tissue strip with a width of 7.0 mm, leading to a cross-sectional area A of 3.5 mm^2, see Figure 6.2. These strips are incubated in minimal essential medium (MEM) and the agarose is washed out by frequently changing the medium within the first 4 h and completing an overnight incubation. Kononov et al. (2001) have shown that the agarose does not change the mechanical properties of the parenchymal tissue.

Previous tests have shown that PCLS are viable for more than three days and the experiments in this study are performed within 48 h after removing the lung (Martin et al., 1996).

PCLS have several advantages: first, since they are very thin, it is possible to get multiple specimens of the same animal, allowing statistical analysis to be performed; second, the cutting method does not change the material behavior of the tissue, since there is no need to further fixate the tissue during cutting; and third, the dimensions of the individual specimens can be adjusted very precisely.

6.1.2 Testing Apparatus

The specimens are probed with the uniaxial tensile tester Bose ElectroForce 3100 (Bose Corporation, Eden Prairie, USA), see Figure 6.3. For testing, the specimens are fixed between two clamps (Figure 6.2 and 6.3), which are specifically designed and manufactured for the use with PCLS. The advantage of these clamps is that they prevent both slipping and tissue damage. One of the clamps is connected to a force transducer and the other one to a displacement transducer. The force transducer has a range of ±0.5 N and a resolution of 2.5 mN and the displacement transducer has a range of ±2.5 mm and a resolution of 12.5 µm. In order to minimize external influences, such as gravity and vibrations, all tests are performed in the horizontal plane. Frequencies higher than 20 Hz are filtered out utilizing a low pass Butterworth filter.

For mounting of the specimens in the machine, the following protocol is used: first, the specimens are straightened out on a piece of aluminum foil, second, the aluminum foil with the tissue on top is lightly fixed between the clamps, and third, the foil is removed before the two clamps are completely fastened. This procedure assures that the PCLS are mounted without internal stresses or sagging. The initial length of the test domain of the specimen is exactly $L_0 = 2.0\,\text{mm}$, the distance between the two clamps.

In the following, the direction of the clamp movement will be referred to as x-direction and the perpendicular direction in the horizontal plane as y-direction, see Figure 6.4.

Due to the compressibility of parenchymal tissue it is not enough to determine the displacement in x-direction exclusively. An additional measurement related to the volume change is needed. However, since the material model is determined utilizing an inverse analysis, see section 7.1.3, the y-displacement at one individual point over time is sufficient. One example point is shown in Figure 6.4.

While the displacement in x-direction is directly measured via the displacement of the clamps, the y-displacement of an individual point has to be determined with a videomicroscopy. To do so, the following steps are needed:

- During the tensile test a movie is recorded.
- The movie is cut to the right length, in order to include exactly one sinusoidal oscillation and split into individual images.
- The images are then straightened and cropped to the region of interest.
- The scaling factor is determined by measuring the number of pixels of the perpendicular connection between the two clamps, which is known to be exactly $L = 2.5\,\text{mm}$ at the start of the measurement after preconditioning, see section 6.1.3.
- The point P is tracked, using the image processing software ImageJ (Abràmoff et al., 2004) and its module ”Manual Tracking”. This software tool returns the y-displacements of P.

These measurements are then used as an additional input parameter for the inverse analysis, see section 7.1.3.

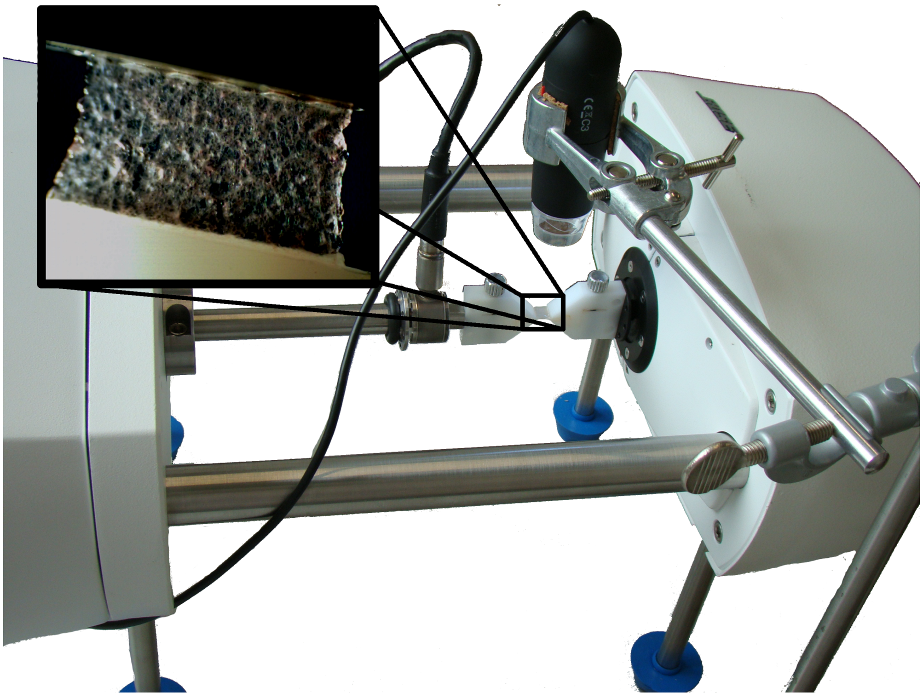

Figure 6.3: Bose ElectroForce 3100 (Bose Corporation, Eden Prairie, USA) is a uniaxial tensile tester. The force transducer has a range of ±0.5 N and a resolution of 2.5 mN and the displacement transducer has a range of ±2.5 mm and a resolution of 12.5 µm.

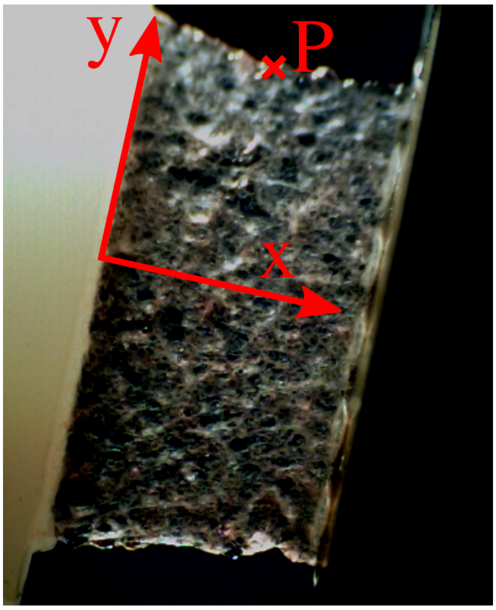

Figure 6.4: Definition of x- and y-direction in the experiment and the simulations. The x-direction is the direction of the clamp movement and the y-direction is the corresponding perpendicular direction in the horizontal plane. P marks an exemplary point where the y-displacement is measured during the experiment.

6.1.3 Testing Protocol

For a reliable characterization of parenchymal lung tissue, a sound testing protocol is essential. For this reason, some additional preliminary tests are performed. Based on these preliminary studies and on results presented in the literature, see section 4.1.2, an appropriate testing protocol is developed.

The testing is further split up in two testing series: first, the homogenized material behavior of lung parenchyma is determined in order to study repeatability, variation between animals, etc.; second, similar tests are performed on proteinase treated PCLS in order to determine the influence of the individual load-bearing constituents.

All experiments are performed at room temperature.

6.1.3.1 Preliminary Studies

Strain Rate Dependency The strain rate dependency is tested for 0.5, 1.0, and 2.0 Hz, which represent breathing rates between $70 - 115$ breath/min. The variation in frequency shows no significant influence, see Figure 6.5. These findings are in line with the results of Fung (1993); Fredberg and Stamenovic (1989).

Influence of Surface Tension The effect of surface tension is tested by performing the same experiments in air and in fluid. As can be seen in Figure 6.5, there is no significant difference between the stress-strain curves. Hence, it is assumed that surface tension effects do not play a role in this experimental setting. Consequently, the methodology proposed in this work is suitable to characterize the behavior of tissue alone. The resulting parenchyma model can be combined with a previously developed model accounting for the contribution of the surface tension (Wiechert et al., 2009). This way, both effects can be incorporated yet remain clearly distinguishable and their respective influence can be studied.

6.1.3.2 Preconditioning

Although lung tissue, like most soft biological tissues, is to a certain extent viscoelastic, the overall material behavior is dominated by the elastic response. Viscoelasticity in the lung parenchyma is associated with both relaxation and creep phenomena, which have been described before by several authors, e.g. Fukaya et al. (1968); Fung (1984); Suki et al. (1994). Since description of these viscoelastic phenomena is not trivial, in this work the focus is on the elastic effects as a first step, although viscoelasticity may be included in the future. For this reason, a preconditioning protocol it used, which reduces the viscous effects. Hence, they can be neglected in the following analysis.

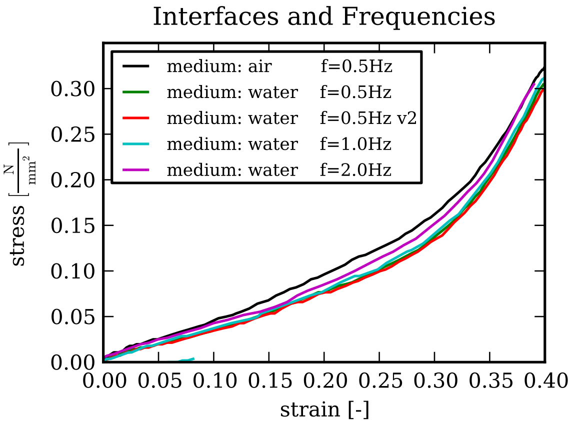

Figure 6.5: Influence of different strain rates and surface tension on stress-strain curves.

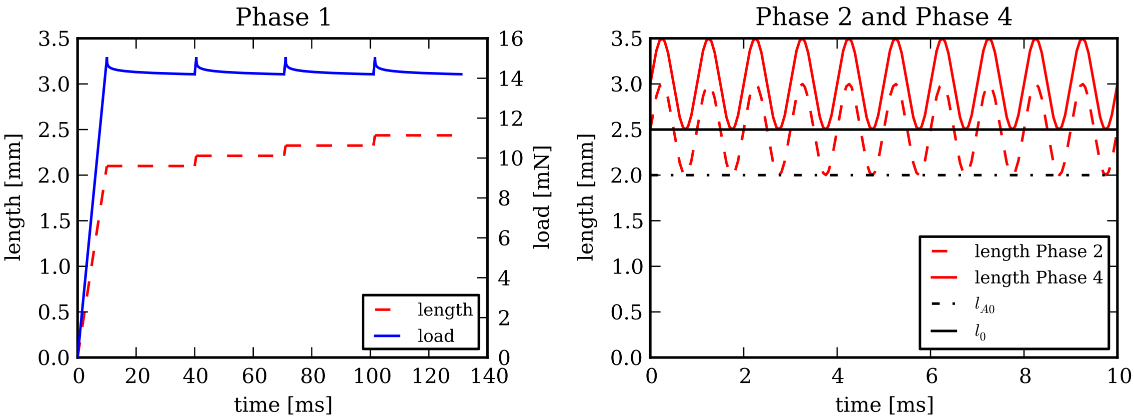

Figure 6.6: Preconditioning of the parenchymal tissue strips for eliminating viscoelastic material behavior. (left) Phase 1: The tissue slice is stretched with a constant velocity of 0.5 mm/s until a force of 15 mN is reached followed by a 30 s relaxation phase. This procedure is repeated 10 times. (right) Phase 2 and 4: the specimen is sinusoidally loaded. The dashed lines show the course of length of the specimen before preconditioning and L_0, whereas the solid line shows the length after preconditioning and L.

The protocol consists of four phases:

Phase 1: The tissue slice is stretched with a constant velocity of 0.5 mm/s until a force of 15 mN is reached. The displacement is held constant for 30 s. During this relaxation time the tissue adjusts itself to the deformation, thus it relaxes and the force drops. This loading and relaxation is repeated approximately 10 times until the force remains constant at a plateau of $\sim 14\,\mathrm{mN}$ (Figure 6.6(left)) i.e. 1 mN below the originally applied 15 mN. Thus, the drop due to viscous release is only 1/15.

Phase 2: The tissue is loaded with a displacement controlled sinusoidal curve with a peak amplitude of 0.5 mm, a mean of $L_0 + 0.5\,\mathrm{mm}$ and a frequency of 1.0 Hz, see Figure 6.6(right).

Phase 3: Due to relaxation phenomena, the tissue strip elongates during the first two preconditioning phases. For this reason, the new initial length L is determined by slowly extending the tissue strip until a small force of $\approx 0.005\,\mathrm{mN}$ is reached; the new initial length $L \approx 2.5\,\mathrm{mm}$, see Figure 6.6(right).

Phase 4: The tissue is again loaded with the same sinusoidal oscillations as described in Phase 3 but the mean value is shifted to L, meaning the minimum of the sine wave is the new initial length of the tissue strip.

Preliminary studies have shown that after performing this preconditioning protocol, the time dependent effects of the lung tissue in the following experiments are negligible.

6.1.3.3 Homogenized Lung Parenchyma

In total, 47 PCLS, from five exbreeder female rats between nine and 15 months (Table 6.1), were examined. After preconditioning, the tissue is loaded with sinusoidal oscillations, similar to the one used during preconditioning, i.e. with a peak amplitude of 0.5 mm, a mean of $l_0 + 0.5\,\mathrm{mm}$, and a frequency of 2.0 Hz. Forces and displacements are sampled at 100 Hz.

Table 6.1: Weights of the rats and number of tested specimens per rat.

Rat	1	2	3	4	5
weight [g]	303.7	307.8	308.1	334.9	293.8
number of tested PCLS	6	10	8	7	16

6.1.3.4 Constituent-based Lung Parenchyma

In total, 21 PCLS are examined, 10 of them are treated with collagenase first and the remaining 11 are treated with elastase first. This testing protocol allows to individually determine the influence of the two fiber families and the GS on the mechanical behavior of the parenchymal tissue.

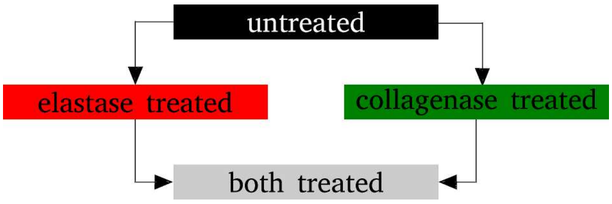

Figure 6.7: Schematic drawing of the experiment protocol. 11 of the 21 tested precision-cut lung slices (PCLS) are tested with elastase prior to collagenase treatment ("elastase treated"), whereas 10 are tested with collagenase prior to elastase treatment ("collagenase treated").

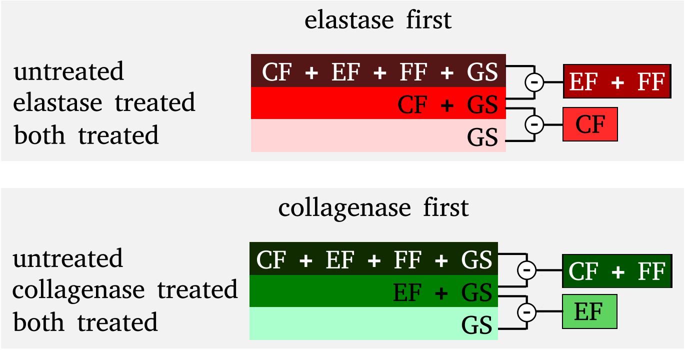

Figure 6.8: The first treatment destroys the first fiber family as well as the fiber-fiber interaction (FF) between the collagen fibers (CF) and elastin fibers (EF). After the second treatment, the only remaining load-bearing element is the ground substance (GS). By subtracting the individual determined stress-strain curves from each other, the contribution of the individual components can be calculated, e.g. EF+FF, CF, CF+FF and EF.

The actual testing is similar as described above for the homogenized lung parenchyma. However, after the untreated PCLS are tested the specimens undergoes the protease treatment with either elastase (i.e. "elastase treated" in Figure 6.7) or collagenase (i.e. "collagenase treated" in Figure 6.7) to destroy the respective fiber family.

The protease incubation takes place with the specimens remaining mounted within the tensile tester, to ensure that the exact same part of the specimen is tested again. For elastase treatment, the PCLS are incubated for 30 min in E7885 elastase from porcine pancreas-lyophilized powder, suitable for cell culture (Sigma-Aldrich). For the collagenase treatment, the PCLS are incubated for 30 min in collagenase H from Clostridium histolyticum (Roche). Due to the fact, that the PCLS are mounted in the tensile tester during the incubation, solution is repeatably drizzled on the specimen keeping the liquid film closed. After the first protease treatment, the specimens are tested again, including the preconditioning protocol, before they are treated with the corresponding other protease (indicated as “both treated” in Figure 6.8) and tested for the third time.

6.2 Results

In the following section the experimental results will be presented, which are used as a target for the material fitting. First, the results of the homogenized lung parenchyma are provided, in order to get a better understanding and a solid establishment and verification of the experimental protocol. Second, the results of the proteinase treated PCLS are presented.

In the following section strain and stress refers to $\frac{l}{L}$ and $\frac{\mathbf{T}}{A}$.

6.2.1 Homogenized Lung Parenchyma

First, the experimentally determined stress-strain curves of each of the five tested animals are compared. Figure 6.9 shows the mean curve, averaged over all tested PCLS of one individual animal, and the area between the mean ± one standard deviation (sd) (mean ± sd) and the mean ± 1.96 sd, i.e. 95 % of all values, highlighted as lighter and darker color, respectively. For a short explanation of the statistical measures, see Appendix A.4.1 and A.4.2. All shown curves are similar in shape and order of magnitude. However, a variation of curves for each animal exists. This variation does not correlate with the number of tested PCLS per animal.

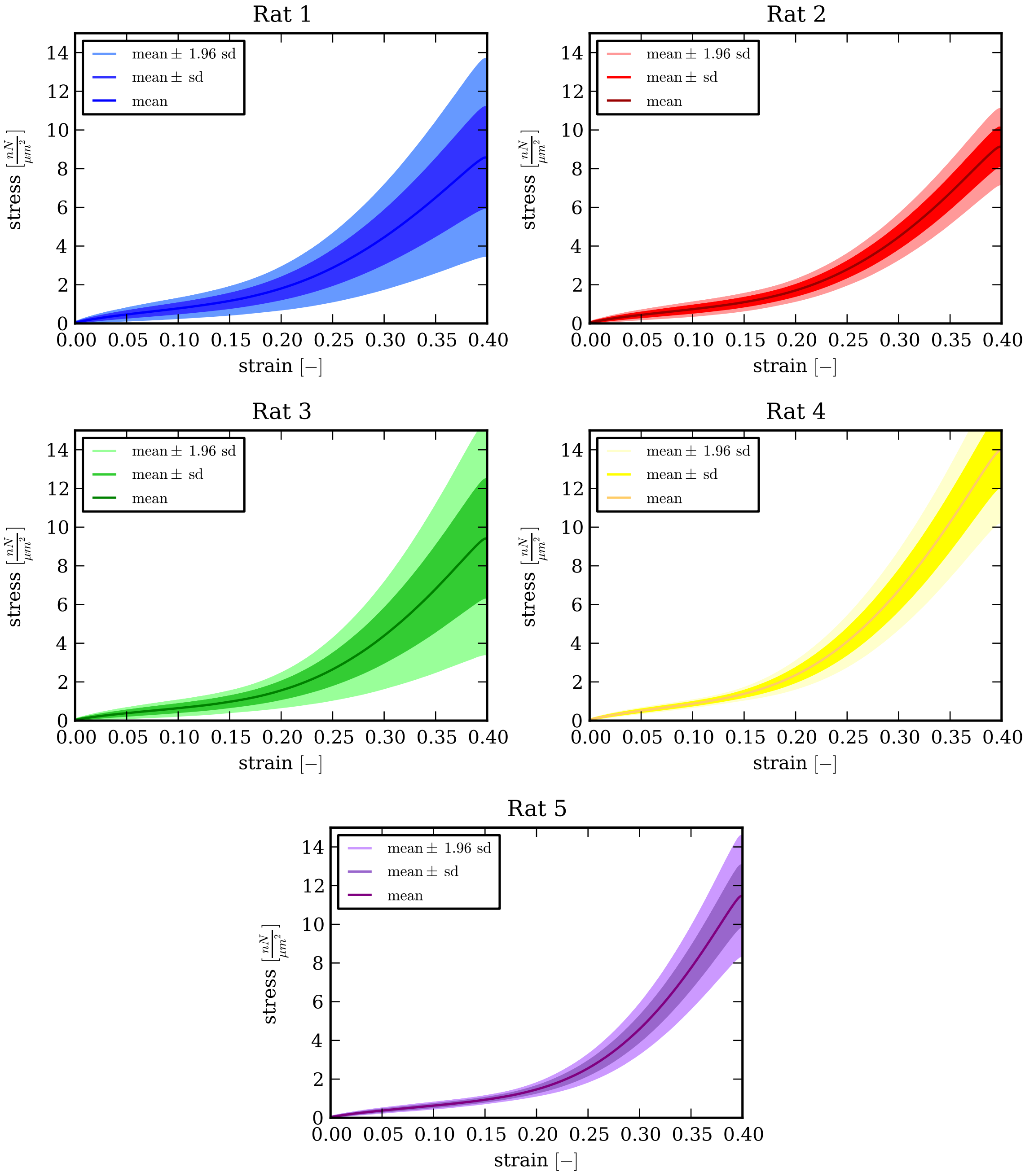

Figure 6.9: Comparison of stress-strain curves of each of the five rats The central line indicates the mean of all tested precision-cut lung slices (PCLS), the darker area represents mean ± sd and the lighter area represents mean ± 1.96 sd.

Second, the coefficient of variation (CV) of the individual rats is compared with the CV of all rats, see Appendix A.4.3. Figure 6.10 shows that the CV within the individual animals does not differ of the CV of all tested specimens.

Third, the mean, mean ± sd, and mean ± 1.96 sd stress-strain curves over all tested spec-

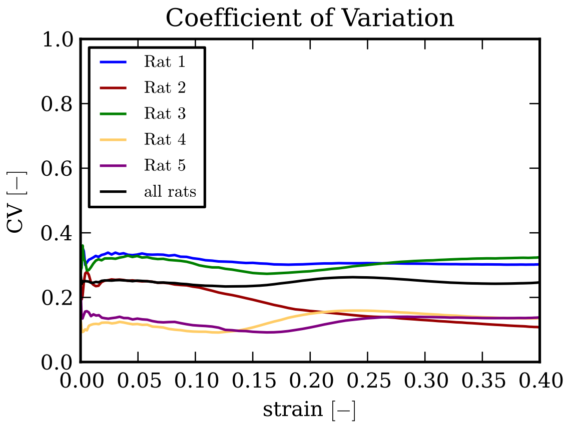

Figure 6.10: Comparison of the coefficient of variation (CV) of the individual rats with the CV of all rats.

imens are compared with the mean stress-strain curves of the individual rats. Figure 6.11 shows that the mean stress-strain curve is of similar shape than the stress-strain curves of the individual animals.

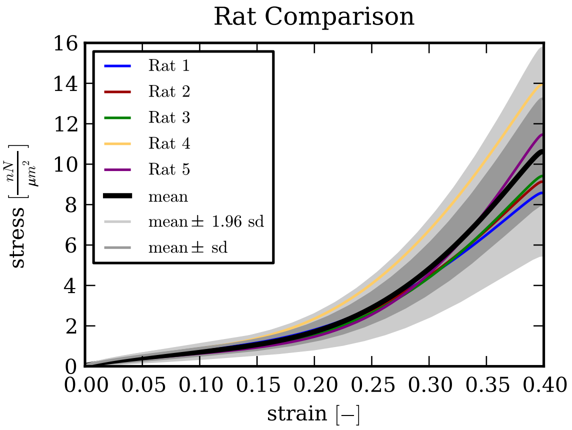

Figure 6.11: Comparison of mean stress-strain curves of each of the five tested rats with the mean, mean ± sd and mean ± 1.96 sd of all tested specimens. The central line indicates the mean of all tested precision-cut lung slices (PCLS), the darker area mean ± sd and the lighter area mean ± 1.96 sd.

6.2.2 Constituent-based Lung Parenchyma

As a next step, the contribution of the individual load-bearing constituents is investigated. For the analysis of the experiments, the PCLS are split up into two groups: the first group consists of the PCLS which are treated with elastase prior to collagenase (“elastase first”) and the second group consists of the PCLS which are treated with collagenase prior to elastase (“collagenase first”).

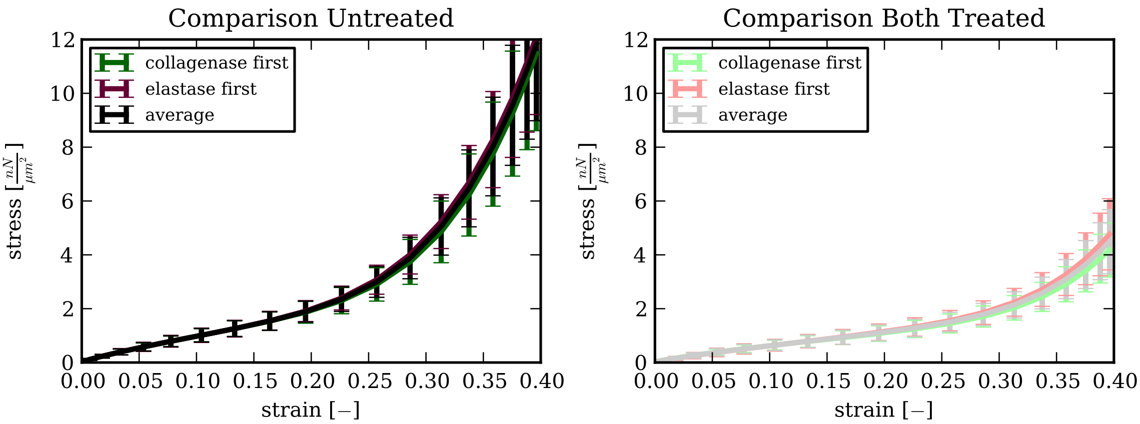

Figure 6.12: Comparison between the two analysed precision-cut lung slices (PCLS) groups for the untreated state (untreated) and after treatment with both proteases (“both treated”). The error bars indicate one standard derivation (sd).

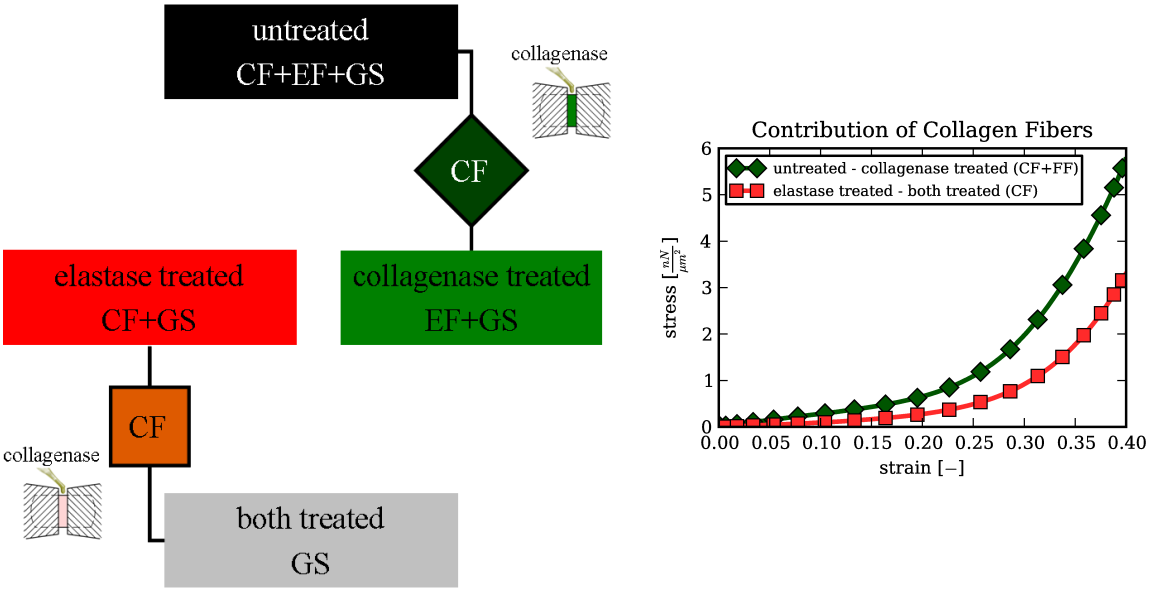

Figure 6.13: Comparison between the two possible calculation methods to determine the collagen fiber (CF) contribution within the lung parenchyma. The corresponding stress-strain curves are shown on the right hand side. The first method is to subtract the mean stress-strain curve of the “both treated” specimens from the collagenase specimens. The second method is to subtract the mean stress-strain curve of the collagenase treated specimens from the untreated specimens. The gap between the two possibilities is assumed to be due to the fiber-fiber interaction (FF).

First, the stress-strain curves of the untreated PCLS and of the “both treated” PCLS are compared, see Figure 6.12. The figure clearly shows that there is no difference between “elastase first” and “collagenase first” treatment.

Second, it is investigated, if there is difference calculating the CF contribution of the curves of the specimens treated with “elastase first” or with “collagenase first”. The CF contribution can be determined by the change of stress-strain curves after the collagenase treatment, see Figure 6.8. The idea behind this is: if there is no interaction between the two fiber families, there should be no difference in the change caused by the collagenase treatment. To investigate the stress-strain curve obtained by subtracting

- the elastase treated and the “both treated” curves for the “elastase first” treated group
- the untreated and the collagenase treated curves for the “collagenase first” treated group,

see Figure 6.13. Additionally, the according opposite scenario is investigated for the contribution of EF, see Figure 6.14. It can be clearly seen that there is a significant difference between the two calculation methods.

Third, the mean stress-strain curves of untreated PCLS, PCLS treated with elastase/collagenase, and PCLS treated with both enzymes are compared, see Figure 6.15. The untreated PCLS exhibit the stiffest behavior. The elastase treated PCLS show a softer mechanical behavior. The PCLS treated with collagenase are even softer than the elastase treated specimens. The PCLS treated with both enzymes show the softest behavior.

6.3 Discussion

In this section, a discussion about the experimental results is given, including a comparison with literature results.

6.3.1 Homogenized Lung Parenchyma

Investigating the differences between the various animals the mean stress-strain curves as well as their sd, are found to be similar in shape and magnitude, see Figure 6.9. This observation is backed up by the comparison of the CV, which turned out to be of similar order of magnitude within the individual animals and within all tested specimens, see Figure 6.10 and Figure 6.11. These results have several advantages: first, there is no

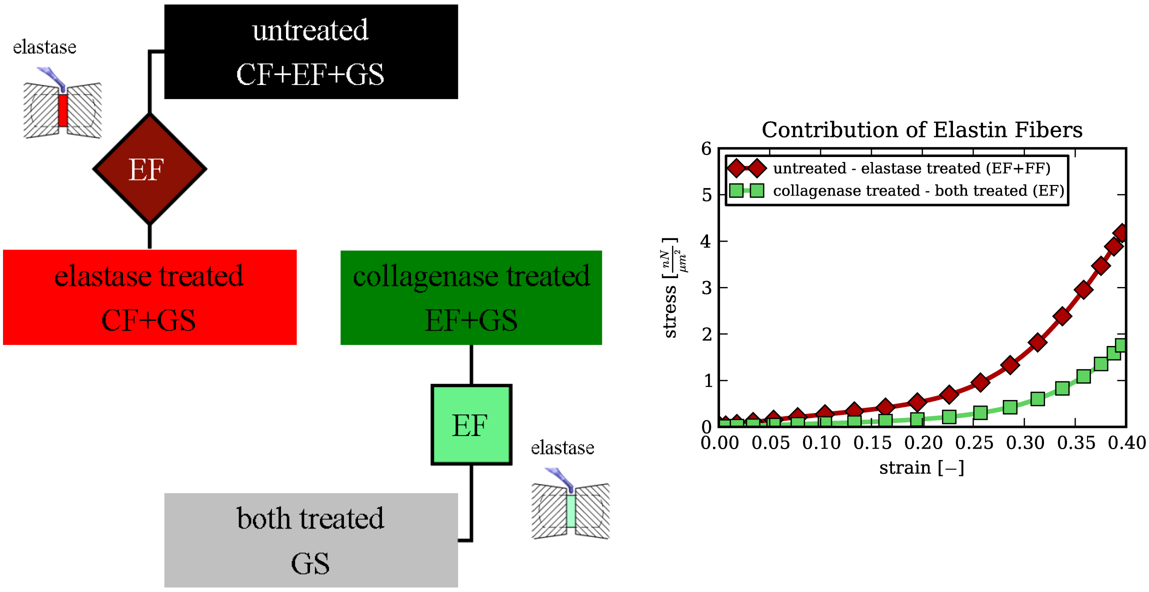

Figure 6.14: Comparison between the two possible calculation methods to determine the elastin fiber (EF) contribution within the lung parenchyma. The corresponding stress-strain curves are shown on the right hand side. The first method is to subtract the mean stress-strain curve of the elastase treated specimens from the untreated specimens. The second method is to subtract the mean stress-strain curve of the "both treated" specimens from the collagenase treated specimens. The gap between the two possibilities is assumed to be due to the fiber-fiber interaction (FF).

need to further distinguish between the individual animals, and second, the testing and the specimen preparation method are both robust and repeatable.

A comparison of the results of this work with stress-strain curves found in the literature (Fukaya et al., 1968; Sugihara et al., 1971; Hoppin et al., 1975; Vawter et al., 1978; Karlinsky et al., 1985; Mijailovich et al., 1994; Sata et al., 1995; Yuan et al., 2000; Jamal et al., 2001; Gao et al., 2006) is shown in Figure 6.16. This comparison revealed a rather large diversity of results of different studies. There are several reasons for this: first, considerable variations are observed between the specimens tested (i.e. dimensions, preparation method, preconditioning etc.); second, different species and testing methods (uniaxial, biaxial and triaxial) were used. However, all experimentally determined stress-strain curves are similar in shape, i.e. they show stiffening for large strain.

It is obvious that the stress-strain curves suggested by Mijailovich et al. (1994) and Karlinsky et al. (1985) differ most, see Figure 6.16. The stress-strain curve suggested by Mijailovich et al. (1994) has a much smaller magnitude than the other ones. However, the reason for this could be the way they calculated the undeformed surface area A of their

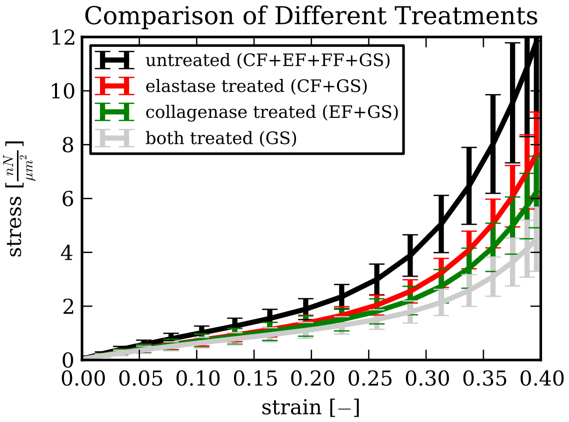

Figure 6.15: Averaged experimentally determined stress-strain curves of all untreated precision-cut lung slices (PCLS) (black), all collagenase treated PCLS (green), all elastase treated PCLS (red), and all collagenase as well as elastase treated PCLS (gray). The error bars indicate one standard derivation (sd). The graph shows a clear stress reduction if one or both of the load-bearing macromolecules are degenerated. The collagenase influences the initial slope as well as the curvature of the stress-strain curve, whereas the elastase reduces the initial slope of the curve.

strips, see section 4.1.2.1. Briefly, their A is based solely on the tissue area and not on a homogenisation of tissue and air area, leading to an about five times smaller area resulting in five time higher stresses than the ones in the present study. The stress-strain curve suggested by Karlinsky et al. (1985) also has a much smaller magnitude than the other ones. One explanation for this difference could be the measurement of the initial length. Karlinsky et al. (1985) determined the initial length with the specimen being adjusted in the machine, meaning under pretension (including the weight of the clamp and its own weight) which is neglected in the following measurements. Furthermore, the extension of 100 % over the initial length might have damaged the tissue in their study.

To sum up; the variation within the stress-strain curves presented in literature is rather big. The curve obtained in this study lies close to the majority of realistic curves in the upper third of the range.

6.3.2 Constituent-based Lung Parenchyma

The untreated and the “both treated” stress-strain curves for both treatment groups show good agreement, see Figure 6.12. For the untreated specimens, this is expected since in this case, both groups underwent no treatment at all. For the “both treated” specimens both groups underwent the same treatment but in different order, which did not influence

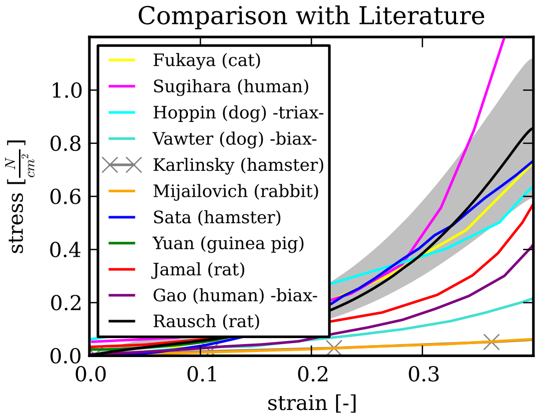

Figure 6.16: Comparison of the stress-strain curve, obtained in this study, with curves presented in literature Fukaya et al. (1968); Sugihara et al. (1971); Hoppin et al. (1975); Vawter et al. (1978); Karlinsky et al. (1985); Mijailovich et al. (1994); Sata et al. (1995); Yuan et al. (2000); Jamal et al. (2001); Gao et al. (2006). The black line indicates the mean stress-strain curve over all 47 tested specimens from this study and the gray area represents ± one standard deviation (sd).

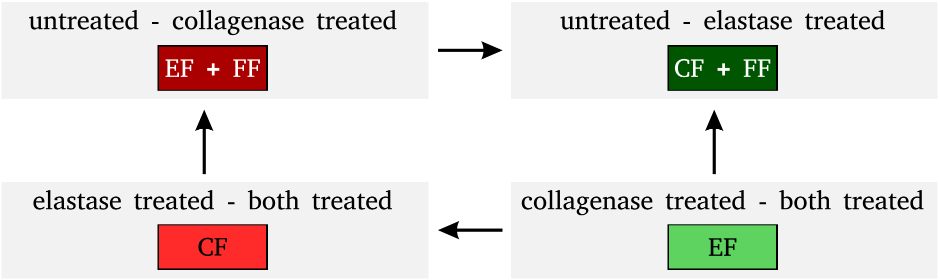

Figure 6.17: Comparison of the stiffness for the two calculated elastin contributions and the two calculated collagen contributions. The arrows are pointing towards the stiffer contribution.

the overall result. This shows that once treated with both proteases, the specimens show similar stress-strain curves, within tolerances comparable to the untreated specimens.

In the second comparison, the difference between the two calculated stress-strains curves, concerning CF and EF, is investigated. The two curves show different stress-strain behavior, see Figure 6.13 and 6.14. This change can be explained by the interaction between the two fiber families, i.e. fiber-fiber interaction (FF). This means the two fiber families do not act independently. There are two additional arguments supporting this hypothesis. First, both CF+FF and EF+FF are stiffer than CF and EF, respectively. Since the fibers can only interact if both fiber families are present, the contribution of the FF is only present in the first calculation method when the corresponding other fiber family still exists, whereas in the second calculation method the corresponding other fiber family has been destroyed in advance. Second, upon closer investigation of the stiffness of the individual measured PCLS (data not shown), it turned out that for the “elastase first” treated specimens, where EF+FF and CF are calculated, EF+FF is always stiffer than CF. However, for the “collagenase first” treated specimens, where CF+FF and EF are calculated, CF+FF is always stiffer than EF. This means the first determined fiber contribution is stiffer than the second determined fiber contribution independent of which fiber family this is. By comparing the mean stress-strain curve of the CF and EF with the same calculation method, i.e. EF+FF with CF+FF and EF with CF, the CF turned out to be stiffer, see Figure 6.17. This seams reasonable, since the CF are known to be stiffer than the EF. This again backs up the assumption that with the first treatment not only one of the fiber family was destroyed but also the FF.

In the third comparison, the differences between the different treated PCLS are investigated, see Figure 6.15. The untreated PCLS still include all major load-bearing elements (CF+EF+GS) and FF, and hence, exhibit the stiffest behavior. The elastase treated PCLS which lack the structural support of the EF and the FF show a softer mechanical behavior. The PCLS treated with collagenase are even softer than the elastase treated specimens. The PCLS treated with both enzymes show the softest behavior. Another interesting fact is that the stress-strain curves of the PCLS treated with collagenase have a reduced curvature. This agrees with the study of Haut and Little (1972), who showed that the CF exhibit strongly non-linear material behavior.

A comparison with the results found in the literature is essentially impossible, since the only paper presenting relevant results (Yuan et al., 2000) provided only two static stress-strain curves; these curves additionally showed a variation of over 100 % between each other. However, the general trend, meaning the shape of the curve, the order of magnitude and the behavior after collagenase/elastase treatment is similar.

Other interesting aspects are: the contribution of the FF is always more dominant than the contribution of the EF; for small strains. the FF is stiffer than the CF as well as the EF. This can be explained with the CF not being fully extended, i.e. their waviness can potentially inhibit their own extension as well as the extension of the EF.

Due to these findings, the material law presented in the following section will not only account for the three major load-bearing constituents but also include an additional summand representing the FF. In order not to get too much influence of intersubject variability, the material model is fitted to the averaged curves rather than to the individually determined curves, see Figure 6.18.

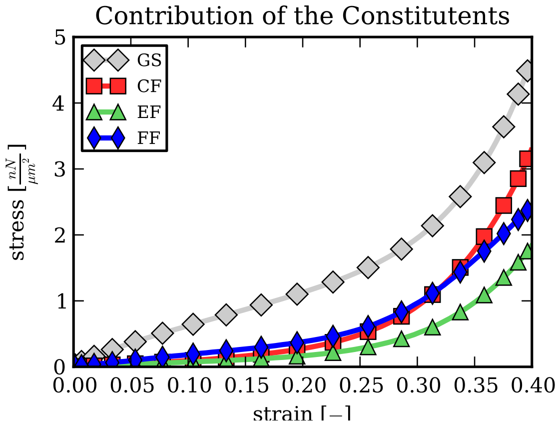

Figure 6.18: Averaged stress-strain curves for each of the four load-bearing constituents. GS: ground substance; CF: collagen fibers EF: elastin fibers and FF: fiber-fiber interaction.

6.4 Conclusion

Living PCLS of isolated rat lungs are experimentally investigated via uni-axial tension tests. Compared with previous experimental methods found in literature (Jamal et al., 2001; Yuan et al., 2000; Fukaya et al., 1968; Mijailovich et al., 1994; Sugihara et al., 1971; Vawter et al., 1978; Hoppin et al., 1975; Gao et al., 2006), the experimental protocol developed in this work has three major advantages. First, the slice dimensions are reproducible, second, several specimens, dissected from one animal, can be tested and third, the specimens are still viable during testing.

In addition, with this study a measure of the contribution arising from fiber-fiber interaction (FF) has been provided for the first time. Previously, Mijailovich et al. (1993) presented a very simplified model, based on two isolated fibers, for the FF. However, they did not quantify the influence. The quantification is very important because it turned out that the FF contribution is larger than the contribution of the elastin fibers themselves, i.e. the interaction of the constituents is as important as the classification of the constituents themselves. This finding is consistent with the observations of Mercer and Crapo (1990).

However, to get a better understanding of the processes occurring during FF, dynamic scanning methods will be essential in the future. Another interesting point is the interaction between the GS and the fiber families. Unfortunately, due to the fact that the GS consists of a plethora of different components, this contribution cannot be determined individually. In the presented model the contribution of this interaction is included in the SEFs of the fiber families.

7 Material Identification

In this chapter, a sophisticated material model adequately reproducing the experimental results presented in chapter 6 is derived. Since the optimal constitutive model is not known *a priori,* this study is not limited to the optimization of one predetermined SEF, but rather compares several possible SEFs, which will be referred to as *"*potential SEF*"* in the latter. For this reason, a *material toolbox* is implemented in the research-code BACI. This material toolbox allows implemented SEFs to be arbitrarily combined. For each of these "potential SEFs", the individual material parameters are optimized to fit the experimentally determined behavior. For the parameter optimization, an inverse analysis is performed. The corresponding algorithm is also included in BACI. In the last step, the "potential SEFs" are compared with each other, in order to obtain the optimal description of the experimental material behavior.

7.1 Methodology

This section is divided in four subsections. The first one introduces the material toolbox and the included SEFs. The second one describes the utilized FE model. The third one describes the inverse analysis algorithm, i.e. the parameter optimization for the "potential SEFs". The fourth one describes the comparison between the different "potential SEFs" for the homogenized as well as for the constituent-based material model.

7.1.1 Material Toolbox

Due to the fact that a SEF can be composed of additive summands (Balzani, 2006), a material toolbox has been implemented in the research-code BACI. In the following, Ψ will replace Ψ_v, for simplicity. Each SEF can be defined as the sum of its individual summands implemented in the toolbox, i.e.

$$\Psi_\mathrm{total} = \sum \Psi_\mathrm{summand}. \tag{7.1.1}$$

This toolbox has several advantages: first, the implementation of new material models is simplified, since only the respective coefficients δ, see section 3.2, have to be adjusted. Second, material models can be adjusted, e.g. by adding new summands, without having to implement a new material formulation. Third, the individual summands can be arbitrarily combined and recombined, thereby allowing an easy comparison between several "potential SEFs".

In the following, a short overview of the implemented SEF summands is given, starting with coupled SEF summands, before introducing decoupled isochoric and volumetric SEF summands. It is worth noting that each part of the SEFs fulfills the principles of objectivity, material symmetry, the requirements of polyconvexity and has a stress–free reference state.

7.1.1.1 Coupled Strain Energy Density Functions

The two implemented, coupled SEFs are established functions which can be frequently found in literature. These SEFs have been developed to describe the material behavior of compressible, foam-like structures such as polyurethane foams.

The first coupled SEF introduced by Blatz and Ko (1962) for foam-like elastomeres reads

$$\Psi_{\text{blako}} = f\frac{G}{2}\left[(I_1 - 3) + \frac{1}{\beta}(J^{-2\beta} - 1)\right] + (1-f)\frac{G}{2}\left[\left(\frac{I_2}{J^2} - 3\right) + \frac{1}{\beta}(J^{2\beta} - 1)\right] \tag{7.1.2}$$

with G and ν denoting the shear modulus and Poisson's ratio, respectively, $\beta = \nu - 0.5$ denoting a material parameter, and $f \in [0,1]$ being an interpolation parameter. For the definition of the constants see Appendix A.2.4 and A.2.3.

The second coupled SEF is the compressible Neo-Hookean formulation

$$\Psi_{\text{neo}} = \frac{G}{2}(I_1 - 3) - G\ln J + \frac{\lambda}{2}(\ln J)^2 \tag{7.1.3}$$

where λ and G are respectively, the first and the second Lamé's parameter, as suggested by Bonet and Wood (1997). For the definition of the constants see Appendix A.2.3 and A.2.5.

7.1.1.2 Decoupled Strain Energy Density Functions

As mentioned in section 3.2.2, decoupled SEFs are additively split into a volumetric Ψ_{vol} and an isochoric part Ψ_{iso}. For each part, different summands have been implemented, which will be introduced in the following.

Isochoric Strain Energy Density Functions There are several possibilities for the isochoric summands Ψ_{iso} of the SEF. For this work we have chosen a subset of the most commonly used SEFs in literature. The simplest one is the isochoric part of the Neo-Hookean formulation

$$\Psi_{\text{iso, neo}} = c\left(\bar{I}_1 - 3\right) \tag{7.1.4}$$

where $c > 0$ represents a stress–like parameter. Slightly more complicated is the formulation suggested by Yeoh (1993)

$$\Psi_{\text{iso, yeoh}} = c_{\text{yeoh, 1}}(\bar{I}_1 - 3) + c_{\text{yeoh, 2}}(\bar{I}_1 - 3)^2 + c_{\text{yeoh, 3}}(\bar{I}_1 - 3)^3 \tag{7.1.5}$$

where $c_{\text{yeoh, 1}} > 0$, $c_{\text{yeoh, 2}} > 0$ and $c_{\text{yeoh, 3}} > 0$ are stress-like parameters. For convenience, this formulation is split up into a linear (which equals $\Psi_{\text{iso, neo}}$) $\Psi_{\text{iso, lin}}$, quadratic $\Psi_{\text{iso, quad}}$, and cubic part $\Psi_{\text{iso, cub}}$, i.e.

$$\Psi_{\text{iso, lin}} = c_{\text{lin}}(\bar{I}_1 - 3), \quad \Psi_{\text{iso, quad}} = c_{\text{quad}}(\bar{I}_1 - 3)^2, \quad \Psi_{\text{iso, cub}} = c_{\text{cub}}(\bar{I}_1 - 3)^3 \tag{7.1.6}$$

where $c_{\text{lin}} > 0$, $c_{\text{quad}} > 0$ and $c_{\text{cub}} > 0$ are stress-like parameters. It should be mentioned that "linear" here only refers to the expression in parenthesis being linear and not to a linear constitutive model.

Additionally, the following power functions have been implemented

$$\Psi_{\text{iso, pow4}} = c_{\text{pow4}}(\bar{I}_1 - 3)^4, \tag{7.1.7}$$

$$\Psi_{\text{iso, pow5}} = c_{\text{pow5}}(\bar{I}_1 - 3)^5, \tag{7.1.8}$$

$$\Psi_{\text{iso, pow6}} = c_{\text{pow6}}(\bar{I}_1 - 3)^6, \text{ and} \tag{7.1.9}$$

$$\Psi_{\text{iso, pow7}} = c_{\text{pow7}}(\bar{I}_1 - 3)^7 \tag{7.1.10}$$

where $c_{\text{pow4}} > 0$, $c_{\text{pow5}} > 0$, $c_{\text{pow6}} > 0$ and $c_{\text{pow7}} > 0$ are stress-like parameters. These SEFs were chosen because, due to their simplicity, they are well suited for the purpose of combining several summands. Additionally, SEFs which are commenly used for soft biological tissue shall be investigated. An exponential expression

$$\Psi_{\text{iso, exp}} = \frac{c_{\text{exp, 1}}}{2c_{\text{exp, 2}}}\left[\exp\left[c_{\text{exp, 2}}\left(\frac{1}{3}\bar{I}_1 - 1\right)^2\right] - 1\right] \tag{7.1.11}$$

which has been implemented with $c_{\text{exp, 1}} \geq 0$ being a stress-like parameter and $c_{\text{exp, 2}} > 0$

being a dimensionless parameter, that can be found in slightly different form in Delfino et al. (1997).

Finally the Mooney-Rivlin SEF

$$\Psi_{\text{iso, mori}} = c_{\text{mori, }1}(\bar{I}_1 - 3) + c_{\text{mori, }2}(\bar{I}_2 - 3) \tag{7.1.12}$$

where $c_{\text{mori, }1} > 0$ and $c_{\text{mori, }2} > 0$ are stress-like parameters.

Volumetric Strain Energy Density Functions In the literature, many different formulations for Ψ_{vol} can be found, for a detailed comparison see (Doll and Schweizerhof, 2000). However for convenience the focus in this work is on the three most common ones.

The first one suggested by Ogden (1974) is defined as

$$\Psi_{\text{vol, ogd}} = \frac{\kappa}{4}(-2\ln J + J^2 - 1) \tag{7.1.13}$$

withκ being the bulk modulus. The volumetric Ogden SEF $\Psi_{\text{vol, ogd}}$ is chosen, because it is suitable for compressible materials.

Another option suggested by Balzani et al. (2006) is defined as

$$\Psi_{\text{vol, pen}} = \epsilon\left(J^\gamma + \frac{1}{J^\gamma} - 2\right) \tag{7.1.14}$$

where ϵ is a stress-like parameter and γ is a dimensionless parameters.

The third option is the SEF suggested by Sussman and Bathe (1987)

$$\Psi_{\text{vol, suba}} = \frac{\kappa}{2}(J - 1)^2, \tag{7.1.15}$$

with κ being the bulk modulus.

7.1.2 Finite Element Model

To find the optimal material description for lung parenchyma, an inverse analysis is performed see section 7.1.3. For this purpose previously described experiments, see chapter 6, are simulated utilizing the FEM.

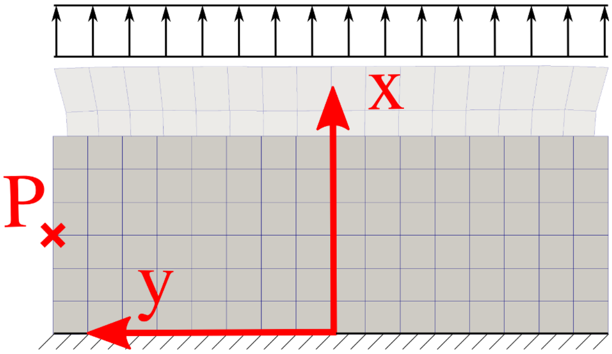

Figure 7.1: Simulation of uniaxial tensile test of a precision-cut lung slice (PCLS). The lower clamp is simulated with a Dirichlet boundary condition and the upper clamp with a Neumann and a Dirichlet boundary condition. The x-displacements at the top of the specimen, which equals the displacement of the second clamp and the y-displacement at point P are recorded as target for the material optimization.

The tested specimen, with the dimensions $7.0 \times 2.5 \times 0.5\,\mathrm{mm}$, is discretized with 288 linear hexahedral elements, see Figure 7.1. For the simulation, the following boundary conditions are chosen:

- The resting clamp is represented with a Dirichlet boundary condition. All displacement degrees of freedom (dofs) of the nodes with x=0, are set to zero.
- The moving clamp during the experiment is represented with a combination of Neumann and Dirichlet boundary conditions. All displacement dofs in y- and z- direction are set to zero and the experimentally determined stresses are applied in x-direction.

According to Tschanz et al. (2003), the tissue consists of 80.4% air. The alveolar wall contains mainly water with the density $\rho_w = 1.0\,\mathrm{kg/dm^3}$. Hence, the parenchymal density used in the simulation was chosen to be $\rho_{\text{par}} = (1-0.804)\,\mathrm{kg/dm^3} = 0.196\,\mathrm{kg/dm^3}$.

7.1.3 Inverse Analysis

For each "potential SEF" the material parameters $\mathbf{p}$ can be written in the general vector form

$$\mathbf{p} = [p_i, ..., p_k]^T, \tag{7.1.16}$$

with k being the number of material parameters. To determine optimal parameters $\mathbf{p}$, an inverse analysis is performed (see Figure 7.2). For example, for the "potential SEF" $\Psi_{\text{ex}} = \Psi_{\text{iso, yeoh}} + \Psi_{\text{vol, ogd}} = c_{\text{yeoh, 1}}(\bar{I}_1 - 3) + c_{\text{yeoh, 2}}(\bar{I}_1 - 3)^2 + c_{\text{yeoh, 3}}(\bar{I}_1 - 3)^3 + \frac{\kappa}{4}(-2\ln J + J^2 - 1)$ the parameters $\mathbf{p}_{\text{ex}} = [c_{\text{yeoh, 1}}, c_{\text{yeoh, 2}}, c_{\text{yeoh, 3}}, \kappa]^T$ would be optimized.

Beginning with an initial guess of the material parameters $\mathbf{p}_0$, the following displacements are calculated and compared to those obtained from the experiment:

- the displacement in x-direction u_x of the moving clamp and
- the displacements in y-direction u_y at point P as measure of the lateral contraction of the specimen.

The displacements $\mathbf{u}_i = \left[u_x, u_y\right]_i^T$ are calculated at each time step i, leading to the displacement vector

$$\mathbf{u} = \begin{bmatrix} \mathbf{u}_1 \\ \vdots \\ \mathbf{u}_n \end{bmatrix} = \begin{bmatrix} \left[u_x, u_y\right]_1^T \\ \vdots \\ \left[u_x, u_y\right]_n^T \end{bmatrix}, \tag{7.1.17}$$

where n denotes the number of time steps.

The residual vector $\mathbf{r}$ is defined as the difference between calculated and experimentally determined displacements

$$\mathbf{r} = \begin{bmatrix} r_1 \\ \vdots \\ r_{2n} \end{bmatrix} = \begin{bmatrix} u_{x,1,\mathrm{cal}} - u_{x,1,\mathrm{exp}} \\ u_{y,1,\mathrm{cal}} - u_{y,1,\mathrm{exp}} \\ \vdots \\ u_{x,i,\mathrm{cal}} - u_{x,i,\mathrm{exp}} \\ u_{y,i,\mathrm{cal}} - u_{y,i,\mathrm{exp}} \\ \vdots \\ u_{x,n,\mathrm{cal}} - u_{x,n,\mathrm{exp}} \\ u_{y,n,\mathrm{cal}} - u_{y,n,\mathrm{exp}} \end{bmatrix}. \tag{7.1.18}$$

To minimize the target function

$$T(\mathbf{p}) = \sum_{i=1}^{2n} \left(r_i(\mathbf{p}) \cdot r_i(\mathbf{p})\right), \tag{7.1.19}$$

the procedure developed by Levenberg (1944) and Marquardt (1963), the so-called Levenberg–Marquardt algorithm, is used. Briefly, in order to determine the minimum the root of the gradient vector $\mathbf{g}$ being the derivative of the target function T with respect to the parameters $\mathbf{p}$

$$\mathbf{g} := \frac{\partial T(\mathbf{p})}{\partial \mathbf{p}}, \tag{7.1.20}$$

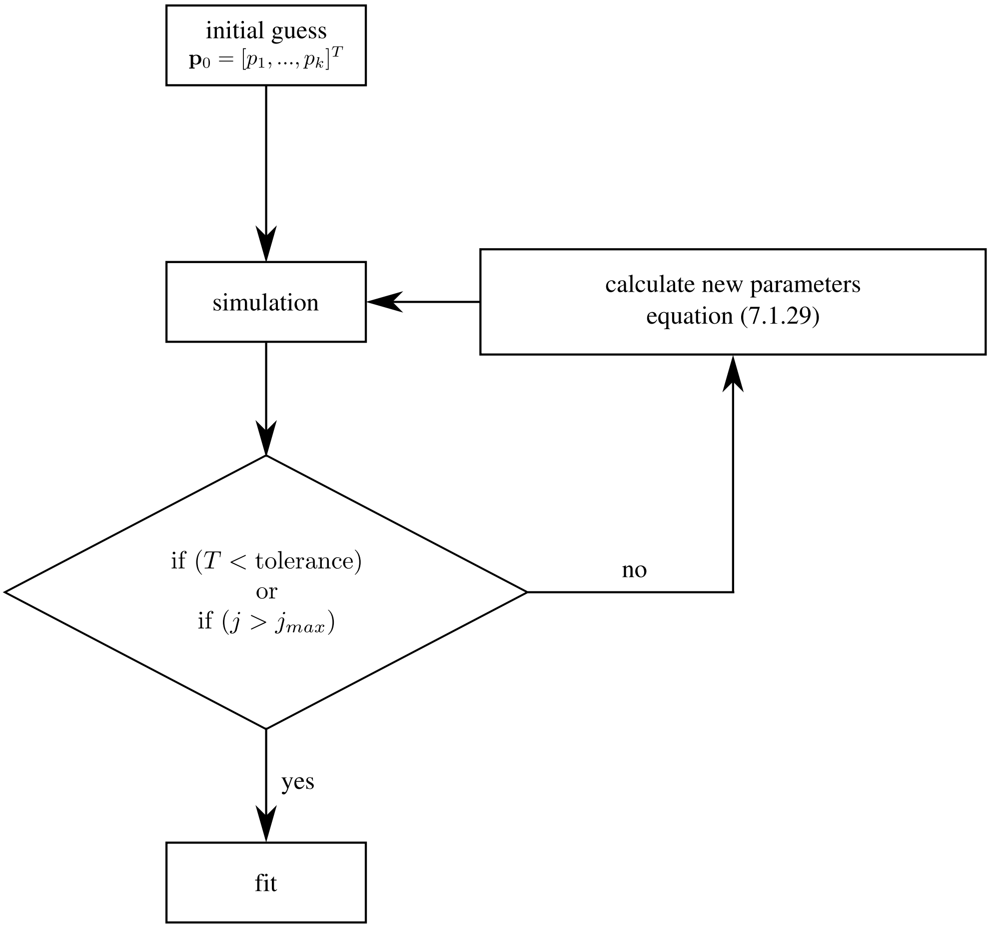

Figure 7.2: Flow chart of the inverse analysis to determine the optimal set of material parameters for each "potential SEF". Starting with an initial guess of material parameters $\mathbf{p}_0$, a finite element simulation mimicking the experiment is performed. The target function T is calculated from the experimentally and numerically determined displacements. If the target function T is larger than a given tolerance and the maximal number of iterations $j_{\max}$ is not reached yet, a new set of material parameters $\mathbf{p}_{i+1}$ is calculated utilizing the Levenberg-Marquardt algorithm, see equation (7.1.30), and the simulation is performed again. If the target function T is smaller than the tolerance or the maximal number of iterations $j_{\max}$ is reached, the procedure is aborted and the optimal fit is obtained.

need to be determined. The individual components of the gradient vector **g** are calculated as

$$g_l = 2\sum_{i=1}^{2n} r_i \frac{\partial r_i}{\partial p_l}. \tag{7.1.21}$$

The Hessian matrix **H** is the second derivation of the target function T with respect to the parameters **p**

$$\mathbf{H} := \frac{\partial^2 T(\mathbf{p})}{(\partial \mathbf{p})^2}. \tag{7.1.22}$$

The individual components of the Hessian matrix **H** are calculated as

$$H_{kl} = 2\sum_{i=1}^{2n}\left(\frac{\partial r_i}{\partial p_k}\frac{\partial r_i}{\partial p_l} + r_i \frac{\partial^2 r_i}{\partial p_k \partial p_l}\right). \tag{7.1.23}$$

In order to solve the non-linear problem

$$\mathbf{g}(\mathbf{p}) \overset{!}{=} \mathbf{0} \tag{7.1.24}$$

the problems is linearized and iteratively solved using the well-known Newton's method (also called Newton-Raphson method). The approximation $\mathbf{p}_{j+1}$ is calculated from $\mathbf{p}_j$ as

$$\mathbf{p}_{j+1} = \mathbf{p}_j - \mathbf{H}^{-1}\mathbf{g}. \tag{7.1.25}$$

For the Gauss-Newton method the second-order derivative terms are ignored, leading to the approximation of the Hessian matrix of

$$H_{kl} \approx \tilde{H}_{kl} = 2\sum_{i=1}^{2n}\left(\frac{\partial r_i}{\partial p_k}\frac{\partial r_i}{\partial p_l}\right). \tag{7.1.26}$$

Introducing the Jacobian-matrix as

$$\mathbf{J_r} = \left[\frac{\partial r_i}{\partial p_j}\right] = \begin{bmatrix} \frac{\partial r_1}{\partial p_1} & \cdots & \frac{\partial r_1}{\partial p_k} \\ \vdots & & \vdots \\ \frac{\partial r_{2n}}{\partial p_1} & \cdots & \frac{\partial r_{2n}}{\partial p_k} \end{bmatrix}, \tag{7.1.27}$$

the gradient vector **g** and the approximate Hessian matrix $\tilde{\mathbf{H}}$ can be written as

$$\mathbf{g} = 2\mathbf{J_r}^T\mathbf{r}, \quad \tilde{\mathbf{H}} = 2\mathbf{J_r}^T\mathbf{J_r}. \tag{7.1.28}$$

Substituting this in the recurrence equation (7.1.25) yields

$$\mathbf{p}_{j+1} = \mathbf{p}_j - \left(\mathbf{J_r}^T\mathbf{J_r}\right)^{-1}\mathbf{J_r}^T\mathbf{r} \tag{7.1.29}$$

which is known as the Gauss-Newton procedure. This methodology can be further improved by introducing a damped version, the Levenberg–Marquardt algorithm

$$\mathbf{p}_{j+1} = \mathbf{p}_j - \left(\mathbf{J_r}^T\mathbf{J_r} + \lambda\,\mathrm{diag}\left(\mathbf{J_r}^T\mathbf{J_r}\right)\right)^{-1}\mathbf{J_r}^T\mathbf{r}, \tag{7.1.30}$$

with λ being a damping factor that is adjusted at each iteration j. For a fast reduction of the target function T a small damping factor λ brings the algorithm closer to the Gauss-Newton method, whereas a larger damping factor λ brings the algorithm closer to the gradient descent direction. The damping factor λ factor is initially set to 1.0 and adapted with the help of the relative error, such that $\lambda = \lambda_{\mathrm{old}}\frac{T}{T_{\mathrm{old}}}$, with λ_{old} and T_{old} being the damping factor and the target function of the last iteration, respectivly. The loop of simulation and the calculation of a new set of material parameters terminates once maximal number of iterations $j_{\max}$ is reached. For the optimization, presented in this study, the maximal number of iterations $j_{\max}$ is chosen to be 25, since preliminary studies have shown that by then the target function T has converged to a constant value. Furthermore the stop criteria of a predefined tolerance turned out to be contra productive for the comparison of the quality of fit for the “potential SEFs”.

For a better comparison of the error, a normalized form of the target function is used, i.e.

$$T_n = \frac{1}{L}\sqrt{\frac{T}{2n}} = \frac{1}{L}\sqrt{\frac{\sum_{i=1}^{2n}(r_i(\mathbf{p})\cdot r_i(\mathbf{p}))}{2n}}. \tag{7.1.31}$$

This algorithm has already shown good results for soft biological tissue (Kauer et al., 2002; Mahnken and Stein, 1996; Moulton et al., 1995; Seshaiyer and Humphrey, 2003). However, one common drawback of most optimization algorithms is that it might only converge to a local minimum instead of a global minimum. Therefore, in a preliminary study, the parameter optimization was performed with several randomly picked initial guesses of **p**. For example, for the coupled SEF Ψ_{blako}, the initial values were chosen in the range of

$G = 5 \ldots 20$ and $\nu = 0.01 \ldots 0.49$. The result of the optimization procedure was similar in all six tested cases, yielding $G = 8.778 \pm 0.01535$ and $\nu = 0.32944 \pm 0.00156$. Over 90 % of initial guesses converged to the same solution with a minimal error and 10 % to a different solution with a higher error.

This methodology has the advantage that the same deformation and loading state are produced in the simulation as in the experiment. This means, there is no need for additional assumption, like a state of uniaxial tension, a plain stress or strain state. This leads to a globally applicable material model.

7.1.4 Strain Energy Density Function Comparison

In order to evaluate the suitability of a material model, both minimization of the target function T and limitation of the number of material parameters is of interest. Therefore, to compare the fitted “potential SEFs”, a variation of the Bayesian information criterion (BIC) (Hastie et al., 2009) is chosen. This criterion is a measure of the quality of the fit including the number of model parameters k. It is given by

$$\mathrm{BIC} = \log\left(\frac{T}{2n}\right) + \frac{k}{2n}\log(2n). \tag{7.1.32}$$

7.2 Results

7.2.1 Homogenized Lung Parenchyma Model

To obtain an optimal material model for lung parenchymal tissue different coupled and decoupled SEFs are compared. First, the suitability of the two coupled SEFs given in equation (7.1.2) and (7.1.3), is investigated. As a next step, several combinations of the isochoric SEFs Ψ_{iso} in combination with the volumetric Ogden SEF $\Psi_{\mathrm{vol,\,ogd}}$ are investigated. Thus, the comparison is not restricted to “potential SEFs” presented in literature but also new recombinations of their summands are tested. Finally, the influence of the three suggested volumetric SEFs Ψ_{vol} is investigated in combination with determined the best fit for the isochoric SEF Ψ_{iso}.

Coupled Strain Energy Density Functions As can be seen in Figure 7.3 and Tab. 7.1, the coupled SEFs (Ψ_{blako} and Ψ_{neo}) are not able to reproduce the material behavior of lung parenchyma in an adequate way. The normalised target function T_n did not converge towards a comparable low value as for the decoupled SEFs.

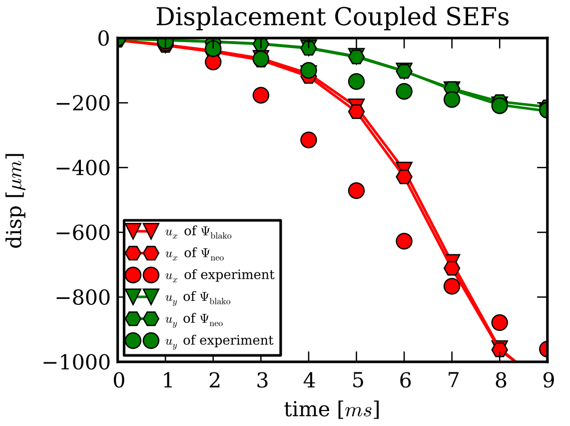

Figure 7.3: Comparison of the parameter optimization of potential coupled strain energy density functions (SEFs). Comparison between experiment and simulations for the optimal parameter set. The displacements u_x and u_y are given in red and green, respectively.

Decoupled Strain Energy Density Functions As the next step, combinations of isochoric SEFs ($\Psi_{\text{iso, neo}}$, $\Psi_{\text{iso, neo}} + \Psi_{\text{iso, exp}}$, $\Psi_{\text{iso, yeoh}}$ and $\Psi_{\text{iso, mori}}$) with the volumetric Ogden SEF $\Psi_{\text{vol, ogd}}$ are investigated. Due to their higher order terms both $\Psi_{\text{iso, neo}} + \Psi_{\text{iso, exp}}$ and $\Psi_{\text{iso, yeoh}}$ reproduce the stiffening of the parenchymal slice better than $\Psi_{\text{iso, neo}}$ and $\Psi_{\text{iso, mori}}$. The combination of $\Psi_{\text{iso, yeoh}}$ and $\Psi_{\text{vol, ogd}}$ is the optimal fit in this comparison, as it is able to reproduce both u_x and u_y (Figure 7.4 and Table 7.1).

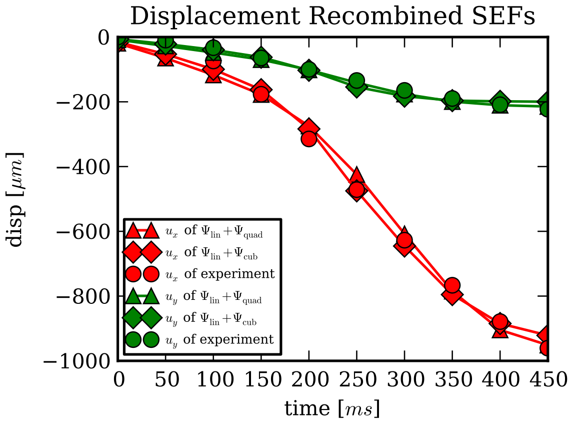

Figure 7.5: Comparison of the parameter optimization of potential recombined strain energy density functions (SEFs). Comparison between experiment and simulations for the optimal parameter set. The displacements u_x and u_y are given in red and green, respectively.

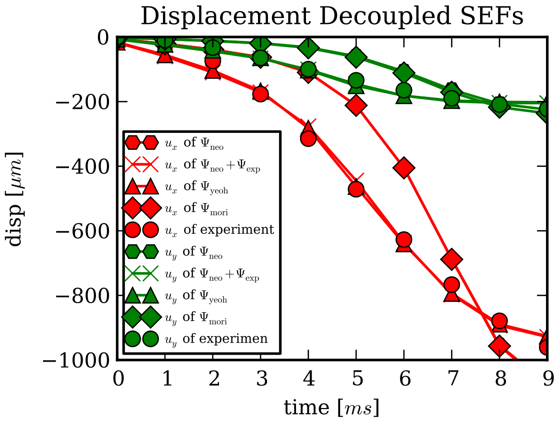

Figure 7.4: Comparison of the parameter optimization of potential decoupled strain energy density functions (SEFs). Comparison between experiment and simulations for the optimal parameter set. The displacements u_x and u_y are given in red and green, respectively. For sake of clarity, not all curves are shown.

The SEFs investigated so far consist of individual summands. For example the isochoric SEF suggested by Yeoh (1993) $\Psi_{\text{iso, yeoh}}$. However, it is unclear whether all summands are needed for an adequate fit and whether another combination of SEFs summands would produce a better fit. Therefore different recombinations of the individual summands are investigated. Most of the SEFs show a good fit to the experimental results (Figure 7.5 and Tab. 7.1). For clarity, not all tested combinations are shown. Of all tested alternatives, the combinations $\Psi_{\text{iso, lin}} + \Psi_{\text{iso, quad}} + \Psi_{\text{iso, cub}}$, $\Psi_{\text{iso, mori}} + \Psi_{\text{iso, quad}} + \Psi_{\text{iso, cub}}$ and $\Psi_{\text{iso, lin}} + \Psi_{\text{iso, cub}}$ were found to have the smallest target function T. This implies that neither the quadratic summand, nor the Mooney-Rivlin summand, including $\bar{I}_2$, improves the fit.

Figure 7.6 shows the BIC comparison of all “potential SEFs”. The combination $\Psi_{\text{iso, lin}} + \Psi_{\text{iso, cub}}$ has the lowest BIC which implies the best fit.

Volumetric Strain Energy Density Functions Finally, the influence of different volumetric contributions to the overall fit is investigated. It is immediately evident that the volumetric part has very little influence on the overall error (see Figure 7.7), however, the convergence behavior is affected by the choice. The fastest rate of convergence is obtained with the volumetric Ogden SEF $\Psi_{\text{vol, ogd}}$. Moreover, this part also turns out to be the most robust one during the simulations.

Optimal Material Model The comparison of SEFs can be found in Table 7.1 and Figure 7.6. Based on the investigations discussed before, the optimal material model for lung parenchyma is found to be

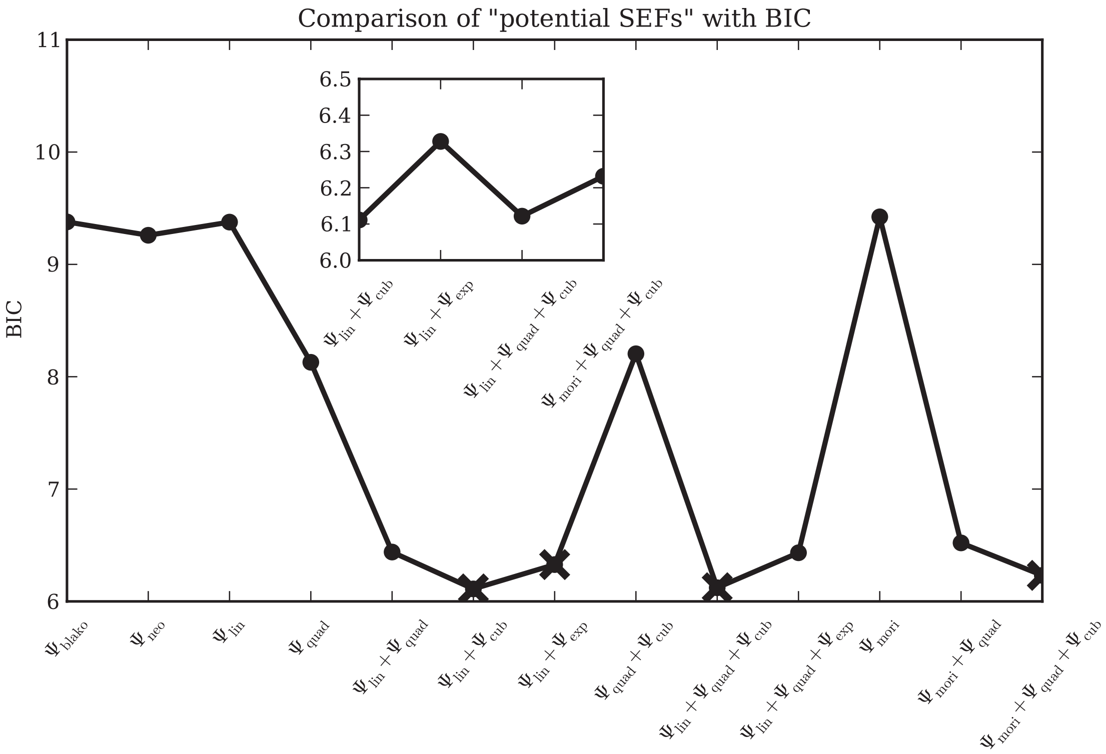

Figure 7.6: Comparison of selected “potential SEFs” based on the Bayesian information criterion (BIC). The crosses indicate the four “potential SEFs” with the lowest BIC. A detailed comparison between those four “potential SEFs” can be found in the zoomed window.

$$\begin{aligned} \Psi_{\mathrm{par}}\left(\bar{I}_1, J\right) &= \Psi_{\mathrm{iso,\,lin}}\left(\bar{I}_1\right) + \Psi_{\mathrm{iso,\,cub}}\left(\bar{I}_1\right) + \Psi_{\mathrm{vol,\,ogd}}(J) \\ &= c_{\mathrm{lin}}\left(\bar{I}_1 - 3\right) + c_{\mathrm{cub}}\left(\bar{I}_1 - 3\right) + \frac{\kappa}{4}\left(-2\ln J + J^2 - 1\right) \end{aligned} \tag{7.2.1}$$

with the material parameters $c_{\mathrm{lin}} = 1.78\mathrm{kPa}$, $c_{\mathrm{cub}} = 18.10\mathrm{kPa}$, and $\kappa = 44.39\mathrm{kPa}$.

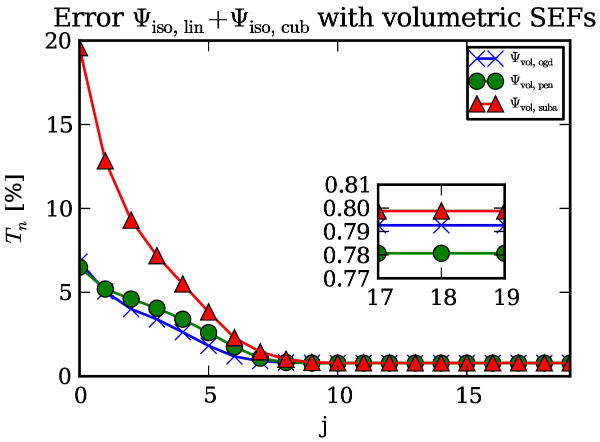

Figure 7.7: Comparison of volumetric strain energy density functions (SEFs). Although the three tested volumetric SEFs Ψ_{vol} showed rather similar results, the volumetric Ogden SEF $\Psi_{\text{vol, ogd}}$ is robuster within the simulation and the error decreases faster during the optimization process. The zoom window shows that the differences of the target function T_n between the three volumetric SEFs Ψ_{vol} in the converged state is marginal.

7.2.2 Constituent-Based Lung Parenchyma Model

Although the material model derived in the previous section reliably describes the material behavior of lung parenchyma it is a purely phenomenological description: To assess the individual contributions of the load-bearing constituents, a constituent-based model will be derived in the following. For this purpose the SEF is split up into four individual parts, representing the load-bearing constituents of the lung parenchyma. The SEF reads

$$\Psi_{\text{v}}(\mathbf{C}) = \Psi_{\text{CF}}\left(\bar{I}_1,\bar{I}_2\right)+\Psi_{\text{EF}}\left(\bar{I}_1,\bar{I}_2\right)+\Psi_{\text{FF}}\left(\bar{I}_1,\bar{I}_2\right)+\Psi_{\text{GS}}\left(\bar{I}_1,\bar{I}_2,J\right) \tag{7.2.2}$$

where Ψ_{CF} represents the contribution of the CF, Ψ_{EF} represents the contribution of the EF, Ψ_{FF} represents the contribution of the FF, and Ψ_{GS} represents the rest of the tissue constituents, including the air-spaces. Since the fibers themselves and their interaction do not contribute to the volume change, the corresponding SEFs only depend on the modified first invariant $\bar{I}_1$ and second invariant $\bar{I}_2$. For the isochoric parts of the SEFs Ψ_{iso} several "potential SEFs" are investigated. For the volumetric part $\Psi_{\text{vol, ogd}}$ is chosen, based on the results of section 7.2.1.

Table 7.1: Comparison of the normalized target function T_n of optimized “potential SEFs”.

Type of SEF	“potential SEF”	T_n
Coupled SEFs	Ψ_{blako}	4.05
	Ψ_{neo}	3.84
Decoupled SEFs	$\Psi_{\text{iso, lin}} + \Psi_{\text{vol, ogd}}$	4.15
	$\Psi_{\text{iso, lin}} + \Psi_{\text{iso, exp}} + \Psi_{\text{vol, ogd}}$	0.86
	$\Psi_{\text{iso, yeoh}} + \Psi_{\text{vol, ogd}}$	0.78
	$\Psi_{\text{iso, mori}} + \Psi_{\text{vol, ogd}}$	4.15
Recombinations of SEF summands	$\Psi_{\text{iso, lin}} + \Psi_{\text{iso, quad}} + \Psi_{\text{vol, ogd}}$	0.93
	$\Psi_{\text{iso, lin}} + \Psi_{\text{iso, quad}} + \Psi_{\text{iso, exp}} + \Psi_{\text{vol, ogd}}$	0.89
	$\Psi_{\text{iso, lin}} + \Psi_{\text{iso, cub}} + \Psi_{\text{vol, ogd}}$	0.79
	$\Psi_{\text{iso, quad}} + \Psi_{\text{vol, ogd}}$	2.22
	$\Psi_{\text{iso, quad}} + \Psi_{\text{iso, cub}} + \Psi_{\text{vol, ogd}}$	2.26
	$\Psi_{\text{iso, mori}} + \Psi_{\text{iso, quad}} + \Psi_{\text{vol, ogd}}$	0.95
	$\Psi_{\text{iso, mori}} + \Psi_{\text{iso, quad}} + \Psi_{\text{iso, cub}} + \Psi_{\text{vol, ogd}}$	0.80

7.2.2.1 Contribution of the Individual Constituents

For each of the three tissue constituents, i.e. CF (Ψ_{CF}), EF (Ψ_{EF}), GS (Ψ_{GS}), and FF (Ψ_{FF}) an individual material description (combination of SEFs) is determined. Due to fact that neither the fibers, nor their interaction influence the volumetric deformation of the tissue, their SEFs can only be determined in combination with the contribution of the GS, i.e. Ψ_{GS}. For this reason, Ψ_{GS} and the corresponding material parameters are determined. Subsequently, the other two constituents (CF and EF) and the FF are determined, as a combination of Ψ_{GS} and Ψ_{CF}, Ψ_{EF}, or Ψ_{FF}, respectively, are determined. The input stress-strain curves for the different constituents are shown in Figure 7.8 (cf. chapter (6)).

The BIC comparison of the “potential SEFs” is shown in Figure 7.9. It turns out, that the combination of $\Psi_{\text{iso, lin}} + \Psi_{\text{iso, pow5}}$ is the best fit for GS, CF, and EF, whereas $\Psi_{\text{iso, lin}} + \Psi_{\text{iso, pow4}}$ shows the best agreement for FF. The errors and according material parameters are shown in Table 7.3. The material constants of the EF are the lowest ones, which correlates to the fact that the calculated stress-strain curve for the EF is the most compliant, see Figure 7.8.

Hence, the optimal constituent-based material description of homogenized lung parenchyma is given by

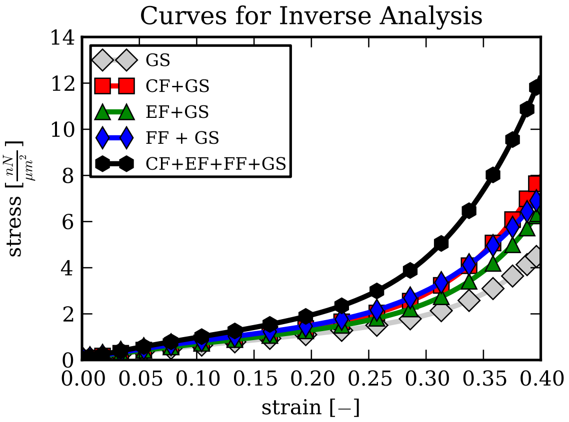

Figure 7.8: Curves used for the inverse analysis to determine the contribution of the four individual constituent. GS: ground substance; CF: collagen fibers; EF: elastin fibers; FF: fiber-fiber interaction.

Table 7.3: Comparison of four different strain energy density function (SEF) combinations for the isochoric part Ψ_{iso}.

SEF	SEF terms	BIC	T_n	c_{lin}	c_{pow4}	c_{pow5}	κ
Ψ_{GS}	$\Psi_{\text{iso, lin}} + \Psi_{\text{iso, pow5}}$	6.43	0.93	1.629		$1.740 \cdot 10^2$	8.946
Ψ_{CF}	$\Psi_{\text{iso, lin}} + \Psi_{\text{iso, pow5}}$	7.38	1.53	0.565		$1.186 \cdot 10^3$	
Ψ_{EF}	$\Psi_{\text{iso, lin}} + \Psi_{\text{iso, pow5}}$	6.84	1.17	0.342		$4.503 \cdot 10^2$	
Ψ_{FF}	$\Psi_{\text{iso, lin}} + \Psi_{\text{iso, pow4}}$	7.22	1.41	0.789	$1.458 \cdot 10^2$		

$$\Psi_{\text{par}} = \Psi_{\text{CF}} + \Psi_{\text{EF}} + \Psi_{\text{FF}} + \Psi_{\text{GS}} \tag{7.2.3}$$

with

$$\Psi_{\text{CF}} = 0.565\left(\bar{I}_1 - 3\right) + 1.186 \cdot 10^3 \left(\bar{I}_1 - 3\right)^5, \tag{7.2.4}$$

$$\Psi_{\text{EF}} = 0.342\left(\bar{I}_1 - 3\right) + 4.503 \cdot 10^2 \left(\bar{I}_1 - 3\right)^5, \tag{7.2.5}$$

$$\Psi_{\text{FF}} = 0.789\left(\bar{I}_1 - 3\right) + 1.458 \cdot 10^2 \left(\bar{I}_1 - 3\right)^4, \text{ and} \tag{7.2.6}$$

$$\Psi_{\text{GS}} = 1.629\left(\bar{I}_1 - 3\right) + 1.740 \cdot 10^2 \left(\bar{I}_1 - 3\right)^5 + \frac{8.946}{4}\left(-2\ln J + J^2 - 1\right). \tag{7.2.7}$$

At small strains the GS shows the stiffest behavior, this can also be seen in the material parameters, since c_{lin} is more than twice as high for the GS than for CF, EF or FF. This means that at small strains the GS dominates the material behavior, whereas at larger strains the

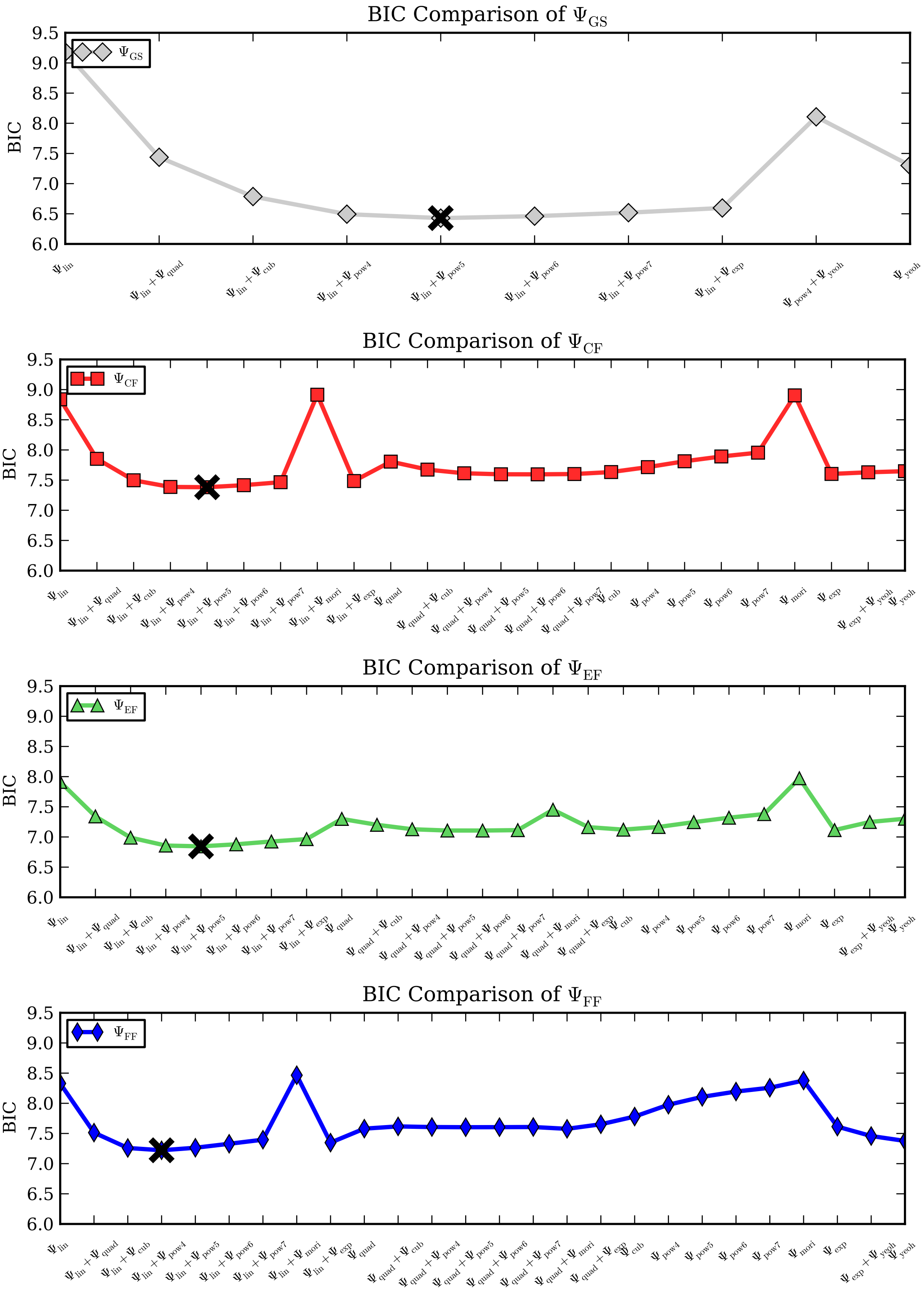

BIC Comparison of Ψ_{GS}

BIC Comparison of Ψ_{CF}

BIC Comparison of Ψ_{EF}

BIC Comparison of Ψ_{FF}

Figure 7.9: Comparison of combinations of strain energy density function (SEF) terms for Ψ_{GS}, Ψ_{CF}, Ψ_{EF}, and Ψ_{FF} based on the Bayesian information criterion (BIC). The black cross indicates the lowest BIC, i.e. the best agreement.

contribution of the fibers rises significantly. Comparing the stress-strain curves of the CF with the FF, a cross-over point exists, meaning the CF are more compliant at the start but become stiffer for large strains; this effect is reflected in the material parameters since c_{lin} is smaller for the CF, whereas the higher order term is the smallest for the FF.

7.3 Conclusion

In this chapter, a method to determine a homogenized and a constituent-based material model for lung parenchyma has been presented. The proposed methodology allows us to compare the suitability of different existing and new models with each other. In the literature no SEF can be found that is capable of sufficiently reproducing the complex compressible, stiffening behavior observed in the experiments presented in chapter 6. To the author's knowledge, previously only Gao et al. (2006) determined material parameters for a SEF describing the homogenized lung parenchyma. However, as mentioned in the introduction, this approach has some major limitations and an exponential SEF (as they proposed) is found to be incapable to reproduce the experimental results adequately.

A mayor advantage of this study is that not only the material parameters of one preselected SEF are optimized but rather many "potential SEF" are compared with each other, in order to find the optimal material model. Another advantage is the usage of the FEM, because it reproduces the same loading states for the fitting as the specimen experienced during the experiment. This means, there is no need for additional assumption, like a state of uniaxial tension, a plain stress or strain state. This leads to a globally applicable material model. In order to validate our determined material model a simulation of the biaxial tensile test performed by Vawter et al. (1978) is performed (data not shown). Qualitatively, our material model showed good agreement.

Therefore, the constitutive models proposed in this work are the first material models for lung parenchymal tissue that adequately reflects the complex behavior of lung parenchymal tissue.

Additionally, the constituent-based material model is the first material model for lung parenchyma including quantified contributions for the three major load-bearing constituents, i.e. the EF, the CF and the GS, as well as their interaction, i.e. FF.

It is important to note that the methodology presented here can also be used for the development of any material model, homogenized as well as constituent-based and hence should have a large range of applications in the future.

The presented material models are used within our virtual lung model (Wall et al., 2010b), in order to realistically determine the loading of the lung tissue during mechanical ventilation. The homogenized material model can be used to model the influence of the healthy lung parenchyma, whereas the constituent-based material model can be applied to simulate healthy as well as diseased parenchymal tissue, e.g. for simulations of fibrosis, where the fiber density changes dramatically. To do so, the corresponding constituent contribution, can be increased or completely removed.

To conclude, the development of novel sophisticated constitutive models for homogenized lung parenchyma and for the individual load-bearing constituents was presented. This approach will help to model the behavior of the lung tissue and quantify its strains and stresses during mechanical ventilation.

8 Local Strain Distribution in Real Three-Dimensional Alveolar Geometries

So far, the majority of models found in literature was quantifying the global loading of the parenchymal tissue. However, for diseases like VALI especially the local loading of the tissue is important. Hence, there is the need to investigate the connection between local and global deformation in the lung parenchyma, i.e. how does the complex microstructure influence the loading of the tissue at the alveolar and even further down at the cell level. Therefore, in this section, a FE simulation of alveolar geometries, obtained from Synchrotron-based X-ray tomographic microscopy (SRXTM), is presented. This scanning method produces, for the first time, three-dimensional images of alveoli. Due to the high resolution, it is possible to model the alveolar walls in three-dimensions, including the actual wall thickness. Additionally, due to the scanning method the imaged specimen can be extracted from the central region of the lung, i.e. this method is not limited to the pleural region of the lung. This allows us to obtain a detailed insight into the three-dimensional deformation of the individual alveolar walls, see Rausch et al. (2011a).

8.1 Methodology

To enable the FE analysis of the deformation behavior of real alveolar geometries, several steps are necessary. First, PCLS are prepared from isolated rat lungs, see section 6.1.1 and Martin et al. (1996); Schittny (2008). Second, the slices are scanned in the Tomographic Microscopy and Coherent Radiology Experiments (TOMCAT) beamline of the Swiss Light Source (SLS). Third, a three-dimensional volume representation of the scanned images is created. Fourth, the three-dimensional volume is discretized with a volume mesh, boundary conditions are applied, and the problem is solved utilizing BACI. In the following, these steps are explained in more detail.

8.1.1 Rat Lung Sample Preparation

The samples are prepared according to Schittny (2008). Briefly, the lung of a rat at postnatal day 36 is intratracheally filled with 2.5 % glutaraldehyde ($CH_2(CH_2CHO)_2$) in 0.03 mol potassium-phosphate buffer (pH 7.4) by instillation via tracheotomy at a constant pressure of 20 cmH_2O. In order to prevent recoiling of the lung, this pressure is maintained during glutaraldehyde-fixation. Subsequently, the lungs are dissected free and immersed into in the same fixative at a temperature of 4 °C for at least 24 h.

The samples are postfixed with 1 % osmium tetroxide (OsO_4) and stained with 4 % uranyl nitrate ($UO_2(NO_3)_2$) to increase the x-ray absorption contrast. After dehydration in a graded series of ethanol, the samples are embedded in Epon 812 using acetone as intermedium. The lung samples are glued onto small metal rods of 3.2 mm diameter using Araldite^{TM}.

The handling of animals before and during the experiments, as well as the experiments themselves, are approved and supervised by the local authorities.

8.1.2 Beamline and Tomographic Imaging

The scanning is performed at the TOMCAT beamline (Stampanoni et al., 2006) at the SLS, Paul Scherrer Institute, Villigen, Switzerland. The samples are scanned at a beam energy of 12.601 keV, corresponding to a wavelength of 1 $\AA$. After penetration of the sample, the x-rays are converted into visible light by a scintillator, magnified by diffraction limited microscope optics (10× magnification) and digitized by a high-resolution 2048×2048 pixel CCD camera (pco.2000, PCO AG, Kelheim, Germany) with 14 bit dynamic range. The detector is operated in 2×2 binning mode. As a result, each recorded projection has a size of 1024×1024 pixels corresponding to 1.48 µm, the exposure time is 108 ms.

1501 projections, at equiangular positions between 0 °C and 180 °C, are recorded. The projections are post-processed and rearranged into flat field-corrected sinograms prior to being reconstructed into tomographic slices on a 16-node computing cluster using a highly optimized filtered back-projection routine. Details of the imaging workflow and reconstruction setup were described by Hintermüller et al. (2010). The resulting tomographic data set is a stack of 1024 16-bit-tiff-images, see Figure 8.1.

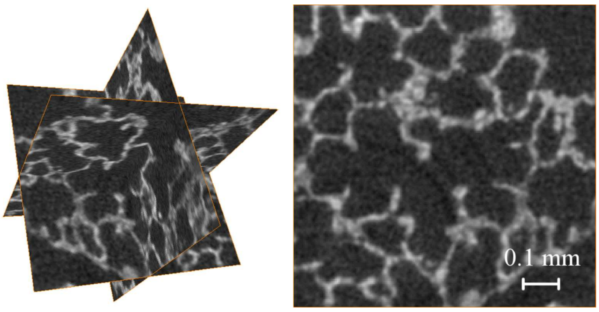

Figure 8.1: Synchrotron-based X-ray tomographic microscopy image of rat lung parenchyma. The specimen is imaged in the TOMCAT beamline of the Swiss Light Source with a voxel size of $1.48 \times 1.48 \times 1.48\,\mu$m.

8.1.3 Segmentation

In the next step, the images are segmented utilizing the commercially available software Amira 4.1.2 (Mercury Computer Systems, (Stalling et al., 2005)). For the segmentation itself the 'magic wand' tool, which is a combination of a threshold and region growth, is the most efficient. In order to assess the accuracy of the segmented geometry, the air-tissue ratio is compared with previously published data of Tschanz et al. (2003). The ratio determined for the segmented geometry shows good agreement with these results.

8.1.4 Meshing and Boundary Conditions

After creation of the geometry, a mesh is generated with the Surface Tesselation Language (STL) meshing package Harpoon (www.sharc.co.uk). Due to the complexity of the geometry, tetrahedral elements are utilized for the FE discretization. For the calculations presented in the following, a newly developed uniform nodal strain tetrahedral element with isochoric stabilization is used. The element is based on the linear interpolation used in the classical displacement-based tetrahedral element formulation but applies nodal averaging of the deformation gradient to improve the mechanical behavior. Especially in the regime of near-incompressibility, where classical linear tetrahedral elements perform very poorly, this element shows good performance (Gee et al., 2009).

In a refinement study, four different meshes are compared. A summary of mesh details is given in Table 8.1. The base level represents the average size of one side of a regular tetrahedron. Example slices through the meshes with base levels of 4.23 µm and 2.11 µm are shown in Figure 8.2. The study shows that with a base level of 3.17 µm, the FE solution can be considered as being converged, see Figure 8.3.

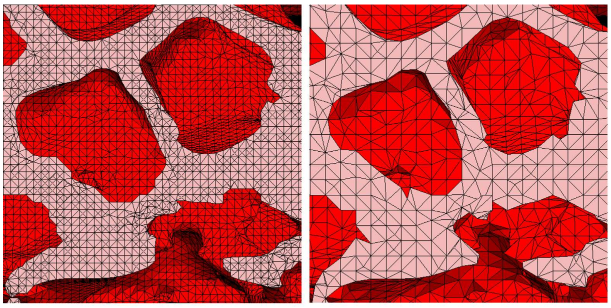

(a) (b)

Figure 8.2: Cut through the mesh (a) with base level 2.11 µm and (b) with base level 4.23 µm.

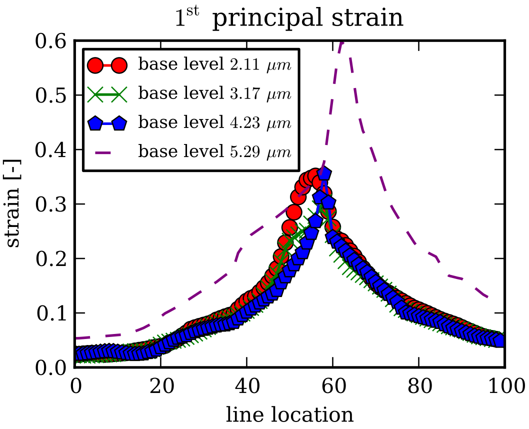

Figure 8.3: Refinement study to test the mesh quality. Four different mesh sizes are compared. The base level represents the average size of one side of a regular tetrahedron. The strains over a line within the cube are plotted. The strain magnitude does not change significantly between the base levels 2.11 and 3.17 µm, i.e. the solution can be considered as being converged.

To evaluate the influence of boundary effects, two different cubes, one with 158.57 µm and the other one with 317.14 µm side length, are compared, see Figure 8.4. These cubes will be referred to as the “small cube” and the “large cube”, respectively.

To investigate the relation of global and local deformations in the lung tissue, two different loading stats, i.e. uniaxial tension and shear deformation, are applied to the samples. In both cases, the deformation is applied as a Dirichlet boundary condition. While the deformation of the bottom surface is completely fixed, the top surface is either pulled upwards or pushed in the transverse direction depending on the considered load case, see Figure 8.5.

Table 8.1: Alveolar meshing statistics

Base level	Elements	Degrees of freedom
5.29 µm	577990	397020
4.23 µm	1164023	750297
3.17 µm	2727686	1669446
2.11 µm	8573680	5003121

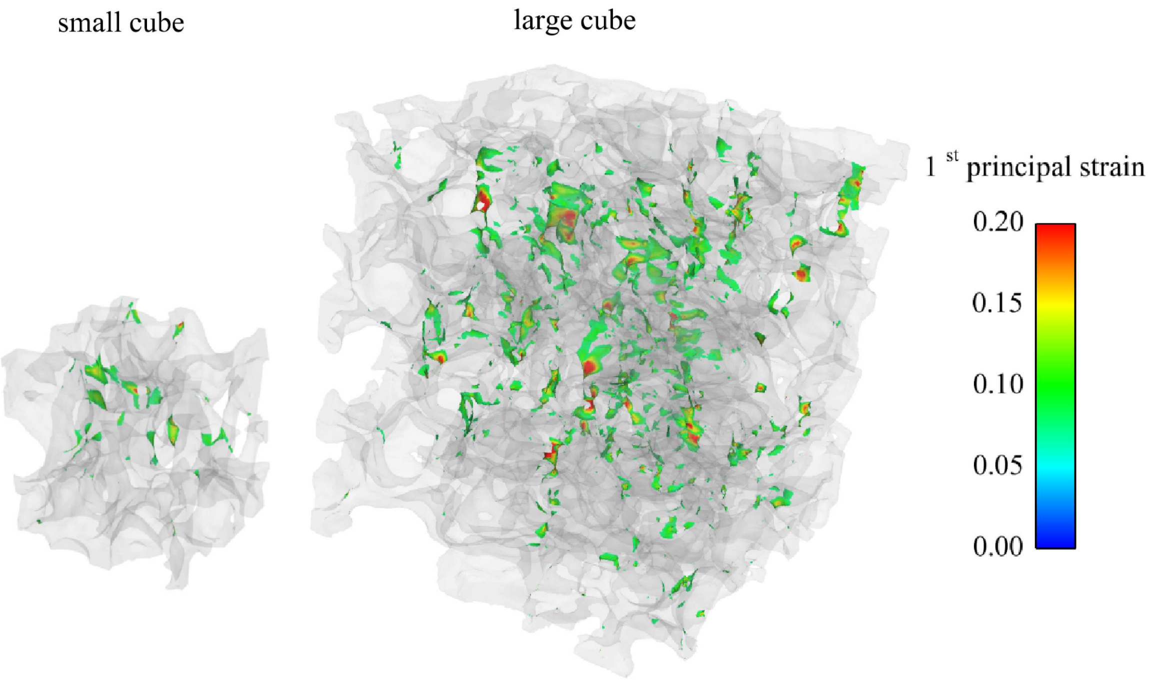

Figure 8.4: Two tested cubes of lung tissue, the "small cube" has a side length of 158.57 µm and the "large cube" has a side length of 317.14 µm. Both cubes are elongated 5 % of their initial side length. The coloring shows strain hotspot areas of the 1st principal strain which are larger than 10 %.

8.1.5 Simulation

The computations are performed with BACI. To model the material behavior of the individual alveolar walls, a Neo-Hookean formulation suggested by Holzapfel and Gasser (2001) is used

$$\Psi_{\text{neo, Holzapfel}} = E\frac{1}{4(1-\nu)}(I_1 - 3) + E\frac{(1-2\nu)}{4\nu(1+\nu)}\left(I_3^{-\frac{\nu}{1-2\nu}} - 1\right), \qquad (8.1.1)$$

with ν being the Poisson's ratio and E being the Young's modulus. For the definition of the constants see Appendix A.2.4 and A.2.1. Due to the fact that the tissue mainly consists of water, it is considered as nearly incompressible ($\nu = 0.49$). The value for E

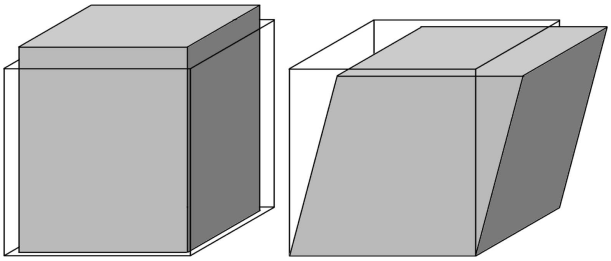

Figure 8.5: The tested deformation states are uniaxial tension and simple shear deformation of the cubes.

is fitted to experimentally determined curves ($E \approx 6.75\,\text{kPa}$), see chapter 6. The material model is only the first approximation, more detailed investigations will follow in the future. However, since the presented study is interested in the local strain distribution, rather than the local stress field, the material model is of secondary interest.

Due to the negative hydrostatic pressure in the pleural space, it can be assumed that the tissue is under tension all the time (Suki and Bates, 2008). Hence, tissue folding and unfolding at lower volumes is not considered.

8.2 Results

In a first step, strain hotspots i.e. the regions of the tissue cube with the highest strain values, are identified. Figure 8.4 shows a comparison of the strain hotspots for both cube sizes under 5 % uniaxial elongation. Due to the complex geometry, only the 1^{st} (largest) strain eigenvalues which are larger than 0.1, are shown, the remaining tissue is set to be transparent.

The most important finding is that local strains are much higher than the global extension of the cubes. This is of course expected but now can be quantified for the first time. It turns out that local strains can be up to four times higher than global strains. Additionally, the strain hotspots occur within the thinnest parts of the cube since there is less tissue to resist the deformation. This leads to an uneven strain distribution throughout the parenchymal tissue. Thin regions become overstretched, whereas regions with tissue accumulation remain relatively unchallenged. A further observation is that there are higher peak strains in the “large cube” than in the “small cube”. This is potentially due to boundary effects as will be discussed in the latter. This hypothesis is supported by the fact that in both cubes the hotspots occurred predominantly in the central regions.

In a next step, a local hotspot is investigated in more detail. Figure 8.6 shows the distributions of the 1^{st}, 2^{nd}, and 3^{rd} strain eigenvalues. The 1^{st} eigenvalues are positive, whereas the 2^{nd} and the 3^{rd} eigenvalues are both negative and of much smaller magnitude. However, the strain patterns are similar for all three eigenvalues, i.e. the peak values occur in the thinnest part of the structure.

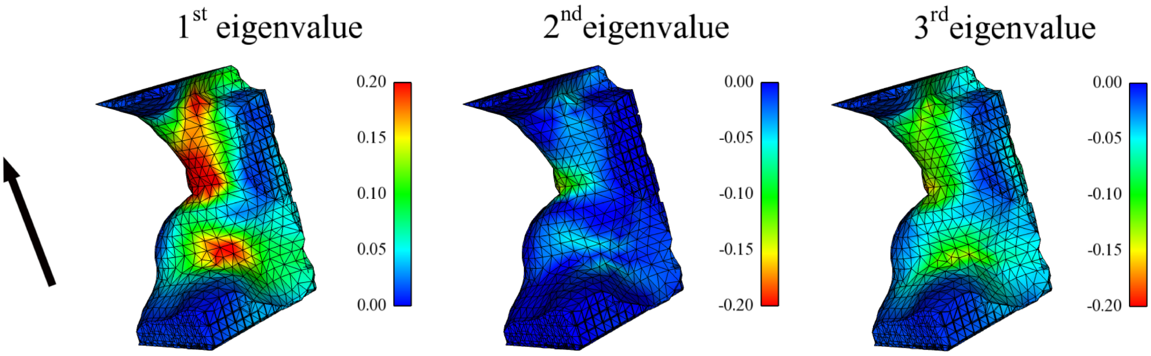

Figure 8.6: 1^{st}, 2^{nd}, and 3^{rd} strain eigenvalues of a hotspot, with the arrow indicating the direction of the uniaxial stretch. To enable a better comparison, the color-maps of the 2^{nd} and 3^{rd} strain eigenvalue are inverted.

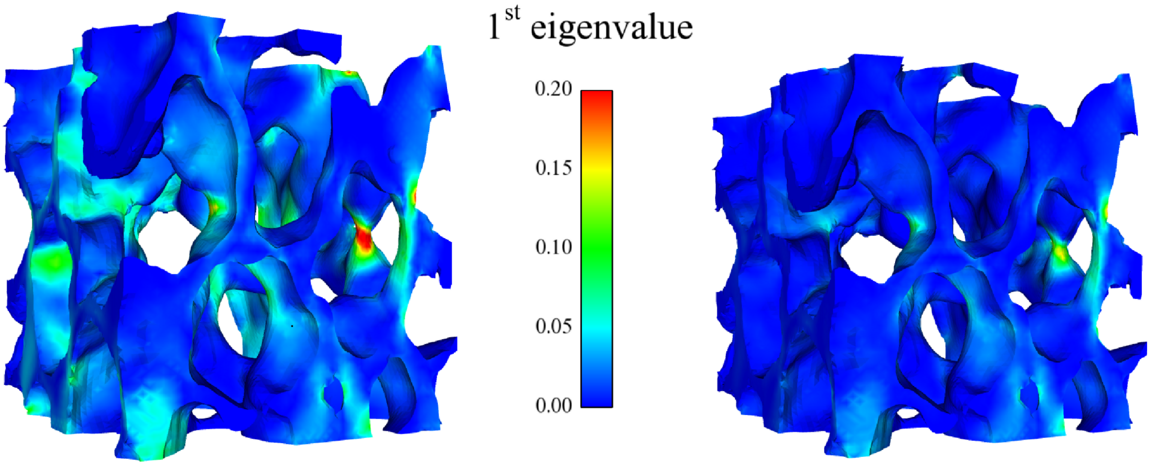

Figure 8.7: Comparison between uniaxial tension and shear deformation of the “small cube” (side length 158.57 µm). The colors indicate the first (largest) eigenvalue of the strain tensor.

The corresponding eigenvectors for a slice through this hotspot show the 1^{st} eigenvectors pointing towards the pulling direction, whereas the 2^{nd} and 3^{rd} eigenvectors lie within the normal plane of the pulling direction (data not shown). It is noteworthy that within the plane the eigenvectors do not follow a preferred direction. This behavior can be explained by the incompressibility of the tissue, i.e. if the tissue is stretched in one direction it has to be compressed in another direction. The compression seems to be quite evenly distributed within the normal plane of the pulling direction, therefore no preferred direction could be determined within this plane.

Furthermore, uniaxial tension and simple shear deformation are compared. In both cases, there is a deformation of 5 % of the initial cube side length, see Figure 8.5. This deformation is oriented in transversal direction for the shear deformation and in axial direction for the tensile deformation, as can be seen in Figure 8.7.

Clearly the peak strain values are much higher for the uniaxial tension than for the shear deformation. However, they occur in similar regions within the geometry, i.e. the above-mentioned thinner parts of the structure. These observations are valid for all three strain eigenvalues. Additionally, the distribution of the eigenvectors in a strain hotspot (data not shown) is investigated. The distribution is found to be similar for shear and tensile displacement, although there is a difference in magnitude.

Finally, the influence of the boundary conditions is investigated by comparing the strain distributions of the following four different cases:

1. the “small cube” under 5 % uniaxial elongation (small cube);
2. the “large cube” under 5 % uniaxial elongation (large cube);
3. the “small cube” under 5 % shear deformation (shear); and
4. the center region of the “large cube”, i.e. the region of equivalent size to the “small cube” in the center of the “large cube”, under 5 % uniaxial elongation (center region),

see Figure 8.8. It is obvious and expected that all distributions are skewed towards lower strain values, since there are only a few strain hotspots. One of the main findings is that even though the mean and the standard deviation are higher for the “small cube”, the extreme values are higher for the “large cube”, see Figure 8.8. If only the central region of the “large cube” is considered, the mean, standard deviation, and median are higher than all other scenarios. Additionally, the difference between the mean and the median which can be seen as a measure of the skewness of the distribution, is greatest. This backs up our assumption that more strain hotspots are developed in the “large cube”, due to a reduction of boundary effects. However, to put this in perspective, it has to be mentioned that this mainly affects the outliers whereas the main distributions are rather similar.

Another interesting fact is that the mean values of all four evaluated distributions are at least twice as small as the 5 % global strain. Furthermore, 90 % of the local strains are below 5 %. This shows clearly that there are only certain hotspots in the tissue, which have much higher strain values, whereas the majority of the tissue remains in a rather low deformation state.

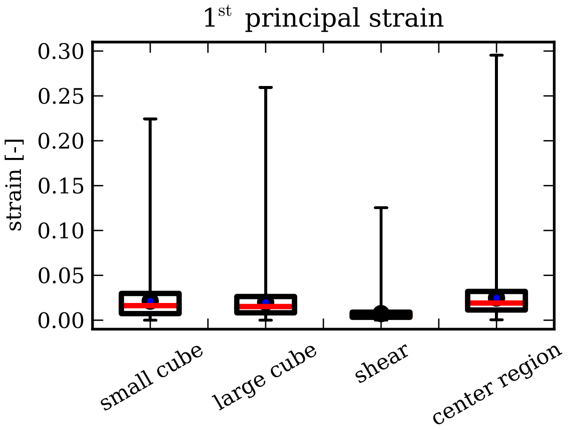

Figure 8.8: Comparison of the statistical distribution of the 1st principal strain for four different cases. First, the “small cube” under 5 % uniaxial elongation (small cube), second, the “large cube” under 5 % uniaxial elongation (large cube), third, the “small cube” under 5 % shear deformation (shear) and fourth, the center region of the “large cube”, i.e. a region of equivalent size to the “small cube” in the center of the “large cube”, under 5 % uniaxial elongation (center region). The whiskers include 99.98 % and the boxes 50 % of all measurement points (outliers are not shown). The red lines in the center of the boxes are the medians and the dots denote the means.

Finally, the distribution of the shear deformation is found to have a much smaller mean and standard deviation. The smaller standard deviation is expected due to the more uniform deformation in the cube and the lower mean is a consequence of the smaller amount of hotspots.

8.3 Discussion

In this chapter FE simulations of SRXTM-based alveolar geometries are presented. This method allows us, for the first time, to determine local three-dimensional strain states in high-resolution image-based alveolar geometries.

In contrast to previous experimental approaches (Brewer et al., 2003; Cavalcante et al., 2005; DiRocco et al., 2005; Perlman and Bhattacharya, 2007), which can only calculate an averaged extension for each of the alveolar walls, the method presented in this work is able to determine a three-dimensional strain state throughout the thickness of the tissue.

A direct comparison with other numerical approaches is difficult, since the studies in literature are investigating very regular artificially generated geometries, which of course reduces the heterogeneity of the strain field. Furthermore, they mainly investigate specific effects, rather than developing a general model, see Cavalcante et al. (2005); Denny and Schroter (2006). The only other FE study on real alveolar geometries was performed by Gefen et al. (1999). However their model was limited to two-dimensional geometries.

A further advantage of the presented method is the quality of the newly developed stabilized node-based uniform strain tetrahedron. The problem with normal tetrahedral elements is that they produce parasitic stresses for nearly incompressible materials, leading to too stiff behavior. With the nodal strain tetrahedron, however, these so-called volumetric locking effects can be neglected.

8.4 Conclusion

From the FE analysis, two main conclusions can be drawn. First, there are certain hotspots in the alveolar geometry which are especially at risk for overstretching. These obviously tend to be in the thinnest regions. Second, a small global strain can lead to significantly larger local strains. These conclusions are found to be independent of the loading type.

Looking at *in vitro* experiments on alveolar type II cells (Ning and Wang, 2007; Vlahakis et al., 1999; Chandel and Sznajder, 2000; Copland and Post, 2007), there is disagreement on how much stretch causes inflammatory reactions. The numbers range from strains of 0.05 up to strains of 0.3, see section 4.1.4. Comparing these values with the local peak strains found in the presented simulations, a global strain of 0.05 turns out to be sufficient to cause inflammation in any cases, since it causes local strains of up to 0.4 which is higher than every threshold value reported in literature. This presents an interesting observation as it suggests that the amount of stretching done in these experiments may not be representative of the *in vivo* environment or at the very least maybe an underestimation. This large increase in strain from the global to the local level shows that inflammatory reactions potentially initiate much earlier than previously thought.

For this reason, the presented simulations will be included within a multi-scale approach for alveolar ensemble (Wiechert and Wall, 2010). This allows us to project the global parenchymal deformation down to the level of a single alveolar ensemble, in order to provide realistic boundary conditions. This method has the advantage that local alveolar strain fields in large geometries, for example PCLS, can be determined.

Dassow et al. (2010) recently measured calcium fluxes, which are known to be induced by lung stretch, within the alveolar walls of these PCLS in a bioreactor. With this experimental approach and our computational models, the local strain fields in PCLS could be directly compared with the locations of increased calcium fluxes, hence providing a mechanical-biological pathway for the initiation of ventilator-induced lung inflammation.

The presented model does not include any surface tension effects. Hence in reality, an overall stiffer behavior can be expected. To investigate these effects further, a surface tension model developed previously by Wiechert et al. (2009) will be included in the future.

9 Summary and Outlook

In this thesis, sophisticated material models for alveolar parenchyma were developed. With these material models stresses and strains in the parenchymal tissue can be determined. Furthermore, the relation between these global stresses and strains and the deformation within individual alveolar walls was determined by performing FE simulations of image-based three-dimensional alveolar geometries.

In the following, a short overview of the achievement of the specific aims, defined in section 5, is given.

AIM 1 To develop an experimental testing protocol in order to determine the elastic material behavior of lung parenchyma.

This aim was achieved. An experimental protocol in order to determine the material behaviour of lung parenchyma is developed. This testing procedure includes a preconditioning protocol, needed to eliminate viscous effects. The three major advantages of the proposed testing protocol are:

1. The slice dimensions are reproducible.
2. Several specimens per animal can be tested.
3. The specimens are still viable during testing.

A drawback of the testing protocol is the lateral contraction is very coarse. This is due to the low time and space resolution of the utilized camera. For the future, image tracking with a high-resolution camera is suggested. This could further improve the experimental results, for the reasons described below:

1. The higher spatial resolution increases the accuracy of the measured values.
2. The higher time resolution increases the number of measured values.
3. Automatic image tracking, in comparison to the manual tracking used in this work, can reduce the post-processing time of the experiment.

4. Image tracking allows to determine a strain field, rather than individual points, which would increase the accuracy of the fit.

AIM 2 To extend the experimental methodology to investigate the influence of the individual tissue constituents (CF and EF).

This aim was achieved. An experimental protocol, which allows the determination of the influence of the individual tissue components and their interaction was developed It determines the influence of the ground substance (GS), the collagen fibers (CF), the elastin fibers (EF) and their interaction (FF). The presented protocol allows for the first time to quantify the contribution of these components. Despite the fact that it was tested that the individual fiber networks were destroyed, it remains unclear if leftover fibers remain in the tissue. These remnants could cause artificial changes in the determined stress-strain curves. A possibility to investigate the influence of the remaining fiber parts would be to perform the tensile tests under a 2-photon microscope. This has the advantage that fibers are visible and the amount of remaining fibers could be documented and included in the studies.

Furthermore, since the lung tissue is viscoelastic the experimental protocol will need to be extended, in order to enable the characterization of time-dependent effects.

AIM 3 To develop an inverse analysis methodology in order to deduce a hyperelastic material model for soft biological tissue from experiments.

This aim was achieved. An inverse analysis methodology to determine hyperelastic material models for soft biological tissues from experimental results was developed. Suitable non-linear, compressible and elastic mathematical models were formulated ("potential SEF"), which reproduce the experimentally determined behavior in an adequate way. To optimize the material parameters of a "potential SEF", the experiment is simulated with varying material parameters, according to an optimization algorithm, until the optimal fit for a predefined target function is achieved. Using this methodology several "potential SEFs" were compared with each other in order to determine the material model that is suited best to describe the complex behavior of lung parenchyma. The advantages of this methodology are described below:

1. Due to the fact that a three-dimensional deformation state of the specimen during the experiment can be accurately mapped with the FE simulation, the approach is

not limited to a specific strain or stress state, like for example uni-axial tension. As a consequence, the determined SEF can predict other strain-states as well.

2. The optimization is implemented directly in the FE code. Hence, no additional programs are necessary.
3. The methodology is not limited to lung tissue. It can be applied to any material and is suitable for arbitrary behavior including viscoelastic and anisotropic materials.

AIM 4 To determine a phenomenological and a constituent-based material model for lung parenchyma.

This aim was achieved. Two material models for lung parenchyma, a phenomenological and a constituent-based approach, were determined. The constituent-based material model is the first material model quantitatively accounting for the contribution of individual fiber families and their interaction. The material models will be used within our virtual lung model for the following applications:

- Simulation of diseases, like fibrosis, in order to get a better understanding of the underlying processes.
- Comparison of the influence of different ventilation protocols on stresses and stains in the parenchymal tissue, in order to compare the outcome of different ventilation strategies.

In the future, further experiments are needed in order to validate the predictive behavior of the material models. Furthermore, the material models need to be extended, in order to include viscoelastic effects. Additionally, due to the fact that a constituent-based material model includes individual summands for both fiber families, the fiber density distribution can be included in our virtual lung model. This means that the contribution of the individual constituents can be correlated with the fiber density distribution gained from imaging. This would allow us to consider spatial differences and improve the localization of risk areas within the alveolar tissue.

AIM 5 To perform a FE simulation on image-based alveolar geometries, in order to determine the deformation within the alveolar walls for a given global deformation state.

This aim was achieved. The deformation within the alveolar wall was determined, using FE simulations with image-based alveolar geometries. The two main conclusions of the

FE analysis are that:

1. There are certain hotspots in the alveolar geometry, which are especially at risk of overstretching.
2. A small global strain can cause up to a fourfold as high local strains within thin tissue regions.

One major problem with this type of simulations is the large size of the discretization, making the simulation numerically very expensive. For this reason, it should be investigated whether the image-based alveolar geometries could be replaced by artificially generated alveolar geometries, see Wall et al. (2010b). The advantage of artificially generated geometries is that, due to their regular shape, they can be meshed with less hexahedral elements, which reduces the computational effort.

Furthermore, the influence of the surface tension on the strain-peaks will need further attention. Since the surface tension always works against the deformation it needs to be investigated whether including the surface tension effects will even out the deformations and reduce the peak strains. This could be further investigated by including a previously developed surfactant model in the simulations (Wiechert et al., 2009).

In the next step, a material model for the individual alveolar wall will be determined. For this reason, the material model fitting procedure will be combined with a previously developed multi-scale approach (Wiechert and Wall, 2010). With this method, the behavior on the parenchymal level and on the alveolar level can be simulated simultaneously. The macro-scale (parenchymal level) gives its deformation state ($\mathbf{F}$) to the micro-scale (alveolar level), thereby defining a boundary condition for alveolar simulations similar to the scenario investigated in chapter 8. After having performed the alveolar simulation, the homogenized parenchymal stresses are determined by averaging over the cube volume. The resulting stresses ($\mathbf{S}$) are returned to the macro-scale. Hence, the micro-scale acts like a material model for the macro-scale. In order to determine the material parameters for the micro-scale, a similar simulation as introduced in chapter 7 is performed. However, in this case the material parameters of the micro-scale are fitted. A preliminary study, with a simplified micro-structure has already shown that the methodology is suitable to deduce micro-scale parameters from macroscopic experiments, see Figure 9.1.

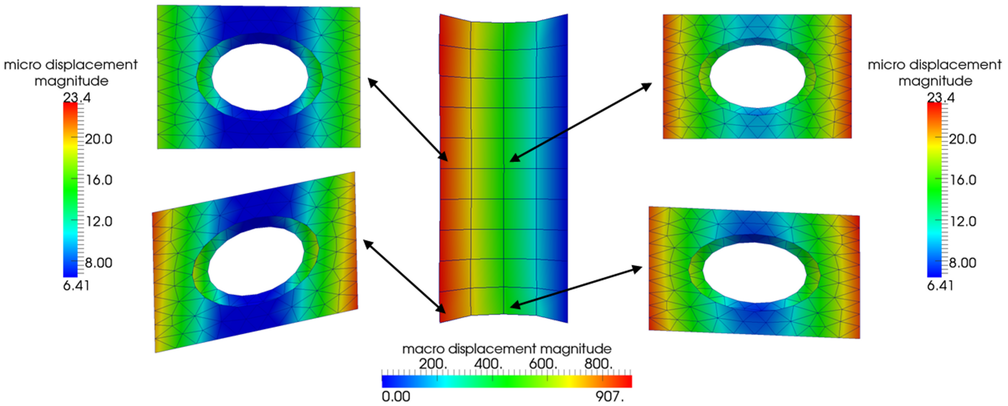

Figure 9.1: Preliminary study for combining a multi-scale approach with the inverse analysis methodology developed as part of this work. The micro-scale, i.e. the alveolar geometry is simplified with a cube with a whole in the middle. The material parameters are fitted on the micro-scale such that the macroscopic response is in optimal agreement with the experiment. The locally different states of deformation in the micro-scale can be clearly seen on the exemplarily displayed micro-scale cubes.

Summing up, in this study a general methodology for determining material models for soft biological tissues was introduced. Furthermore, two sophisticated material models for lung parenchyma were determined, a phenomenological one and a model accounting for the contribution of the individual constituents of the micro-structure. These material models can be utilized within our virtual lung model in order to determine global strains and stresses in the lung tissue. Another major achievement of this work is the quantitative correlation of these global deformation states with three-dimensional strain distributions in individual alveolar walls. These strains are of utmost importance, since they are the trigger causing inflammatory reactions during VALI. Hence, the developed approaches are essential to promote further understanding of this disease and formulate improved protective ventilation protocols in the future.

A Appendix

A.1 Important Theorems

A.1.1 Reynolds Transport Theorem

$$\frac{\mathrm{d}}{\mathrm{d}t}\int_{\mathcal{B}_t}(\bullet)\,\mathrm{d}v = \int_{\mathcal{B}_t}\Big(\dot{(\bullet)} + (\bullet)\nabla\cdot\mathbf{v}\Big)\,\mathrm{d}v = \int_{\partial\mathcal{B}_t}(\bullet)\,(\mathbf{v}\cdot\mathbf{n})\,\mathrm{d}a \tag{A.1.1}$$

A.1.2 Gauss' Divergence Theorem

$$\int_{\mathcal{B}_t}\nabla\cdot\mathbf{G}\,\mathrm{d}v = \int_{\partial\mathcal{B}_t}\mathbf{G}\cdot\mathbf{n}\,\mathrm{d}a. \tag{A.1.2}$$

A.2 Common Constants in Material Science

In solid mechanics, there are multiple commonly used stiffness measures which can also be transformed into each other.

A.2.1 Young's Modulus

The slope of the stress-strain curve at any point is called the tangent modulus, it is a measure of the stiffness of the material. The tangent modulus of the initial, linear portion of a stress-strain curve is called Young's modulus E. It can be experimentally determined from the slope of a stress-strain curve created during tensile tests. It is always positive and defined as the ratio of the uniaxial stress over the uniaxial strain, see

$$E = \frac{\text{tensile stress}}{\text{tensile strain}}\left[\frac{\mathrm{N}}{\mathrm{mm}^2}\right]. \tag{A.2.1}$$

Anisotropic materials have different Young's moduli depending on the direction of the applied force with respect to the material's structure.

A.2.2 Bulk Modulus

The bulk modulus κ describes the resistance of a material against compression. It is always positive and defined as

$$\kappa = -V\frac{\partial p}{\partial V}\left[\frac{\mathrm{N}}{\mathrm{mm}^2}\right] \tag{A.2.2}$$

with p being the pressure and V being the volume. The minus arises from the fact that with increasing pressure the volume decreases, however the bulk modulus κ is defined positive. The inverse of the bulk modulus is a measure for the compressibility of a substance.

A.2.3 Shear Modulus

The shear modulus G, also known as modulus of rigidity or Lamé's second parameter, describes the resistance against shear deformation. It is always positive and defined as

$$G = \frac{\text{shear stress}}{\text{shear strain}}\left[\frac{\mathrm{N}}{\mathrm{mm}^2}\right] \tag{A.2.3}$$

in the range of a linear stress-strain curve.

A.2.4 Poisson's Ratio

The Poisson's ratio ν is the ratio of the strain perpendicular to the applied load (ϵ_{trans}), to the strain in the direction of the applied load (ϵ_{axial}), i.e.

$$\nu = -\frac{\epsilon_{\text{trans}}}{\epsilon_{\text{axial}}}\,[-]\,. \tag{A.2.4}$$

The Poisson's ratio of a stable material cannot be less than -1.0 or greater than 0.5 due to the requirement that E, G, and κ have positive values.

A.2.5 Lamé's first parameter

Lamé's first parameter λ is is defined as

$$\lambda = \frac{E}{(1+\nu)(1-2\nu)}. \tag{A.2.5}$$

Although, Lamé's first parameter λ can be negative in principal, it is positive for most materials.

A.2.6 Transformation of Stiffness Measures

The transformation of the above introduced stiffness measures into each other is shown in Table A.1.

Table A.1: Transformation of the different stiffness moduli into each other.

	Young's modulus E	bulk modulus κ	shear modulus G	Lamé's first parameter λ
E		$3\kappa(1-2\nu)$	$2G(1+\nu)$	$\frac{\lambda(1+\nu)(1-2\nu)}{\nu}$
κ	$\frac{E}{3(1-2\nu)}$		$\frac{2G(1+\nu)}{3(1-2\nu)}$	$\frac{\lambda(1+\nu)}{3\nu}$
G	$\frac{E}{2(1+\nu)}$	$\frac{3\kappa(1-2\nu)}{2(1+\nu)}$		$\frac{\lambda(1-2\nu)}{2\nu}$
λ	$\frac{E\nu}{(1+\nu)(1-2\nu)}$	$\frac{3\kappa\nu}{1+\nu}$	$\frac{2G\nu}{1-2\nu}$	

A.3 Common Constants in Physiology

A.3.1 Compliance

The tendency of a hollow organ to resist recoil towards its original dimensions is called compliance. The compliance of the lung is defined as the slope of the p-V curve, it can be approximated with

$$\text{compliance} = \frac{\Delta V}{\Delta p}\left[\frac{1}{\text{kPa}}\right],\left[\frac{\text{ml}}{\text{cmH}_2\text{O}}\right]. \tag{A.3.1}$$

As most other relationships in medicine, the p-V curve of the lung is non-linear, i.e. the compliance changes according to the loading stage of the system.

A.3.2 Elastance

The reciprocal value of the compliance is called elastance.

A.3.3 Resistance

To keep gas flowing through a pipe ($\dot{V} > 0$), a pressure change (Δp) is needed. The ratio between pressure change and resulting flow is defined as resistance. The resistance equals the slope of the pressure-flow curve and can be calculated as

$$\text{resistance}=\frac{\Delta p}{\dot{V}}. \tag{A.3.2}$$

A.4 Common Statistical Measures

A.4.1 Mean

In this work, the term mean refers to the arithmetic mean, which is calculated as

$$\text{mean} = \frac{1}{n} \cdot \sum_{i=1}^{n} x_i, \tag{A.4.1}$$

with n being the number of measurements and x_i being the individual measurement values.

A.4.2 Standard Deviation

The standard deviation (sd) of a sample calculates as

$$\text{sd} = \sqrt{\frac{1}{n} \sum_{i=1}^{n} (x_i - \text{mean})^2} \tag{A.4.2}$$

with the mean given in equation (A.4.1), n being the number of measurements, and x_i being the individual measurement values.

A.4.3 Coefficient of Variation

The coefficient of variation (CV) is defined as

$$\text{CV} = \frac{\text{sd}}{\text{mean}} \tag{A.4.3}$$

the mean and sd given in equation (A.4.1) and (A.4.2), respectively.

Bibliography

Abel, S., Finney, S., Brett, S., Keogh, B., Morgan, C., and Evans, T. (1998). Reduced mortality in association with the acute respiratory distress syndrome (ARDS). *British Medical Journal*, 53(4):292–294.

Abràmoff, M., Magalhaes, P., and Ram, S. (2004). Image processing with imagej. *Biophotonics International*, 11(7):36–42.

American Thoracic Society, European Society of Intensive Care Medicine, Societé de Réanimation Langue Française (1999). International consensus conferences in intensive care medicine. Ventilator-associated lung injury in ARDS. *Intensive Care Medcine*, 25(12):1444–1452.

Ashbaugh, D., Bigelow, D. B., Petty, T., and Levine, B. (1967). Acute respiratory distress in adults. *The Lancet*, 290(7511):319–323.

Ball, J. (1977). Convexity conditions and existence theorems in nonlinear elasticity. *Archive for Rational Mechanics and Analysis*, 63(4):337–403.

Balzani, D. (2006). *Polyconvex Anisotropic Energies and Modeling of Damage Applied to Arterial Walls*. PhD thesis, Institut für Mechanik, Abteilung Bauwissenschaften, Fakultät für Ingenieurwissenschaften.

Balzani, D., Neff, P., Schröder, J., and Holzapfel, G. (2006). A polyconvex framework for soft biological tissues. adjustment to experimental data. *International Journal of Solids and Structures*, 43:6052–6070.

Barnas, G., Yoshino, K., Stamenovic, D., Kikuchi, Y., Loring, S., and Mead, J. (1989a). Chest wall impedance partitioned into rib cage and diaphragm-abdominal pathways. *Journal of Applied Physiology*, 66(1):350–359.

Barnas, G. M., Mackenzie, C. F., Skacel, M., Hempleman, S. C., Wicke, K. M., Skacel, C. M., and Loring, S. H. (1989b). Amplitude dependency of regional chest wall resistance and elastance at normal breathing frequencies. *The American Review of Respiratory Disease*, 140(1):25–30.

Basser, P., Schneiderman, R., Bank, R., Wachtel, E., and Maroudas, A. (1998). Mechanical properties of the collagen network in human articular cartilage as measured by osmotic stress technique. *Archives of Biochemistry and Biophysics*, 351(2):207–219.

Bates, J., Maksym, G., and Suki, B. (1994). Lung tissue rheology and 1/f noise. *Annals of Biomedical Engineering*, 22(6):674–681.

Bates, J. H., Shardonofsky, F., and Stewart, D. E. (1989). The low-frequency dependence of respiratory system resistance and elastance in normal dogs. *Respiration Physiology*, 78(3):369–382.

Belytschko, T., Liu, K., and Moran, B. (2005). *Nonlinear Finite Elements for Continua and Structures*. John Wiley & Sons, LTD.

Bernard, G. R., Artigas, A., Brigham, K. L., Carlet, J., Falke, K., Hudson, L., Lamy, M., LeGall, J. R., Morris, A., and Spragg, R. (1994). Report of the american-european consensus conference on acute respiratory distress syndrome: definitions, mechanisms, relevant outcomes, and clinical trial coordination. consensus committee. *Journal of Critical Care*, 9(1):72–81.

Blatz, P. J. and Ko, W. L. (1962). Application of finite elastic theory to the deformation of rubbery materials. *Journal of Rheology*, 6(1):223–252.

Bonet, J. and Wood, R. D. (1997). *Nonlinear contiuum mechanics for finite element analysis*. Cambridge University Press, Cambridge.

Brewer, K. K., Sakai, H., Alencar, A. M., Majumdar, A., Arold, S. P., Lutchen, K. R., Ingenito, E. P., and Suki, B. (2003). Lung and alveolar wall elastic and hysteretic behavior in rats: effects of in vivo elastase treatment. *Journal of Applied Physiology*, 95(5):1926–1936.

Brower, R., Ware, L., Berthiaume, Y., and Matthay, M. (2001). Treatment of ards. *Chest*, 120(4):1347–1367.

Brown, R., Butler, J., Rogers, R., and Leith, D. (1994). Mechanical connections between elastin and collagen. *Connective Tissue Research*, 30(4):295–308.

Budiansky, B. and Kimmel, E. (1987). Elastic moduli of lungs. *Journal of Applied Mechanics*, 54(2):351–358.

Carton, R. W., Dainauskas, J., and Clark, J. W. (1962). Elastic properties of single elastic fibers. *Journal of Applied Physiology*, 17:547–551.

Cavalcante, F. S., Ito, S., Sakai, H., Alencar, A. M., Almeida, M. P., Andrade, I. S., A, M., Ingenito, E. P., and Suki, B. (2005). Mechanical interactions between collagen and proteoglycans: implications for the stability of lung tissue. *Journal of Applied Physiology*, 98(2):672–679.

Chandel, N. S. and Sznajder, J. I. (2000). Stretching the lung and programmed cell death. *American Journal of Physiology- Lung Cellular and Molecular Physiology*, 279(6):1003–1004.

Comerford, A., Förster, C., and Wall, W. A. (2010). Structured tree impedance outflow boundary conditions for 3d lung simulations. *Journal of Biomechanical Engineering*, 132(8):081002–1–10.

Copland, I. B. and Post, M. (2007). Stretch-activated signaling pathways responsible for early response gene expression in fetal lung epithelial cells. *Journal of Cellular Physiology*, 210(1):133–143.

Crapo, J. (2000). *Respiratory structure and function*. Cecil Textbook of Medicine. Philadelphia. WB Saunders Company.

Crystal, R. G., Bradley, K. H., McConnell-Breu, S. D., Collins, J. F., Hanca, A. J., and Cowan, M. J. (1975). Collagen in the lung: development of a technology applicable to human lung disease. *Chest*, 67(2 Suppl):30–31.

Dassow, C., Wiechert, L., Martin, C., Schumann, S., Müller-Newen, G., Pack, O., Guttmann, J., Wall, W. A., and Uhlig, S. (2010). Biaxial distension of precision-cut lung slices. *Journal of Applied Physiology*, 108(3):713–721.

Debes, J. C. and Fung, Y. C. (1992). Effect of temperature on the biaxial mechanics of excised lung parenchyma of the dog. *Journal of Applied Physiology*, 73(3):1171–1180.

Delfino, A., Stergiopulos, N., Moore, J. E., and Meister, J. J. (1997). Residual strain effects on the stress field in a thick wall finite element model of the human carotid bifurcation. *Journal of Biomechanics*, 30(8):777–786.

Denny, E. and Schroter, R. C. (1997). Relationships between alveolar size and fibre distribution in a mammalian lung alveolar duct model. *Journal of Biomechanical Engineering*, 119(3):289–297.

Denny, E. and Schroter, R. C. (2000). Viscoelastic behavior of a lung alveolar duct model. *Journal of Biomechanical Engineering*, 122(2):143–151.

Denny, E. and Schroter, R. C. (2006). A model of non-uniform lung parenchyma distortion. *Journal of Biomechanics*, 39(4):652–663.

DiRocco, J. D., Carney, D. E., and Nieman, G. F. (2005). *The Mechanism of Ventilator-induced Lung Injury: Role of Dynamic Alveolar Mechanics*. Springer Berlin Heidelberg.

DiRocco, J. D., Pavone, L. A., Carney, D. E., Lutz, C. J., Gatto, L. A., Landas, S. K., and Nieman, G. F. (2006). Dynamic alveolar mechanics in four models of lung injury. *Intensive Care Medicine*, 32(1):140–148.

Doll, S. and Schweizerhof, K. (2000). On the development of volumetric strain energy functions. *Journal of Applied Mechanics*, 67:17–21.

Dos Santos, C. C. and Slutsky, A. S. (2000). Invited review: mechanisms of ventilator-induced lung injury: a perspective. *Journal of Applied Physiology*, 89(4):1645–1655.

Dos Santos, C. C. and Slutsky, A. S. (2006). The contribution of biophysical lung injury to the development of biotrauma. *Annual Review of Physiology*, 68:585–618.

Dreyfuss, D., Soler, P., Basset, G., and Saumon, G. (1988). High inflation pressure pulmonary edema. respective effects of high airway pressure, high tidal volume, and positive end-expiratory pressure. *The American Review of Respiratory Disease*, 137(5):1159–1164.

Ethier, C. R. and Simmons, C. A. (2007). *Introductory biomechanics: from cells to organisms*. Cambridge University Press.

Faffe, D. and Zin, W. (2009). Lung parenchymal mechanics in health and disease. *Physiological Reviews*, 89(3):759–775.

Faffe, D. S., D'Alessandro, E. S., Xisto, D. G., Antunes, M. A., Romero, P. V., Negri, E. M., Rodrigues, N. R. D., Capelozzi, V. L., Zin, W. A., and Rocco, P. R. M. (2006). Mouse strain dependence of lung tissue mechanics: role of specific extracellular matrix composition. *Respiratory Physiology and Neurobiology*, 152(2):186–196.

Faffe, D. S., Silva, G. H., Kurtz, P. M. P., Negri, E. M., Capelozzi, V. L., Rocco, P. R. M., and Zin, W. A. (2001). Lung tissue mechanics and extracellular matrix composition in a murine model of silicosis. *Journal of Applied Physiology*, 90(4):1400–1406.

Frankus, A. and Lee, G. C. (1974). A theory for distortion studies of lung parenchyma based on alveolar membrane properties. *Journal of Biomechanics*, 7(1):101–107.

Fredberg, J. J. and Stamenovic, D. (1989). On the imperfect elasticity of lung tissue. *Journal of Applied Physiology*, 67(6):2408–2419.

Fukaya, H., Martin, C. J., Young, A. C., and Katsura, S. (1968). Mechanial properties of alveolar walls. *Journal of Applied Physiology*, 25(6):689–695.

Fung, Y. (1984). Structure and stress-strain relationship of soft tissues. *American Zoologist*, 24(1):13–22.

Fung, Y. (1993). *Biomechanics Mechanical Properties of living Tissue Seccond Edition*. Springer-Verlag.

Fung, Y. C. and Sobin, S. S. (1981). The retained elasticity of elastin under fixation agents. *Journal of Biomechanical Engineering*, 103(2):121–122.

Gao, J., Huang, W., and Yen, R. T. (2006). Mechanical properties of human lung parenchyma. *Biomedical Sciences Instrumentation*, 42:172–180.

Gee, M. W., Dohrmann, C. R., Key, S. W., and Wall, W. A. (2009). A uniform nodal strain tetrahedron with isochoric stabilization. *International Journal for Numerical Methods in Engineering*, 78(4):429–443.

Gefen, A., Elad, D., and Shiner, R. J. (1999). Analysis of stress distribution in the alveolar septa of normal and simulated emphysematic lungs. *Journal of Biomechanics*, 32(9):891–897.

Gray, H. and Bannister, L. H. (1995). *Gray's anatomy: The Anatomical Basis of Medicine and Surgery*. Churchill Livingstone London.

Grytz, R. and Meschke, G. (2009). Constitutive modeling of crimped collagen fibrils in soft tissues. *Journal of the Mechanical Behavior of Biomedical Materials*, 2(5):522–533.

Harman, E. (2011). Acute respiratory distress syndrome. *eMedcine*.

Hastie, T., Tibshirani, R., and Friedman, J. (2009). *The Elements of Statistical Learning: Data Mining, Inference, and Prediction.* Springer.

Haut, R. and Little, R. (1972). A constitutive equation for collagen fibers. *Journal of Biomechanics*, 5(5):423–430.

Heroux, M., Bartlett, R., Howle, V., Hoekstra, R., Hu, J., Kolda, T., Lehoucq, R., Long, K., Pawlowski, R., and Phipps, E. (2005). An overview of the trilinos project. *ACM Transactions on Mathematical Software (TOMS)*, 31(3):397–423.

Hildebrandt, J. (1966). *Mechanical Properties of Mammalian Lung*. PhD thesis, University of Washington.

Hildebrandt, J. (1969). Dynamic properties of air-filled excised cat lung determined by liquid plethysmograph. *Journal of Applied Physiology*, 27(2):246–250.

Hildebrandt, J. (1970). Pressure-volume data of cat lung interpreted by a plastoelastic, linear viscoelastic model. *Journal of Applied Physiology*, 28(3):365–372.

Hintermüller, C., Marone, F., Isenegger, A., and Stampanoni, M. (2010). Image processing pipeline for synchrotron-radiation-based tomographic microscopy. *Journal of Synchrotron Radiation*, 17(4):550–559.

Holzapfel, G. A. (2004). *Nonlinear Solid Mechanics*. John Wiley & Sons, LTD.

Holzapfel, G. A. and Gasser, T. C. (2001). A viscoelastic model for fiber-reinforced composites at finite strains: Continuum basis, computational aspects and applications. *Computer Methods in Applied Mechanics and Engineering*, 190(34):4379–4403.

Holzapfel, G. A., Gasser, T. C., and Ogden, R. W. (2000). A new constitutive framework for arterial wall mechanics and a comparative study of material models. *Journal of Elasticity*, 61(1 - 3):1 – 48.

Hoppin, F. G., Lee, G. C., and Dawson, S. V. (1975). Properties of lung parenchyma in distortion. *Journal of Applied Physiology*, 39(5):742–751.

Horsfield, K., Dart, G., Olson, D. E., Filley, G. F., and Cumming, G. (1971). Models of the human bronchial tree. *Journal of Applied Physiology*, 31(2):207–217.

Hughes, T. (2000). *The finite element method: linear static and dynamic finite element analysis*. Dover Civil and Mechanical Engineering Series. Dover Publications.

Ismail, M., Comerford, A., and Wall, W. (2012). Coupled and reduced dimensional modelling of respiratory mechanics during spotaneous breathing. Preprint.

Jamal, R. A., Roughley, P., and Ludwig, M. (2001). Effect of glycosaminoglycan degradation on lung tissue viscoelasticity. *American Journal of Physiology- Lung Cellular and Molecular Physiology*, 280(2):306–315.

Karakaplan, A. D., Bieniek, M. P., and Skalak, R. (1980). A mathematical model of lung parenchyma. *Journal of Biomechanical Engineering*, 102(2):124–136.

Karlinsky, J. B., Bowers, J. T., Fredette, J. V., and Evans, J. (1985). Thermoelastic properties of uniaxially deformed lung strips. *Journal of Applied Physiology*, 58(2):459–467.

Karlinsky, J. B., Snider, G. L., Franzblau, C., Stone, P. J., and Hoppin, F. G. (1976). In vitro effects of elastase and collagenase on mechanical properties of hamster lungs. *The American Review of Respiratory Disease*, 113(6):769–777.

Kastelic, J., Galeski, A., and Baer, E. (1978). The multicomposite structure of tendon. *Connective Tissue Research*, 6(1):11–23.

Kauer, M., Vuskovic, V., Dual, J., Szekely, G., and Bajka, M. (2002). Inverse finite element characterization of soft tissues. *Medical Image Analysis*, 6(3):275–287.

Kikuchi, Y., Stamenovic, D., and Loring, S. H. (1991). Dynamic behavior of excised dog rib cage: dependence on muscle. *Journal of Applied Physiology*, 70(3):1059–1067.

Kononov, S., Brewer, K., Sakai, H., Cavalcante, F. S., Sabayanagam, C. R., Ingenito, E. P., and Suki, B. (2001). Roles of mechanical forces and collagen failure in the development of elastase-induced emphysema. *American Journal of Respiratory and Critical Care Medicine*, 164(10):1920–1926.

Kowe, R., Schroter, R. C., Matthews, F. L., and Hitchings, D. (1986). Analysis of elastic and surface tension effects in the lung alveolus using finite element methods. *Journal of Biomechanics*, 19(7):541–549.

Lanir, Y. (1983). Constitutive equations for the lung tissue. *Journal of Biomechanical Engineering*, 105(4):374–380.

Lee, G. and Frankus, A. (1975). Elasticity properties of lung parenchyma derived from experimental distortion data. *Biophysical Journal*, 15:481–493.

Levenberg, K. (1944). A method for the solution of certain nonlinear problems in least squares. *Quarterly of Applied Mathematics*, 11:164–168.

Mahnken, R. and Stein, E. (1996). Parameter identification for viscoplastic models based on analytical derivatives of a least-squares functional and stability investigations. *International Journal of Plasticity*, 12(4):451–480.

Maksym, G., Bates, J., and Navajas, D. (1993). Lung parenchyma stress response to step strain. *Proceedings 15th Annual IEEE International ASIC/SOC Conference*, 93:1116–1117.

Maksym, G. N. and Bates, J. H. (1997). A distributed nonlinear model of lung tissue elasticity. *Journal of Applied Physiology*, 82(1):32–41.

Marquardt, D. (1963). An algorithm for least-squares estimation of nonlinear parameters. *Journal of the Society for Industrial and Applied Mathematics*, 11:431–441.

Martin, C., Uhlig, S., and Ullrich, V. (1996). Videomicroscopy of methacholine-induced contraction of individual airways in precision-cut lung slices. *European Respiratory Journal*, 9(12):2479–2487.

Mercer, R. and Crapo, J. (1990). Spatial distribution of collagen and elastin fibers in the lungs. *Journal of Applied Physiology*, 69(2):756–765.

Mijailovich, S., Stamenovic., D., and Fredberg, J. (1993). Toward a kinetic theory of connective tissue micromechanics. *Journal of Applied Physiology*, 74(2):665–681.

Mijailovich, S. M., D. Stamenovic, D., Brown, R., Leith, D. E., and Fredberg, J. J. (1994). Dynamic moduli of rabbit lung tissue and pigeon ligamentum propatagiale undergoing uniaxial cyclic loading. *Journal of Applied Physiology*, 76(2):773–782.

Mishima, M., Hirai, T., Itoh, H., Nakano, Y., Sakai, H., Muro, S., Nishimura, K., Oku, Y., Chin, K., and Ohi, M. (1999). Complexity of terminal airspace geometry assessed by lung computed tomography in normal subjects and patients with chronic obstructive pulmonary disease. *Proceedings of the National Academy of Sciences*, 96(16):8829–8834.

Moulton, M., Creswell, L., Actis, R., Myers, K., Vannier, M., Szabo, B., and Pasque, M. (1995). An inverse approach to determining myocardial material properties. *Journal of Biomechanics*, 28(8):935–948.

Navajas, D., Maksym, G. N., and Bates, J. H. (1995). Dynamic viscoelastic nonlinearity of lung parenchymal tissue. *Journal of Applied Physiology*, 79(1):348–356.

Navajas, D., Mijailovich, S., Glass, G. M., Stamenovic, D., and Fredberg, J. J. (1992). Dynamic response of the isolated passive rat diaphragm strip. *Journal of Applied Physiology*, 73(6):2681–2692.

Ning, Q. and Wang, X. (2007). Response of alveolar type ii epithelial cells to mechanical stretch and lipopolysaccharide. *Respiration*, 74(5):579–585.

Ochs, M., Nyengaard, J., Jung, A., Knudsen, L., Voigt, M., Wahlers, T., Richter, J., and Gundersen, H. (2004). The number of alveoli in the human lung. *American Journal of Respiratory and Critical Care Medicine*, 169(1):120–124.

Ogden, R. (1974). On the overall moduli of non-linear elastic composite materials. *Journal of the Mechanics and Physics of Solids*, 22:541–553.

Ogden, R. (1997). *Non-linear elastic deformations*. Dover Pubns.

Ottani, V., Raspanti, M., and Ruggeri, A. (2001). Collagen structure and functional implications. *Micron*, 32(3):251–260.

Perlman, C. E. and Bhattacharya, J. (2007). Alveolar expansion imaged by optical sectioning microscopy. *Journal of Applied Physiology*, 103(3):1037–1044.

Prange, H. D. (2003). Laplace's law and the alveolus: a misconception of anatomy and a misapplication of physics. *Advances in Physiology Education*, 27(1-4):34–40.

Rausch, S. M. K., Haberthür, D., Stampanoni, M., Schittny, J. C., and Wall, W. A. (2011a). Local strain distribution in real three-dimensional alveolar geometries. *Annals of Biomedical Engineering*, 39(11):2835–2843.

Rausch, S. M. K., Martin, C., Bornemann, P. B., Uhlig, S., and Wall, W. A. (2011b). Material model of lung parenchyma based on living precision-cut lung slice testing. *Journal of the Mechanical Behavior of Biomedical Materials*, 4:583 – 592.

Rosen, M. (2004). *Surfactants and internfacial phenomena*. Wiley, 3 edition.

Sata, M., Takahashi, K., Sato, S., and Tomoike, H. (1995). Structural and functional characteristics of peripheral pulmonary parenchyma in golden hamsters. *Journal of Applied Physiology*, 78(1):239–246.

Schittny, J. (2008). High resolution 3d visualization of lung parenchyma. do new images force us to rewrite lung development? In *CMGM (internal seminar)*.

Schröder, J. (2004). Fluch der dimensionen? *Essen Unikate*, 23:37–49.

Schröder, J. and Neff, P. (2003). Invariant formulation of hyperelastic transverse isotropy based on polyconvex free energy functions. *International Journal of Solids and Structures*, 40(2):401–445.

Seshaiyer, P. and Humphrey, J. (2003). A sub-domain inverse finite element characterization of hyperelastic membranes including soft tissues. *Journal of Biomechanical Engineering*, 125(3):363–371.

Sobin, S., Fung, Y., and Tremer, H. (1988). Collagen and elastin fibers in human pulmonary alveolar walls. *Journal of Applied Physiology*, 64(4):1659–1675.

Stalling, D., Westerhoff, M., and Hege, H. (2005). Amira: A highly interactive system for visual data analysis. *The visualization handbook*, 38:749–767.

Stamenovic, D. and Yager, D. (1988). Elastic properties of air- and liquid-filled lung parenchyma. *Journal of Applied Physiology*, 65(6):2565–2570.

Stampanoni, M., Groso, A., Isenegger, A., Mikuljan, G., Chen, Q., Bertrand, A., Henein, S., Betemps, R., Frommherz, U., Böhler, P., Meister, D., Lange, M., and Abela, R. (2006). Trends in synchrotron-based tomographic imaging: the sls experience. In *Society of Photo-Optical Instrumentation Engineers (SPIE) Conference Series*.

Sugihara, T., Martin, C., and Hildebrandt, J. (1971). Length-tension properties of alveolar wall in man. *Journal of Applied Physiology*, 30(6):874–8.

Sugihara, T. and Martin, C. J. (1975). Simulation of lung tissue properties in age and irreversible obstructive syndromes using an aldehyde. *Journal of Clinical Investigation*, 56(1):23–29.

Suki, B., Barabasi, A., and Lutchen, K. (1994). Lung tissue viscoelasticity: a mathematical framework and its molecular basis. *Journal of Applied Physiology*, 76(6):2749–2759.

Suki, B. and Bates, J. H. T. (2008). Extracellular matrix mechanics in lung parenchymal diseases. *Respiratory Physiology and Neurobiology*, 163(1-3):33–43.

Suki, B., Ito, S., Stamenovic, D., Lutchen, K. R., and Ingenito, E. P. (2005). Biomechanics of the lung parenchyma: critical roles of collagen and mechanical forces. *Journal of Applied Physiology*, 98(5):1892–1899.

Suki, B., Peslin, R., Duvivier, C., and Farre, R. (1989). Lung impedance in healthy humans measured by forced oscillations from 0.01 to 0.1 Hz. *Journal of Applied Physiology*, 67(4):1623–1629.

Sussman, T. and Bathe, K.-J. (1987). A finite element formulation for nonlinear incompressible elastic and inelastic analysis. *Computers & Structures*, 26(1-2):357 – 409.

Tai, R. C. and Lee, G. C. (1981). Isotropy and homogeneity of lung tissue deformation. *Journal of Biomechanics*, 14(4):243–252.

The Acute Respiratory Distress Syndrome Network (2000). Ventilation with lower tidal volumes as compared with traditional tidal volumes for acute lung injury and the acute respiratory distress syndrome. *New England Journal of Medicine*, 342(18):1301–1308.

Toshima, M., Ohtani, Y., and Ohtani, O. (2004). Three-dimensional architecture of elastin and collagen fiber networks in the human and rat lung. *Archives of Histology & Cytology*, 67(1):31–40.

Tschanz, S. A., Makanya, A. N., Haenni, B., and Burri, P. H. (2003). Effects of neonatal high-dose short-term glucocorticoid treatment on the lung: a morphologic and morphometric study in the rat. *Pediatric Research*, 53(1):72–80.

Tsushima, K., King, L. S., Aggarwal, N. R., Gorordo, A. D., D'Alessio, F. R., and Kubo, K. (2009). Acute lung injury review. *Internal Medicine*, 48(9):621–630.

Vawter, D. L., Fung, Y. C., and West, J. B. (1978). Elasticity of excised dog lung parenchyma. *Journal of Applied Physiology*, 45(2):261–269.

Vlahakis, N. E., Schröder, M. A., Limper, A. H., and Hubmayr, R. D. (1999). Stretch induces cytokine release by alveolar epithelial cells in vitro. *American Journal of Physiology*, 277(1):167–173.

Wall, W. A., Bornemann, P. B., and Cyron, C. (2010a). *Nichtlineare Kontinuumsmechanik*. Institute for Computational Mechanics, Technische Universität München.

Wall, W. A. and Gee, M. W. (2010). BACI: A parallel multiphysics simulation environment. Technical report, Institute for Computational Mechanics, Technische Universität München.

Wall, W. A. and Rabczuk, T. (2008). Fluid structure interaction in lower airways of ct-based lung geometries. *International Journal for Numerical Methods in Fluids*, 57:653–675.

Wall, W. A., Wiechert, L., Comerford, A., and Rausch, S. (2010b). Towards a comprehensive computational model for the respiratory system. *International Journal for Numerical Methods in Biomedical Engineering*, 26(7):807–827.

Wall, W. A., Yoshihara, L., Bornemann, P. B., and Tinkl, S. (2012). *Nichtlineare Finite-Element-Methoden*. Institute for Computational Mechanics, Technische Universität München.

Ware, L. B. and Matthay, M. A. (2000). The acute respiratory distress syndrome. *New England Journal of Medicine*, 233(2):309–319.

Weibel, E. R. (1963). *Morphometry of the human lung*. Springer-Verlag.

Weibel, E. R. (1984). *The pathway for oxygen*. Harvard University Press Cambridge, MA.

Weibel, E. R. (1986). *Functional morphology of lung parenchyma*. Wiley Online Library.

West, J. B. (2008). *Respiratory Physiology The Essentials*. Wolters Kluwer-Lippincott Williams & Wilkins, 8 edition.

West, J. B. and Matthews, F. L. (1972). Stresses, strains, and surface pressures in the lung caused by its weight. *Journal of Applied Physiology*, 32(3):332–345.

Wiechert, L., Metzke, R., and Wall, W. A. (2009). Modeling the mechanical behavior of lung tissue at the microlevel. *Journal of Engineering Mechanics*, 135(5):434–438.

Wiechert, L. and Wall, W. A. (2010). A nested dynamic multi-scale approach for 3d problems accounting for micro-scale multi-physics. *Computer Methods in Applied Mechanics and Engineering*, 199(21-22):1342–1351.

Wilson, T. A. and Bachofen, H. (1982). A model for mechanical structure of the alveolar duct. *Journal of Applied Physiology*, 52(4):1064–1070.

Yager, D., Feldman, H., and Fung, Y. C. (1992). Microscopic vs. macroscopic deformation of the pulmonary alveolar duct. *Journal of Applied Physiology*, 72(4):1348–1354.

Yeoh, O. (1993). Some forms of the strain energy function for rubber. *Rubber Chemistry and Technology*, 66(5):754–771.

Yoshihara, L. and Wall, W. A. (2012). Fluid-structure interaction including volume coupling of homogenized subdomains for treating artificial boundaries. Preprint.

Yuan, H., Ingenito, E., and Suki, B. (1997). Dynamic properties of lung parenchyma: mechanical contributions of fiber network and interstitial cells. *Journal of Applied Physiology*, 83(5):1420–1431.

Yuan, H., Kononov, S., Cavalcante, F., Lutchen, K., Ingenito, E., and Suki, B. (2000). Effects of collagenase and elastase on the mechanical properties of lung tissue strips. *Journal of Applied Physiology*, 89(1):3–14.

Zeng, Y., Yager, D., and Fung, Y. (1987). Measurement of the mechanical properties of the human lung tissue. *Journal of Biomechanical Engineering*, 109(2):169–174.